Amine functionalized ordered mesoporous silica materials and its applications towards adsorbent and membrane for CO_2 capture

A Thesis
Submitted in Partial
Fulfillment of the Requirements for the Degree of

DOCTOR OF PHILOSOPHY

by

Sanjib Barma

Department of Chemical Engineering
Indian Institute of Technology Guwahati
Guwahati 781039, Assam, India

June 2015


भारतीय प्रौद्योगिकी संस्थान गुवाहाटी
Indian Institute of Technology Guwahati

Dedicated

To

My Late Father

Department of Chemical Engineering
Indian Institute of Technology Guwahati
Guwahati 781039, Assam, India

CERTIFICATE

It is certified that the work contained in this thesis entitled **"Amine functionalized ordered mesoporous silica materials and its applications towards adsorbent and membrane for CO_2 capture"** submitted by **Mr. Sanjib Barma** for the award of the degree of Doctor of Philosophy has been carried out in Department of Chemical Engineering, Indian Institute of Technology Guwahati under my supervision and this work has not been submitted elsewhere for the award of any other degree or diploma.

This thesis in my opinion, has reached the standard fulfilling the requirements for the award of the degree of Doctor of Philosophy in accordance with the regulations of the institute.

(**Dr. Bishnupada Mandal**)
Professor, Head
Department of Chemical Engineering
Indian Institute of Technology Guwahati
Guwahati 781039, India

ACKNOWLEDGEMENTS

The completion of this thesis would not have been possible without the support and encouragement of several special people including my well-wishers, my friends, colleagues and various institutions. Hence, it is a pleasant task to express my thanks to all those who contributed in many ways to the success of this study and made it an unforgettable experience for me.

First of all, I am extremely grateful to my research guide, ***Professor Bishnupada Mandal,*** *for his valuable guidance, scholarly inputs and consistent encouragement I received throughout the doctoral work. He has been supportive and has given me the freedom to pursue my research work without objection. His patience, flexibility, genuine caring and concern, and faith in me during the doctoral process enabled me to attend to life while also earning my Ph.D. I consider it as a great opportunity to do my doctoral programme under his guidance and to learn from his research expertise. Thank you sir, for all your help, advice and support.*

I must also acknowledge my doctoral committee chairman ***Dr. G. Pugazhenthi,*** *Department of Chemical Engineering, for his useful suggestion during the course of my research. I would also like to profoundly acknowledge my other doctoral committee members* ***Prof. Gopal Das,*** *Department of Chemistry, and* ***Dr. Chandan Das,*** *Department of Chemical Engineering, and for their valuable suggestions during my progress review seminars. Their suggestions have really helped me to make necessary improvements towards various stages of my research work.*

I am thankful to ***Dr. Sasidhar Gumma,*** *for being very kind and allowing me to avail the research facilities in his magnetic suspension balance for gas adsorption measurement.*

I must also thank to the previous ***Head*** *of the Department of Chemical Engineering and also to the* ***faculty members*** *for their consistent encouragements and supports to me.*

The thesis would not have come to a successful completion, without the help I received from the staff of the Analytical Lab, Department of Chemical Engineering. I would like to thank ***Kaustavda, Lukuda, Harshaji, Ritumoniji, Debojit, Prasunda*** *for their services in connection with analysis of data. I must also thank* ***Bhagyoda, Jyotish*** *for their support in various forms.*

I would also like to convey my sincere thanks to the ***Central Instruments Facility (CIF)*** *of IIT Guwahati for providing the analytical facilities to carry out FESEM, TEM, analysis. My sincere thanks go to* ***Dr. Arun Ch. Borsaikia*** *and* ***Mr. Pranab Hazarika,*** *Department of Civil Engineering of IIT Guwahati for providing me the Universal Testing Machine to carry out my experimental work.*

I gratefully acknowledge the financial support of the Council of Scientific and Industrial Research (CSIR), Government of India, for providing financial support for my research work (Grant No. 22(0630)/13/EMR-II).

I would gratefully acknowledge ***Prashant, Rupak, Satya, Pruthvi*** *for their kind help for completion of my doctoral work.*

Coming to my other labmates, I must acknowledge ***Arijit*** *for his helping in GC handling during the initial period of my PhD work. I am fortunate enough to have juniors like* ***Bisweswar, Binay, Babul, Mridusmita, Rajashree*** *in my research group. I acknowledge their constant encouragement and help during the course of the research. It was always good to work with them.*

I am thankful to all my excellent batch mates and juniors including ***Sravanthi, Murali, Avik, Kishant, Sahu, Ashim, Manish,***

Suresh, Supriyo, Vinoth, Rajsekhar, China, Yadav, Ardhendu, Chitrita, Arijit, Sujoy, Sankar, Mahesh *for their cooperation and friendly behaviour which helped in several forms during my doctoral work. I enjoyed lot of encouraging discussions with them.*

I specially mention about my friends in IIT Guwahati, ***Mannada, Ruhit, Milan, Avijit, Amrita, Leela****. Their presence was always a huge relaxation for me in the hectic work load in the lab. I spent some precious moments with all of them. I thoroughly enjoyed the informal discussions with all of them during my tea breaks.*

On personal note, I owe a lot to my parents, who encouraged and helped me at every stage of my personal and academic life, and desired to see this achievement come true. At this moment, I deeply miss my father who passed away in the 2nd year of my PhD. I can't forget his hard times. Despite of his ill health, he never made me to realize his bad health condition over phone so that my research work gets disturbed. Sorry, 'Baba' I could not able to stay beside you during the last moment of your life when you wanted to see me desperately. I wish his soul roots in peace and solace in the heaven. It is to him that I dedicate this work. My mother is always a great supporter and strength of me. She took all the responsibility back home during those tough days of my life without any complaining. I cannot express in my words how valuable they are for me. Happy to have wonderful sisters ***Ruby*** *&* ***Tumpa*** *providing me immense support at all the ups and down's of my life. Great to have wonderful in-laws, brother and sister in-laws, nieces, nephews, who showered unconditional love and supported me with every possible way to see the completion of my doctoral work.*

Finally, and most importantly, I would like to thank my wife ***Moumita.*** *Her support, encouragement, quiet patience and untiring love have made it possible for me to come so far. Her tolerance of my occasional vulgar moods is evidence in itself of her unyielding devotion and love.*

In addition, these acknowledgements would not be complete if I would not mention my 3 and ½ year old son, ***Ruhan.*** *He has been a twinkle in my eyes since he was born. Throughout my doctoral program, he has been a bright light in my eyes.*

In closing I realize that it is impossible to mention each and every one who crossed my path in this exciting journey. My sincere apology goes to all of those to whom I forget to mention but helped me at any part of the research work.

Sanjib Barma

LIST OF PUBLICATIONS

Published Articles in International Refereed Journals

1. **Barma, S.,** and Mandal, B. **(2014).** Effects of sintering temperature and initial compaction load on alpha-alumina membrane support quality. ***Ceramics International,*** 40, 11299–11309. **(Elsevier)**.

2. **Barma, S.,** and Mandal, B. **(2015).** Synthesis and characterization of ordered mesoporous silica membrane: role of porous support and gas permeation study. **Microporous & Mesoporous Materials,** 210, 10-19. **(Elsevier)**.

Communicated/Under Review in Refereed International Journals

3. **Barma S.**, Mishra, P., Gumma, S., and Mandal, B. To study the amine-functionalized ordered mesoporous silica material (MCM 48) characteristics for CO_2 capture in flue gas condition.
4. **Barma, S.,** and Mandal, B. A comparison study for ordered mesoporous silica materials obtained by acidic & basic route for CO_2 adsorption.

Conference Presentations (National and International)

1. **Barma, S.,** and Mandal, B. (**2014**). Synthesis and Characterization of ordered mesoporous silica membrane by spin coating method on α-alumina support. (**CSChE 2014**) October 19-20, Niagara Falls, CANADA
2. **Barma, S.,** and Mandal, B. (**2014**). Gas permeation properties of MCM-48 membrane: synthesis & characterization. The Indian Chemical Engineering Congress (**CHEMCON 2014**), Dec 27-30, Chandigarh, INDIA.

3. **Barma, S.,** and Mandal, B. (**2013**). Synthesis and Characterisation of MCM-48 Coated Inorganic Membrane for CO_2 / N_2 Separation. International Conference on “Membranes and Applications” (**ICMA 2013**), Nov 22-23, CGCRI Kolkata, INDIA.
4. **Barma, S.,** and Mandal, B. (**2013**). Comparative study of the properties of MCM 48 synthesized by room temperature method with other synthesis methods and the overall feasibility of such adsorbents. The Indian Chemical Engineering Congress (**CHEMCON 2013**), Dec 27-30, Mumbai, INDIA.
5. Deogam, B., Das, B., **Barma, S.,** Mondal, A., and Mandal, B. (**2013**). Absorption of Carbon Dioxide into Piperazine Activated Aqueous Diethanolamine. Energy System Modeling and Optimization Conference (**ESMOC 2013**) Dec 9-11, NIT Durgapur, INDIA
6. **Barma, S.,** Mandal, A. and Mandal, B. (**2012**). Synthesis and Characterization of MCM-48 Materials at Different Aging Time. The Indian Chemical Engineering Congress (**CHEMCON 2012**), Dec 27-30, Jalandhar, INDIA.
7. **Mandal, A., Barma, S.,** and Mandal, B. (**2012**). Synthesis and Characterization of Thin-Film-Composite Polymeric Membrane Containing Amine Carrier. The Indian Chemical Engineering Congress (**CHEMCON 2012**), Dec 27-30, Jalandhar, INDIA.
8. **Barma, S.,** and Mandal, B. (**2012**). Gas Separation by Inorganic Composite Membrane. Twenty First International Symposium on Processing and Fabrication of Advanced Materials (**PFAM XXI 2012**), Dec 10-13, IIT Guwahati, INDIA.

ABSTRACT

The main aim of this work is to study the CO_2 separation using amine functionalized ordered mesoporous silica materials in adsorption based technology as well as membrane based technology. To know the inner detail of surface characteristics and the CO_2 adsorption capacities of the amine-functionalized ordered mesoporous silica materials (OMS), the powder form of the materials are synthesized and characterized. Functionalizations of the ordered mesoporous silica (MCM 48) materials with different amines are performed by using three different amines such as 3-aminopropyltriethoxysilane (3-APS), 3-aminopropyltrimethoxysilane (3-APTMS), and 3-(2-aminoethylamino) propyl trimethoxysilane (3-2-Am). The degree of grafting is observed to be similar for all three amines. Small differences between uptakes of different amine grafted samples are attributed to the difference in their surface areas. CO_2 adsorption at 0.2 bar and 30 ^{o}C is increased significantly from ~0.1 mmol g^{-1} to ~0.84 mmol g^{-1} after grafting of 9 mmol of different amine on 1 g of MCM-48 material. The CO_2 adsorption for each sample is performed between the pressure ranges of 0-10 bar. It is observed that at low pressures up to 4 bar, amine loaded sample exhibit more CO_2 uptake, at a higher pressures pure MCM-48 shows better CO_2 loading. The CO_2 adsorption capacities at a particular temperature (30 ^{o}C) for different dosing (9, 10, 15 & 20 mmol) of amine-functionalized OMS materials are also studied. CO_2 uptake obtained for amine grafted MCM-48 samples is comparable to the available literature. The effects of temperatures (30 ^{o}C, 60 ^{o}C, and 75 ^{o}C) for the 3-APS functionalized OMS material are

also examined to understand whether physisorption or chemisorption dominates for amine loaded samples. It is observed that adsorption uptake decreases with the increase of temperature. This indicates that the interactions between CO_2 molecules and adsorbent samples are exothermic in nature. Modeling of CO_2 isotherms is carried out to get molecular level insight and to calculate Henry's constants. CO_2 isotherm of pure MCM-48 material follows the Langmuir model indicating the homogeneous adsorption nature of MCM-48 structure. In contrast, CO_2 isotherm on amine grafted samples follow Dual Site Langmuir (DSL) model. It is seen that Henry's constant of pure MCM-48 material (0.47 mmol g^{-1} bar^{-1}) is significantly lower than that of samples containing 9 mmol of different amines (29 - 84 mmol g^{-1} bar^{-1}) indicating that CO_2 molecules are having specific interaction with amino functional groups, which is much stronger than weak van der Waals interactions in case of the pure MCM-48 sample.

After inheriting the concept of amine-functionalized ordered mesoporous silica materials for CO_2 adsorption, two different techniques for synthesizing OMS materials are studied and CO_2 uptake capacity for those materials are compared. Then the OMS materials are introduced in more energy saving application to form membrane by spin coating technique.

To prepare crack-free ordered mesoporous silica membranes by spin coating, the quality of the support is of crucial importance to the membrane layer integrity. So, α-alumina support at various sintering temperatures (1200 °C, 1300 °C, 1400 °C & 1500 °C) and various compaction load (50 kN, 150 kN, 250 kN & 350 kN), are prepared and investigation studies were performed to find out the best quality support for synthesizing spin-coated silica membranes for CO_2 separation application. The ordered mesoporous silica membranes are successfully synthesized on porous α-alumina support. Dependency on the support surface pore size for synthesizing good quality ordered mesoporous silica membranes are explored. It is observed that the lower surface pore size support exhibits more ordered silica membrane. Finally, the performance studies for amine-modified ordered mesoporous silica membranes were investigated by using single and binary gas mixture (CO_2/N_2). The amine functionalized silica membrane showed promising candidates for CO_2 separation from process streams as they exhibit CO_2 selective at higher pressure.

CONTENTS

		Page No.
Dedication		**iii**
Certificate		**v**
Acknowledgement		**vii**
Abstract		**xv**
List of Tables		**xxiii**
List of Figures		**xxiv**
CHAPTER 1	**CO_2 CAPTURE AND EMISSIONS OVERVIEW, LITERATURE REVIEW AND OBJECTIVES**	**1 - 41**
1.1	**Introduction and Overview of CO_2 Emissions**	1
1.2	**Indian Scenario for CO_2 Emission & CCS Technology**	2-4
1.3	**CO_2 Capture Strategies**	4
1.4	**Available Techniques for CO_2 Capture**	5
1.5	**Requirement of Alternative Technique**	6-8
	1.5.1 Adsorbent technology for CO_2 capture	6
	1.5.2 Membrane technology for CO_2 capture	7-8
	1.5.3 Difference between adsorbent and membrane technology	8
1.6	**Ordered Mesoporous Silica (OMS) Materials for CO_2 Adsorption**	9-11
	1.6.1 MCM materials	10-11
1.7	**Ordered Mesoporous Silica Membranes for CO_2 Separation**	11-13
1.8	**Literature Review**	13-22
	1.8.1 Literature review on adsorption based CO_2 capture	13-17
	1.8.2 Literature review on Membrane based CO_2 separation	18-22
1.9	**Importance and Objectives of the Present Study**	22-24
1.10	**Thesis Outline**	24-27
References		28-41
CHAPTER 2	**CO_2 CAPTURE BY AMINE MODIFIED ORDERED MESOPOROUS SILCA MATERIALS & MEMBRANES: THEORY, REACTIONS AND TRANSPORT MECHANISMS**	**42 - 71**
2.1	**Introduction to Adsorption**	43
2.2	**Phase Rule for Adsorption**	43-44
2.3	**Equilibrium Adsorption Isotherm**	44-45

2.4 **Henry’s Constant** 45-46
2.5 **Models for Pure Gas Isotherms** 46-7
    2.5.1 Langmuir isotherm 46-47
    2.5.2 Dual Site Langmuir (DSL) isotherm 47
    2.5.3 Virial isotherm 48
    2.5.4 Langmuir-virial isotherm 49
2.6 **Theoretical Background for Ordered Mesoporous Silica Synthesis** 49-55
    2.6.1 Synthesis mechanism of mesoporous silica by basic route 51-52
    2.6.2 Synthesis mechanism of mesoporous silica by acidic route 52
    2.6.3 Different techniques to synthesize ordered mesoporous silica membrane 53
    2.6.4 Mesoporous silica membrane formation by EISA mechanism 53-55
2.7 **Spin Coating Method** 55-56
    2.7.1 Steps involved in Spin Coating methods 56
2.8 **Gas permeation through Amine Modified Silica Pore** 57-60
2.9 **Fundamentals of Molecular Transport in Membranes** 61
2.10 **Mass transport mechanisms** 62-66
    2.10.1 Free molecule regime 63-64
    2.10.2 Viscous flow 64-65
    2.10.3 Gaseous diffusion 65
    2.10.4 Surface diffusion 65
    2.10.5 Molecular sieving 65-66
References 67-71

CHAPTER 3 **CO_2 ADSORPTION CHARACTERISTICS FOR PURE & AMINE MODIFIED ORDERED MESOPOROUS SILICA POWDERS** **72-96**

3.1 **Introduction** 73-74
3.2 **Materials** 74
3.3 **Experimental** 75-77
    3.3.1 Synthesis 75-76
        3.3.1.1 Synthesis of MCM 48 by basic route 75
        3.3.1.2 Synthesis of amine-Grafted MCM 48 75-76
    3.3.2 Characterization techniques 76-77
    3.3.3 CO_2 Adsorption Measurements 77
3.4 **Results & Discussions** 77-91
    3.4.1 Thermo-gravimetric analysis 77-78

3.4.2 Surface area analysis 78-79
3.4.3 Fourier-transform infrared spectroscopy (FTIR) analysis 80-81
3.4.4 X-ray diffraction (XRD) analysis 81-82
3.4.5 CO_2 adsorption analysis 83-91
3.5 Conclusions 91-92
References 93-96

CHAPTER 4 SYNTHESIS & CHARACTERIZATION OF PURE ORDERED MESOPOROUS SILICA (OMS) POWDER OBTAINED BY ACIDIC AND BASIC ROUTES FOR CO_2 ADSORPTION **97-113**

4.1 Introduction 98
4.2 Materials 99
4.3 Experimental 99
4.3.1 Synthesis 99
4.3.1.1 Synthesis of OMS by basic route 99
4.3.1.2 Synthesis of OMS by acidic route 99-100
4.3.2 Characterization techniques 100
4.3.3 CO_2 adsorption measurements 100
4.4 Results & Discussions 101-110
4.4.1 Surface area analysis 101-103
4.4.2 FTIR analysis 103-104
4.4.3 Thermo-gravimetric analysis 104-105
4.4.4 X-ray diffraction analysis 105-106
4.4.5 Transmission electron microscopy (TEM) analysis 106-108
4.4.6 CO_2 adsorption analysis 109-110
4.5 Conclusions 110
References 111-113

CHAPTER 5 SYNTHESIS AND OPTIMIZATION OF HIGH SURFACE QUALITY α-ALUMINA COMPACT MEMBRANE SUPPORT **114-142**

5.1 Introduction 115-117
5.2 Materials 117
5.3 Experimental 117-123

5.3.1 Membrane support synthesis 117-119
5.3.2 Characterization techniques 120-123
5.4 Results & Discussions 124-139
5.4.1 Raw α-alumina powder properties 124-125
5.4.2 Support properties 125-139
5.4.2.1 *XRD analysis* 125-128
5.4.2.2 *Flexural strength analysis* 128-129
5.4.2.3 *FESEM analysis* 129-133
5.4.2.4 *Nitrogen gas permeation analysis* 133-135
5.4.2.5 *Porosity, density and shrinkage analysis* 135-139
5.5 Conclusions 139
References 140-142

CHAPTER 6 ORDERED MESOPOROUS SILICA MEMBRANE SYNTHESIS AND CHARACTERIZATION ON DIFFERENT SUPPORT **143-174**

6.1 Introduction 144-145
6.2 Materials 145
6.3 Experimental 145-153
6.3.1 Support synthesis 145
6.3.2 Membrane synthesis 145-147
6.3.3 Functionalization of silica membrane by chemical grafting 147-149
6.3.4 Membrane Characterization 149-153
6.4 Results & Discussions 153-170
6.4.1 X-ray Diffraction Analysis 153-157
6.4.2 Fourier Transform Infrared Spectroscopy Analysis 157-160
6.4.3 FESEM & EDX analysis 160-163
6.4.4 Single gas permeation analysis 164-168
6.4.5 Mixed gas permeation analysis 168-170
6.5 Conclusions 170
References 171-174

CHAPTER 7 CONCLUSIONS AND RECOMMENDATION FOR FUTURE WORK **175-180**
7.1 Conclusions 176-178
7.2 Recommendations on future directions 178-179

7.3 **References** 180

APPENDIX 1 **DETAIL OF THE EXPERIMENTAL PROTOCOL FOLLOWED FOR ADSORPTION MEASUREMENT** **181-182**

A1.1 **Experimental Protocol** 181-182

APPENDIX 2 **GAS TRANSPORT PARAMETERS CALCULATION AND GAS CHROMATOGRAPHY DATA** **183-191**

A2.1 **Gas Transport Parameters (CO_2 and N_2 fluxes, CO_2 and N_2 permeability, CO_2/N_2 selectivity) Calculation** 183-191

A2.2 **Gas Chromatography Data of Calibration Gases and G.C Operating Protocol** 192-196

A2.2.1 *Calibration Gases for G.C* 192-193

A2.2.2 *G.C operating protocol* 194-195

A2.2.3 *Detail Purity of all Calibration gases* 196

LIST OF TABLES

TABLE NO	TABLE CAPTION	PAGE NO
Table 3.1	BET surface area and pore volume of the different MCM-48 samples.	**79**
Table 3.2	CO_2 Adsorption Capacity of 3-APS Grafted Silica Adsorbents[a]	**85**
Table 3.3	Model parameters for adsorption isotherms on different MCM-48 materials*.	**88**
Table 4.1	BET surface area and pore volume of different OMS samples.	**102**
Table 5.1	Average particle size and pore diameter of the sintered α-alumina membrane supports at different preparing conditions measured by ImageJ software from FESEM image and by N_2 gas permeation technique	**135**
Table 6.1	‘d’spacing value for the different membranes before and after the calcination	**155**
Table 6.2	CO_2 separation properties of different membrane samples at 298K and ~138 kPa pressure.	**168**
Table A2.1	Detail purity percentage of all calibration gases	**196**

LIST OF FIGURES

FIGURE NO	**FIGURE CAPTION**	**PAGE NO**
Figure 1.1	Schematic of the 3-APS modified OMS pore structure (not to scale)	**10**
Figure 1.2	Structures of mesoporous M41S materials (a) MCM 48 (b) MCM 41 & (c) MCM 50	**11**
Figure 2.1	IUPAC classifications of adsorption isotherms	**45**
Figure 2.2	Different types of surfactant silica interactions	**50**
Figure 2.3	Silica precursor at variable pH condition	**51**
Figure 2.4	Evaporation induced self-assembly mechanism for film formation	**55**
Figure 2.5	The steps involved in the spin-coating process	**56**
Figure 2.6	Structural formulaes of some important aminosilanes	**57**
Figure 2.7	Mechanism of carbamate formation	**58**
Figure 2.8	Mechanisms of CO_2 adsorption to the pairs of (a) primary-primary, (b) primary-secondary, and (c) secondary-secondary amines	**59**
Figure 2.9	Surface reaction of tethered amine groups with CO_2	**60**
Figure 2.10	Mechanisms of mass transport through porous media: a) Viscous flow(Poiseuille); b) Knudsen diffusion; c) surface diffusion; d) molecular sieving	**62**
Figure 3.1	Thermogram of different MCM-48 based samples under the flow of N_2	**78**
Figure 3.2	Adsorption isotherm of N_2 on MCM-48 based samples at 77 K	**79**
Figure 3.3	FTIR spectra on different MCM-48 based materials	**80**
Figure 3.4	XRD pattern of pure MCM-48 sample	**81**
Figure 3.5	XRD pattern of pure and amine modified MCM-48 samples	**82**
Figure 3.6	CO_2 isotherms of different MCM-48 samples at 30 ^oC. Symbols are experimental data and lines are fits obtained using Langmuir (for pure MCM-48 sample) and DSL (for amine grafted MCM-48 samples)	**84**

isotherm parameters from Table 3.3

Figure 3.7 CO_2 isotherms of OMS (MCM-48) samples with different 3-APS loading content at 30 °C. **86**
Figure 3.8 CO_2 isotherms of 20 mmol 3-APS loaded MCM-48 sample at different temperatures **86**
Figure 3.9 CO_2 Henry's constant of pure MCM-48 and amine loaded MCM-48 samples at 30 °C **90**
Figure 3.10 Henry's constant of 3-APS loaded OMS (MCM-48) samples at 30 °C **91**
Figure 4.1 TGA curves of crosslinked-PVA-PVP membrane containing single (PEI) and blended (PEI and TEPA) amines. 60 mole% degree of crosslinking of PVA with HCHO **101**
Figure 4.2 BJH pore size distribution profile for samples OMS_AC & OMS_H samples **102**
Figure 4.3 FTIR spectra for OMS materials synthesized by various routes **104**
Figure 4.4 Thermo-gravimetric analysis for the OMS samples synthesized by various routes **105**
Figure 4.5 X-ray diffraction peaks for the OMS materials **106**
Figure 4.6(a) TEM image of OMS synthesized under basic route (OMS_H) **107**
Figure 4.6(b) TEM image of OMS synthesized under acidic route (OMS_AC) **108**
Figure 4.7 The SAED patterns of OMS synthesized under acidic route (OMS_AC) **108**
Figure 4.8 CO_2 adsorption isotherm of samples OMS_AC & OMS_H at 30 °C **109**
Figure 5.1 Stainless steel mold for support preparation **118**
Figure 5.2 Programmable furnace with P310 controller **119**
Figure 5.3 α-alumina membrane support after sintering and polishing **119**
Figure 5.4 Schematic representation of single gas permeation set-up (picture in the right side) **121**
Figure 5.5 Particle size distribution of pure α- alumina powder **124**
Figure 5.6 XRD patterns of raw α-Alumina powder **125**
Figure 5.7 XRD patterns of the sintered α-Alumina membrane support at **(a)** 50kN, **(b)** 150 kN, **(c)** 250 kN and **(d)** **126**

350 kN load at different temperatures

Figure 5.8 XRD patterns of the sintered α-Alumina membrane support at **(a)** 1200°C, **(b)** 1300°C, **(c)** 1400°C and **(d)** 1500°C at different load **127**

Figure 5.9 Flexural strength vs. compaction load for the supports synthesized at different sintering temperature **129**

Figure 5.10 FESEM image of the α-Alumina disc membrane support synthesized at 1200°C sintering temperature at **(a)** 50 kN, **(b)** 150 kN, **(c)** 250 kN and **(d)** 350 kN initial load. **130**

Figure 5.11 FESEM image of the α-Alumina disc membrane support synthesized at 1300°C sintering temperature at **(a)** 50 kN, **(b)** 150 kN, **(c)** 250 kN and **(d)** 350 kN initial load. **131**

Figure 5.12 FESEM image of the α-Alumina disc membrane support synthesized at 1400°Csinteringtemperature at **(a)** 50 kN, **(b)** 150 kN, **(c)** 250 kN and **(d)** 350 kN initial load **132**

Figure 5.13 FESEM image of the α-Alumina disc membrane support synthesized at 1500°C sintering temperature and **(a)** 50 kN, **(b)** 150 kN, **(c)** 250 kN and **(d)** 350 kN initial load **133**

Figure 5.14 Effect of pressure on N_2 gas permeability for membrane supports synthesized at different sintering temperature **(a)** 1200° C, **(b)** 1300° C, **(c)** 1400° C and **(d)** 1500° C at different initial load **134**

Figure 5.15 Final density of the sintered membrane support as a function of applied load at different temperatures: 1200°C, 1300°C, 1400°C and 1500°C **136**

Figure 5.16 Porosity of the sintered membrane support as a function of applied load at different temperatures: 1200°C, 1300°C, 1400°C and 1500°C **137**

Figure 5.17 Porosity of the sintered membrane support as a function of temperature at different applied load: 50 kN, 150 kN, 250 kN and 350 kN **138**

Figure 5.18 Percentage Shrinkage in diameter of the sintered membrane support as a function of applied load at different temperatures: 1200°C, 1300°C, 1400°C and 1500°C **139**

Figure 6.1	Synthesis procedure for OMS membrane by spin coating method	**146**
Figure 6.2	Spin coater Instrument for membrane coating	**147**
Figure 6.3	Experimental set-up for amine functionalization for OMS membrane	**148**
Figure 6.4	Schematic representation of gas-permeation set-up	**150**
Figure 6.5	Gas permeation Experimental set-up	**152**
Figure 6.6	XRD diffraction patterns of the silica membranes synthesized on different supports before calcination and after calcination	**154**
Figure 6.7	XRD diffraction patterns of the amine functionalized silica membrane (MR2) and unmodified membrane (MR2)	**156**
Figure 6.8	FTIR spectra of different silica membranes synthesized on different α-alumina supports.	**158**
Figure 6.9	FTIR spectra in the range 1300-850 cm^{-1} of different silica membranes synthesized on different α- alumina supports	**159**
Figure 6.10	FESEM images of the surfaces of the different silica membranes (MR1, MR2, and MR3) synthesized on different α-alumina supports and the corresponding α-alumina supports (MR1(S), MR2(S) and MR3(S))	**161**
Figure 6.11	FESEM images for the cross-sectional view of the different silica membranes (MR1, MR2, and MR3) synthesized on different α-alumina supports	**162**
Figure 6.12	EDX analysis of the different silica membranes (MR2 and MR3) synthesized on different α-alumina supports at different locations shown in the Figure 6.11	**163**
Figure 6.13	N_2 permeance for the different silica membranes (MR1, MR2, and MR3) and corresponding supports (MR1(S), MR2(S), and MR3(S)) at different feed pressures	**164**
Figure 6.14	N_2 permeance for the different silica membranes (MR1, MR2, and MR3) at different feed pressures	**165**
Figure 6.15	Plots of permeance versus $M_W^{-1/2}$ of various gases through mesoporous silica membrane (MR3), measured at 298 K and ~138 kPa	**166**

Figure 6.16 N_2 and CO_2 permeance for the different silica membranes (MR1, MR2, and MR3) at different feed pressures **167**

Figure 6.17 CO_2 and N_2 permeance versus feed absolute pressure for CO_2 separation membrane (MR2) at 363 K **169**

Figure A2.1 Peak intensity and position of all five CO_2 and N_2 calibration gases **192**

Figure A2.2 Plot of all five CO_2 and N_2 calibration gases **193**

Chapter 1

CO_2 CAPTURE AND EMISSIONS OVERVIEW, LITERATURE REVIEW AND OBJECTIVES

This chapter presents a discussion on emission of CO_2 and its impact on global warming issues in the World and India's viewpoint. It also discusses the features of different technologies for CO_2 separation. The use of ordered mesoporous silica materials for CO_2 capture and difference between adsorption and membrane technology are also included in this chapter. It elaborates the background of the research work. Importance and objectives of the present work are highlighted accordingly. The chapter subsequently presents detailed literature review that includes CO_2 separation by amine modified mesoporous silica materials and membranes.

1.1. Introduction and Overview of CO_2 Emissions

There is growing scientific agreement that CO_2 concentration level is rising in the atmosphere due to the human activities (e.g., fossil fuel burning, cement and lime production, ammonia and ethylene oxide synthesis, aluminium and glass industries, fermentation, deforestation, use of fertilizers) and this is responsible for the warming effect on the climate. Among different gaseous irradiative forces (CO_2, CH_4, N_2O), CO_2 is the major gas responsible for the greenhouse effect which is ca. 70% [**1-2**]. Since preindustrial era, the CO_2 concentration in the troposphere has increased from 280 ppmv in 1750 to ~400 ppmv at recent study, with an annual increase of about 1 ppm [**1**]. The earth's surface temperature has risen about 0.6 − 0.7°C during the past century due to the increase of CO_2 concentration. The increase rate is observed prominent during the past 20 years from an annual growth rate of 1.1% in the period 1990−1999 to >3% during the period 2000−2004 [**3**]. In 2010, the CO_2 emissions from fuel combustion were observed to be 30 Gtonnes worldwide, 41% of that being related to energy production [**4**]. On current trends, the Intergovernmental Panel on Climate Change (IPCC) projected an average increase of the global temperature by (1.8−4.0)°C during this century, causing irreversible consequences for mankind and ecosystems (e.g., increase of ocean levels) [**5**]. Since the beginning of the 1990s, climate change has moved up top of the agenda in the international politics. The Kyoto Protocol, approved by more than 140 nations in 1997 under the supports of the UN Framework Convention on Climate Change (UNFCCC) and extended during climate summit held in Doha (Qatar) in October 2012, constitutes an international milestone to counteract global warming [**6-7**].

1.2. Indian Scenario for CO_2 Emission & CCS Technology

According to The International Energy Agency (IEA), India will be among the top three emitters of the world by 2030 in terms of total CO_2 emitted each year (it is currently ranked sixth). World Coal Association predicted that coal use is to rise by over 60% over this same period, with developing countries responsible for 97% of this increase. This rise is primarily due to fulfil the increased rates of electrification. The IEA has studied a number of global GHG reduction scenarios and concluded that CCS (Carbon Capture & Storage) is "the most important single new technology for CO_2 savings" in both power generation and industry.

Three strategies have been raised for long-term large-scale CO_2 storage: (1) geological storage in depleted oil and gas fields, deep saline aquifers, or unminable coal seams (formation of CO_2 pools or solid gas hydrates), (2) deep ocean storage in “CO_2 lakes” and marine sediments, and (3) industrial fixation in inorganic carbonates. CO_2 transport to the storage site could be carried out either at high pressure by gas duct or by liquefying CO_2 at moderate pressure (up to 7 bar) and − 20°C (off shore transport by ship). Among the three steps of the CCS chain, CO_2 capture is by far the most expensive one, responsible for 50 − 90% of the overall chain cost depending on the CO_2 emission source [**8**].

CCS has a large potential in industry and petroleum refineries not only because of its large CO_2 emissions but also because there are many industrial processes that generate gas streams rich in CO_2, or in some cases pure CO_2, which could reduce the costs of CCS. A recent study by the IEA estimates that in a scenario to reduce global greenhouse gas (GHG) emissions to half in 2050 compared to today’s level, about half of all CCS installed (up to more than 10 Gt per year) would be in industrial processes (cement, iron and steel and chemicals) and fuel transformation sector (petroleum refineries and liquefied natural gas production) [**8**].

1.3. CO_2 Capture Strategies

In general, CO_2 capture in a fossil fuel combustion process can be achieved following four different strategies [**9**], which aim at maximizing the concentration of CO_2 in the gas stream: (i) post-combustion capture; (ii) pre-combustion capture; (iii) oxyfuel combustion; and (iv) electrochemical separation.

There are several studies reported in detail of these strategies. Every strategy has their potential depending on the application [**10-11**]. Post combustion capture is the simplest to be implemented since the separation process can be easily adapted to the existing plant (after the combustion step) but CO_2 capture is by far the most challenging option, since a diluted, low-pressure, wet, and hot CO_2/N_2 mixture has to be treated. This makes the separation more difficult and increases the energy penalty. In oxy-fuel combustion the action can be taken before the combustion or performing oxy-combustion of the fuels to get pure CO_2. The separation strategy is different in oxy-combustion because in the oxy-combustion, the fuel is burned with nearly pure oxygen (typically greater than 95% purity) mixed with recycled flue gas and the final gas consisting mainly of CO_2 and water is generated, ready for sequestration after water condensation without the necessity of CO_2 stripping from the gas stream [**12**]. Whereas, in the pre-combustion, the CO_2 is separated from a gas stream that contains mainly H_2 (the fuel gas is converted to H_2, CO and CO_2 by injecting steam and oxygen) since carbon is removed from the fuel before combustion [**10, 12-13**]. For electrochemical separation, a high temperature fuel cell is used to convert the chemical energy in fuels directly to electricity [**9**]. Finally, the product stream contains a mixture of CO_2 and water, hence, only water condensation is required to produce pure CO_2.

1.4. Available Techniques for CO_2 Capture

Three main technologies emerge for pre- and post-combustion CO_2 capture [**14-16**]. These are (a) chemical and physical absorption (wet scrubbing) using alkanolamines, solutions of alkali-metal carbonates, ethylene glycol, "chilled" ammonia etc. (b) thermal and pressure swing adsorption (TSA and PSA respectively) using either physical adsorbents (e.g., alumina, activated carbon, silica gel, molecular sieves etc.) or chemical adsorbents such as hydrotalcites and limestone and (c) membrane-based separations depending on the selective channel of CO_2 (polymers and ceramics).

Amine absorption is the widely developed commercial technology for CO_2 removal. However, scientific community is actively involved in search for alternate technologies due to high energy requirement for the amine absorption process in addition to corrosive nature of the solvents as well as costly equipment used for absorption. Separation processes based on TSA or PSA (VSA) using well-engineered physisorbents at the molecular level (most often zeolites and activated carbons, but also amine-functionalized silicas) are visualized as future strategies for CO_2 separation at low gas flow streams [**17-22**]. Membrane based separation has also received considerable focus in recent years for CO_2 separation.

1.5. Requirement of Alternative Technique

1.5.1. Adsorbent technology for CO_2 capture

Due to the higher cost of regeneration process in amine absorption process, regenerable solid adsorbents appear to be alternative for CO_2 adsorption over the conventional methods. Adsorption technologies depend on the different physical repulsion or attraction forces between the sorbent and sorbate species, allowing the separation of different components in a gas mixture based on the different affinities. Physical adsorbents based on carbons [**23-24**], metal organic frameworks (MOF) [**25-27**], surface-functionalized silicas [**28-31**] and zeolites [**32-36**] are able to reversibly adsorb large quantity of CO_2 at room temperature.

Adsorption-based technologies contain two basic steps. (a) Adsorption step: The X components of a gas mixture containing X & Y are selectively adsorbed on the solid in a packed column at relatively high pressure, leaving the gas stream enriched in Y components ($Y < X$) in the raffinate stream corresponding to the weakly sorbing components. (b) Regeneration or desorption step: The X−Y sorbed components are desorbed from the solid by lowering the pressure (PSA) or the temperature (TSA) inside the column. After this operation, the adsorbent is ready for a further cycle. The gas mixture obtained from the regeneration (the extract) is enriched in the more strongly adsorbed components.

1.5.2. Membrane technology for CO_2 capture

In general terms, the membrane materials for pre- and post-combustion CO_2 capture can be classified into three main families: (i) polymers, (ii) dense or metal membranes, and (ii) porous inorganic membranes (PIMs).

The application of polymer membranes [**37-43**], Mixed Matrix membranes [**44-48**] to CO_2 separation is usually argued as limited due to their insufficient thermal, mechanical, and chemical stabilities and their intrinsic low permeances. The metal membranes, most often based on dense Pd alloys either supported or not on ceramic supports, are applicable for H_2 separation in pre-combustion CO_2 capture applications [**49**].

PIMs include purely inorganic or mineral membrane materials for H_2 and CO_2 separation. These materials can be classified into three different categories such as (a) silicas, (b) zeolites, and (c) MOFs. PIMs show potential for pre- and post-combustion CO_2 capture due to several reasons. Firstly, the higher thermal, chemical, and mechanical stability than polymers, Secondly, potentially longer lifetimes in service and more reduced maintenance costs, higher permeability (usually at the expense of lower separation factors), smaller arrangements and investment costs than polymer membranes etc. Finally, unlike adsorbents, the possibility of operating in continuous mode and treating higher flow rates offers an added value to their industrial implementation. Although PIMs for gas separation are certainly still in an early technological stage, there is a great opportunity to synthesize a new generation of hybrid materials based on functionalized silicas, novel zeolites, and metal−organic frameworks (MOFs) and make transform them into new membranes with suitable functional groups for CO_2 capture via selective adsorption and/ or diffusion [**50-51**].

1.5.3. Difference between adsorption and membrane technology

Despite the success of adsorption based technologies for gas treatment and conditioning in terms of energy economy, these processes are usually restricted to low flow rates and limited by their semi continuous operation mode as in physical/chemical adsorption. The conventional operation of adsorption columns is complicated because it requires at least an adsorption step and a desorption step (accomplished by either reducing the pressure or increasing the temperature). Membranes can overcome this shortcoming by reformulating the adsorbent in a film like configuration, also offering additional selectivity benefits via differences in surface diffusion patterns.

The membranes can also benefit from general concepts of physical/chemical adsorption via functionalization in membrane pores (e.g., impregnation or grafting), offering a piece of creativity for design.

Three main challenges are addressed for improving membrane technologies to promote industrial implementation: (1) the selectivity challenge, (2) the energy challenge, and (3) the productivity challenge. These challenges impose not only the optimization of existing membrane materials, but also the development of new materials with balanced adsorption and diffusion properties for a given CO_2 captures application.

1.6. Ordered Mesoporous Silica (OMS) Materials for CO_2 Adsorption

There are several types of mesoporous inorganic molecular sieves, mesoporous silicas which have uniform pore structure and a high density of silanol groups [**52-53**]. M41S was the first ordered mesoporous silica material to be reported [**54**]. Many ordered mesoporous silica materials such as the families of SBA-n [**55-56**], Fudan University Material (FDU) [**57**], Korea Advanced Institute of Science and Technology (KIT) [**58**], and anionic-surfactant-templated mesoporous silica (AMS) [**59**] have been reported in the application field of adsorption. It has been found that mesoporous silicas such as SBA-15, MCM-41, and MCM-48 are good adsorbents for CO_2, offering good selectivity over other gases like CH_4 and N_2 [**60-61**]. Ordered Mesoporous Silica materials offer scope for surface modification aimed at enhancing CO_2 adsorption compared to microporous materials such as zeolites. Due to the small pore opening for the the microporous materials, the access of functional groups in the pores is limited which might not allow the large target gas molecules to pass through [**62**]. Pure silica surfaces do not provide strong adsorption sites to interact strongly with CO_2 due to the fact that the residual hydroxyl groups on the silica surfaces fail to induce strong interactions with CO_2. However, modification of mesoporous silica can be done with amine functional groups to increase the CO_2 gas-adsorbent interactions [**63-64**]. Due to their large and uniform pore sizes (2-50 nm), ordered mesoporous silica materials are highly suitable for surface modification with aminosilane [**63**]. After modification of the pores with aminosilane, it becomes narrower which can permit a target molecule which has molecular diameter below the range of modified pore size (Figure 1.1). In addition, the high density of silanol groups on the mesoporous silica pore walls is beneficial to the introduction of these aminosilane polymer-containing amino groups [**65**]. The introduction of amine functional groups to these mesoporous materials to create specific interactions with CO_2 has gained importance to overcome the disadvantages of the conventional amine absorption processes [**66**].

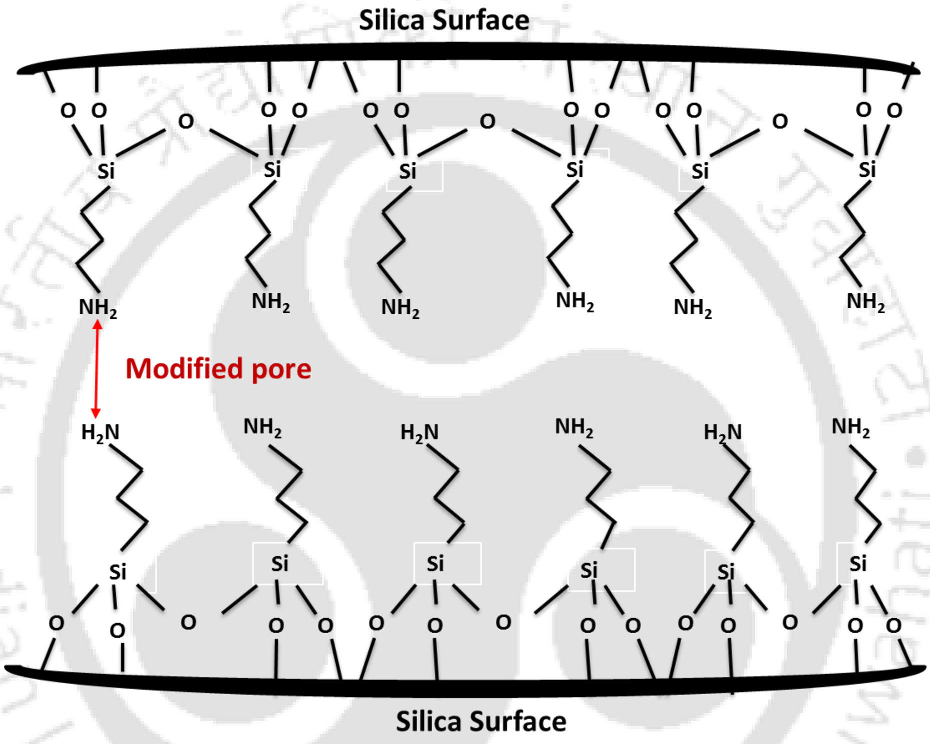

Figure 1.1 Schematic of the 3-APS modified OMS pore structure (not to scale) [**67**].

1.6.1. MCM materials

Since the discovery of the M41S family of mesoporous molecular sieves by Kresge *et al.* [**54**], these materials have received widespread interest in open-structured inorganic materials. Three members of the M41S family of materials have been reported: a hexagonal MCM-41, cubic MCM-48, and lamellar MCM-50 silica phase which are shown in Figure 1.2. Among them, MCM-48 materials attracts great attention for CO_2 adsorption and separation, because MCM-48 are more attractive than MCM-41 due their three dimensional pore structure, which can decrease the diffusion limitation and avoid pore blockage in practical applications.

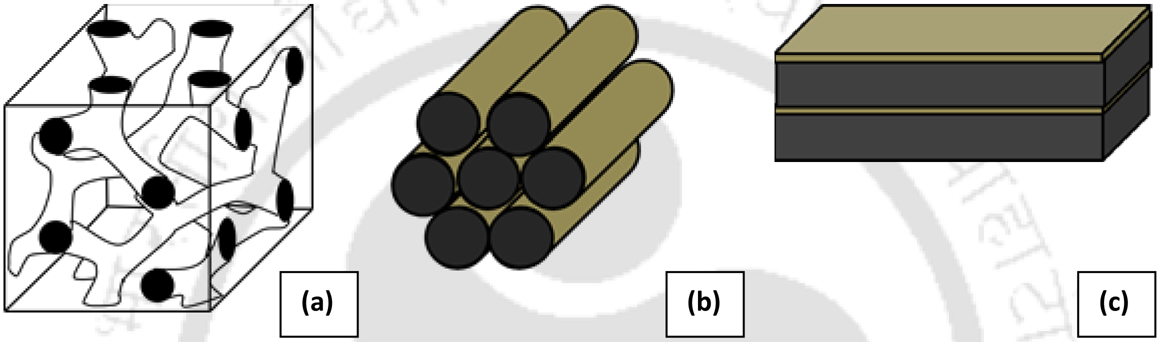

Figure 1.2 Structures of mesoporous M41S materials (a) MCM 48 (b) MCM 41 & (c) MCM 50 [**68**]

1.7. Ordered Mesoporous Silica Membranes for CO_2 Separation

The material for developing a porous membrane should have the convenient affinity with the desired species to separate. In broad sense, the term "affinity" has to be regarded comprising not only the favorable interaction of one or more molecules from a mixture with the solid material, but also their stimulated motion within the porous framework. So at the first step for a membrane design adsorption and diffusion should be maximized.

By preserving the Ordered Mesoporous Silica (OMS) properties, the OMS sieve can be changed into membrane configuration. The mesoporous materials in the form of membrane or thin film could offer number of advantages in CO_2 separation process. As said previously, OMS in membrane configuration allows the CO_2 separation to be operated under steady state condition where adsorption occurs on one side and continuous desorption occurs on the other side. To enhance the separation efficiency of CO_2 from a mixture of other gases, it is desired to functionalize the pores of the membrane with amine groups. The pore size of membrane can thus be tuned as per our requirement.

The performance of membranes is related to their permselectivity/separation factor and also to their permeability. For the microporous membranes, the thickness of the separative layer must be thin enough to reach attractive fluxes with experimentally acceptable trans membrane pressure. On the contrary, the mechanical strength of the membrane must be large enough to withstand the applied pressure. These considerations led to the concept of an asymmetric structure based on a macroporous support and successive layers with decreasing thickness and pore size.

OMS membrane can be formed on a macro porous support by two different techniques such as (i) Hydrothermal method & (ii) Evaporation Induced Self Assembly (EISA) method. There are certain issues associated with the preparation of silica membranes like defect formation due to preparation, thermal cracking during heat treatment which affect membrane reproducibility. The details about these methods are discussed in Chapter 5. The porous supports play a significant role in formation of ordered mesoporous silica membrane in different techniques. Different types of supports such as α-alumina, vycor glass, and γ-alumina can be used to synthesize the ordered mesoporous silica membranes in both the techniques.

The focus of this thesis is to investigate the potential of OMS materials applicability for the energy-efficient and effective separation of CO_2 and N_2 in the membrane process.

1.8. Literature Review

1.8.1. Literature review on adsorption based CO_2 capture

Adsorption appeared an attractive technology for the removal of CO_2 from flue gas or from other gas mixture containing CO_2. Silica (SiO_2) exhibits unique properties related to the ability of its elemental structure, that is, SiO_4 tetrahedra, to be connected together to give rise to a large number of different amorphous or crystallized solids which can be microporous, mesoporous, or macroporous. Ordered mesoporous silica materials known as M41S which included MCM-41, MCM-48, and MCM-50 have attracted increasing attention in separation and catalysis [**54**]. The range of uniform pore size and the high density of silanol groups of these materials are beneficial to the introduction of functional groups with a high coverage, and amine functional groups are one of the most prominent chemical functionalities in this field. MCM-48 with cubic Ia3d symmetry possesses a discontinuous structure centered on gyroid minimal surface that divides the available pore space into two nonintersecting sub volumes. Such a special structure makes the mass-transfer faster in MCM-48 than that in MCM-41 and as a result, MCM-48 is a promising material for gas separation applications.

Tailoring pore properties of mesoporous materials has been examined by many research groups [**66, 69-71**]. The amine functional groups employed in modifying the mesoporous surface included aliphatic primary amines, aromatic primary amines [**66**] and polymeric amines [**71**]. There are very limited reports available on CO_2 adsorption over modified MCM-48.

Gil et al. [**72**] synthesized cubic MCM-48 material and functionalized the MCM 48 material with 3-aminopropyltriethoxysilane (APTES) under different conditions to study CO_2 adsorption capacity. They found that CO_2 adsorption in amino modified materials involved both chemisorption and physisorption. They reported the maximum CO_2 adsorption capacity of 1.68 mmol/g at 1 atm pressure.

Kim et al. [**66**] studied CO_2 adsorption over various amines functionalized MCM-48. Four different types of amines which include aminopropyl (monomeric, unhindered), pyrrolidinepropyl (monomeric, hindered), polymerized aminopropyl (polymeric, unhindered) groups and PEI (polymeric, hindered) were used by them. They reported 0.8 mmol/g of CO_2 adsorption for 3-aminopropyltriethoxysilane. They found that although the MCM-48 silica containing polymeric amines showed a high concentration of amine sites, the monomeric aminopropyl-attached MCM-48 displayed the highest CO_2 adsorption rate at room temperature, because of greater accessibility of amine adsorption sites. APS-MCM-48 also displayed high equilibrium selectivity in adsorptive CO_2/N_2 separation indicating the promise of these molecularly engineered materials for adsorptive separation of CO_2. They finally concluded that in addition to the concentration of surface-attached amino groups, specific interactions between CO_2 and the surface amino groups and the resultant pore structure after amine group attachment have a significant impact on CO_2 adsorption properties of the adsorbent materials.

Huang et al. [**70**] made a comparative investigation on the performance of (3-APS) grafted MCM 48 and xerogel towards CO_2 adsorption. Huang and Yang [35] studied an amine-grafted MCM-48 and reported that the amount of CO_2 adsorbed reached 2.05 mmol/g of adsorbent at 1 atm and 25^oC. It was concluded that the variation in the adsorption capacity was attributed to the amine loading capacity of both the support materials. AP-MCM-48 exhibited amine loading of ~2.3 mmol (N)/g, which was 26% higher than AP-xerogel (~1.7 mmol/g), thereby leading to improved efficiency for CO_2 adsorption.

Ma et al. [**73**] worked on polyethyleneimine (PEI) impregnated MCM-41 for CO_2 adsorption and created the term “molecular basket” for the resultant composite adsorbent. They reported that with respect to loading, the CO_2 adsorption capacity of PEI-impregnated MCM-41 was found to be increased. CO_2 adsorption capacity of ~3.02 mmol/g was reported for PEI-impregnated MCM-41 under a stream of 100% CO_2 (75^oC, 1 bar) for PEI loading of 75 wt%. The optimum amount of PEI that can be loaded in MCM-41 was found to be 50 wt% based on the amine efficiency of the composite adsorbent. The 50 wt% PEI loaded MCM-41 exhibited an adsorption capacity of ~2.0 mmol/g under a stream of 15% CO_2/air mixture. It was reported that unlike other amine functionalized adsorbent, PEI-impregnated MCM-41 composite showed an interesting behaviour that the CO_2 adsorption capacity increased with respect to temperature (25 to 75 ^oC). The enhancement in the adsorption capacity observed with rise in temperature was concluded to be due to the occurrence of a bulk-like state of PEI inside the mesopores. Further, it was mentioned that when PEI is present in bulky state, amine groups are not readily accessible for CO_2 at low temperature, resulting in a diffusion-limited process.

Son et al. [**71**] investigated the CO_2 adsorption characteristics of PEI (50 wt%) impregnated using five different silica materials. Interestingly, it was observed that all the silica materials used in their study for impregnation process exhibited variation in the CO_2 adsorption capacity. They revealed that the pore diameter of the silica materials used for impregnation process, have the significant effect on the adsorption capacity. It was observed that CO_2 adsorption capacity increased in the order of KIT-6>SBA-15~SBA-16>MCM-48>MCM-41, which corresponds to the order of average pore diameter of the bare materials (6.5, 5.5, 4.1, 3.1 and 2.8 nm respectively). They further noticed the similar trend for the time required for each PEI impregnated adsorbent to reach 90% of its equilibrium capacity.

Knowles et al. [**74**] explored the suitability of amorphous silica gel and hexagonal mesoporous silica (HMS) for amine tethering. 3-APS modified with HMS showed a higher adsorption capacity of 1.59 mmol/g (20 ^oC, 0.9 bar) in comparison to 3-APS modified with silica gel (0.68 mmol/g) under the similar conditions. In the case of 3-APS-HMS, 52 % higher amine loading was observed compared to 3-APS-silica gel. They concluded that due to the difference in surface areas of HMS (1198 m^2/g) compared to amorphous silica (567 m^2/g), the adsorption capacities as well as loadings varied.

Knofel et al. [**75**] grafted N-[3- (trimethoxysilyl)propyl] ethylenediamine (DP) on SBA-16 silica based on the assumption that the occurrence of two amine groups per carbon chain may lead to enhanced CO_2 adsorption efficiency. They observed that after grafting of DP into SBA-16 silica material provided an adsorption capacity of ~1.4 mmol/g (27^{o}C, 1 bar). It was found that the amine efficiency of 3-APS functionalized silica adsorbents to be higher than DP functionalization.

Zelenak et al. **[76]** investigated the effect of pore size on the performance of amine-functionalized adsorbents for CO_2 capture. In their study, MCM-41 and SBA-15 with a pore size of 3.3 nm and 7.1 nm, respectively, were used as base materials. 3-APS was tethered onto that two different mesoporous silica supports. The 3-APS functionalized SBA-15 and 3-APS-MCM-41 exhibited CO_2 adsorption capacity of ~1.54 mmol/g, and ~0.57 mmol/g (20 °C, 0.1 bar), respectively. It was concluded from the study that variation in the adsorption capacity exhibited by the two adsorbents was attributed to the pore size and amine surface density. The mesoporous silica support SBA-15 with larger pore size was reported to possess higher amine surface density (2.4 (N)/nm in comparison to AP-MCM-41 having amine density of only 1.1 (N)/nm^2.

Hiyoshi et al. [**77**] made a comparative investigation on the adsorption characteristics of amine-grafted SBA-15 by using three different amines including 3-APS, DP and TP (N-[3-(trimethoxysilyl)propyl] diethylenetriamine). The study demonstrated that higher amine density resulted through tri amine bearing species led to synthesis of best performing adsorbent. TP-SBA-15 had been reported with CO_2 adsorption capacity of ~1.58 and ~1.80 mmol/g, respectively, under dry and humid streams. Moreover, the adsorbent was also reported to be stable for more than 50 adsorption-desorption cycles when subjected to regeneration at 100 °C.

1.8.2. Literature review on membrane based CO_2 separation

A good membrane for gas separation should have both high selectivity and permeation of target gas molecule. The performance of membrane can be determined through its permeance/permeability and separation factor/selectivity. There are two widely applicable techniques for synthesizing mesoporous silica membranes. Hydrothermal process and EISA (Evaporation Induced self-assembly) are those techniques which are widely used. The details of these processes are described in Chapter 2. In both techniques the mesoporous silica membranes are synthesized on a macroporous support to enhance their mechanical stability. The hydrothermal synthesis technique is mostly reported in literature to fabricate ordered mesoporous silica membranes [**78-87**]. In EISA process the preparation of thin films and membranes by spin-coating require flat supports. Some limited studies have reported synthesis of mesoporous silica membranes by spin-coating on porous alumina substrates [**79, 88-90**].

There have been extensive studies on the synthesis of mesoporous silica membranes with two-dimensional hexagonal structure [**91-94**]. However, the application of the hexagonal mesoporous silica membrane for gas separation is restricted to its uni-dimensional pore channels [**95**]. The mesoporous silica membranes with three-dimensional structure have been studied in recent years [**79-80, 83**].

McCool et al. [**81**] fabricated mesoporous silica membranes via sol dip-coating and hydrothermal synthesis deposition technique onto a polished surface of a macroporous α-alumina disk. They reported that the silica layer formed from dip-coating method appeared to be much more uniform than those of the hydrothermal method. Sakamoto et al. [**79**] also reported preparation of mesoporous silica membranes on porous alumina supports by spin-coating method as well as hydrothermal method. The supports used were asymmetric alumina disks consisting of a thin dense top layer with an average pore diameter of 70 nm and a support layer with a pore diameter of 700 nm. They also observed similar nature of the synthesized membranes. They reported thinner and homogeneous mesoporous silica layer in spin coating technique compared to hydrothermal process on the alumina support. Nishiyama et al. [**84**] investigated a membrane made of MCM-48 with a three-dimensional pore structure deposited on a porous alumina support under hydrothermal conditions. In the above three papers single gas permeation experiments showed the gas permeation for H_2, N_2, Ar, O_2, CO_2 and He for mesoporous silica membranes is governed by Knudsen diffusion [**81-82**]. Kumar et al. [**82**] also synthesized MCM 48 membrane on two different supports by hydrothermal synthesis having different pore size. They found that the support having smaller surface pore size gives better quality membrane. There are several other studies have reported reproducible synthesis of high-quality dip-coated mesoporous silica membranes on α-alumina and γ-alumina supports [**81, 88, 96-99**].

So far, very few studies are reported on the amine-functionalized OMS membranes. The development of amine-functionalized OMS membrane is still in very early stage of research and thus need immediate attention by the researchers. A few studies have recently appeared in the literature on the functionalization of mesostructure silica membranes for CO_2 separation. McCool et al. [**81**] explored three different strategies to functionalize mesoporous silica membranes. The membranes were functionalized by atomic layer deposition (ALD) with amino propyl di-methyl ethoxysilane (APDMES), ethylene diamine (EDA) assisted APDMES ALD and direct attachment of APS from the liquid phase. The CO_2 permeance of EDA-APDMES ALD membranes was higher than that of the membranes modified with APTES even though the relative concentration of amino groups was the lowest for the APTES membranes. They suggested that polymerization of APTES within the membrane pores caused a decrease in the pore diameter, thereby limiting the CO_2 permeance. They suggested that the high loading of amino groups which minimizes the interactions with silica surface, promote the rate of CO_2 transport.

Sakamoto et al. [**79**] showed that amine-functionalized OMS membrane is another potential research field worth to be studied for CO_2 separation. They modified MCM-48 membranes by 3-aminopropyltrimethoxysilane (3-APS) groups via post synthesis grafting method. They reported that the separation performance for CO_2/N_2 (20/80) gas mixture was greatly improved after amine modification of the pure MCM 48. It was found by them that at pressure difference 150 kPa and 373 K temperature, the CO_2 selectivity over N_2 was increased from 0.8 for pure MCM 48 membrane to 800-50 for amine functionalized membrane. They also found that spin-coated membrane was performing better for CO_2 selective membrane compared to hydrothermal membrane. The CO_2 permeance values for amine-modified hydrothermally synthesized and spin coated membranes were reported to be 4.7×10^{-10} and 1×10^{-9} mol/m^2 s Pa, respectively. These values were much lower than the CO_2 permeance for hydrothermally synthesized and spin coated membranes without any amine functionalization.

Kumar et al. [**80**] described modification of MCM-48 membranes with a polymer, polyethyleneimine (PEI), containing primary, secondary and tertiary amino groups. They found N_2 selective (over CO_2) membrane unlike Sakamoto et al. [**79**]. They performed binary CO_2/N_2 permeation experiments in the absence and presence of ~2.6 vol.% water vapour. The separation efficiency (N_2 selective) was found to be 1.25. In the presence of water vapour the binary gas (CO_2/N_2) permeation results showed higher N_2 selective membrane and the selectivity was found to be 80 for the highest CO_2 feed concentration (80%). Increased N_2/CO_2 separation factors were observed with an increase in CO_2 concentration in the feed mixture. The gas permeances were found to be extremely low (<0.1 $nmol \cdot m^{-2} \cdot s^{-1} \cdot Pa^{-1}$) by them. The high N_2/CO_2 selectivity for the PEI/MCM-48 membranes was observed at room temperature. They found that the separation performance was reduced with increase in temperature. In the presence of water vapour at higher temperature the separation performance was also not improved. Very low N_2/CO_2 separation factors (~3.5) were observed even at the highest CO_2 concentration (80 vol.%) in the feed at 363 K.

Ostwal et al. [**67**] also reported the preparation of well inter grown membranes based on 3-APS-grafted vycor membranes showing CO_2 permeance (0.22 $nmol \cdot m^{-2} \cdot s^{-1} \cdot Pa^{-1}$). They found lower CO_2/N_2 separation factor (up to 10) at 100 ^oC for a 20% (v/v) CO_2 feed composition compare to Sakamoto et al. [**79**]. They described the formation of surface carbamate species. The membranes displayed an improved permeation and separation performance at higher temperatures and lower CO_2 compositions in the feed stream. The authors attributed these observations to a lower stability of carbamate species and increased CO_2 diffusion at higher temperatures and to a higher saturation of carbamate species at higher pressures, hampering the hopping of CO_2 molecules within the membrane by closing down the pores. Evidence of the formation of carbamate species in 3-APS-grafted silica membranes was provided by Ostwal et al. [**67**] using DFT calculations.

The result reported by Sakamoto et al. [**79**] was in agreement with the studies reported by Kim [**100**] on the 3-APS functionalised MCM 48 membranes. It was found by Kim et al. [**100**] that the amine-functionalized MCM 48 exhibited slight greater CO_2/N_2 separation factor which is to be ~0.96 compared to that of pure MCM-48 (0.89). They also observed that the CO_2 permeance dropped from 9.8×10^{-8} $mol.m^{-2}s.Pa$ to 2.5×10^{-8} $mol.m^{-2}s.Pa$ when MCM-48 was functionalized with amine group.

Xomeritakis et al. [**101**] synthesized microporous sol-gel derived aminosilicate membrane by using 3-APS. They performed single gas permeation analysis for CO_2 with varying feed pressure. It was reported that the CO_2 permeance increased drastically when the CO_2 feed pressure was reduced to 1-2 kPa. They explained that CO_2 can diffuse fast through the membrane pore wall due to small coverage of CO_2 at lower CO_2feed partial pressure whereas at higher CO_2 feed partial pressure, the coverage of CO_2 in the pore wall reaches a saturation level. Due to this the membrane pore size gets decreased for adsorbed CO_2 monolayer and hence lower the permeation.

1.9. Importance and Objectives of the Present Study

From the discussion in the previous section, it is apparent that amine-functionalized ordered mesoporous silica materials have immense industrial significance and there is huge scope of research. The main target of this thesis is to study the CO_2 separation performance for the amine functionalized ordered mesoporous silica materials in adsorption based technology as well as membrane based technology.

This research work has been undertaken with the following objectives:

- Synthesis of OMS (MCM-48) materials by basic route and functionalize the materials with different amines such as 3-aminopropyl tri methoxy silane (3-APTMS), 3-amino propyl tri ethoxy silane (3-APS) and 3-(2-aminoethylamino) propyl tri methoxy silane (3-2-Am).
- Characterization of the materials by thermo gravimetric analysis (TGA), Fourier transforms infra-red spectroscopy (FTIR), X-ray diffraction (XRD) analysis, etc.
- Selection of the type of amine based on highest CO_2 adsorption capacity.
- To find out the optimum dose of amine for functionalization of OMS (MCM-48) materials to obtain highest CO_2 separation performance.
- Synthesis of OMS materials by acidic route and make a comparative study with the OMS materials obtained by basic route for CO_2 adsorption.
- Synthesis and characterization of best quality porous α-alumina support to form crack-free ordered mesoporous silica membrane by spin coating method.
- Synthesis and characterization of ordered mesoporous silca membrane by spin-coating method.
- Functionalization of the OMS membrane by the selected amine and study the performance for CO_2 separation from CO_2/N_2 gas mixture.

To know the inner detail of surface characteristics and the CO_2 adsorption capacities of the amine-functionalized ordered mesoporous silica materials, the powder form of the materials are studied. The functionalization of the OMS (MCM 48) materials is performed by using four different amines. The amine, which gives the highest CO_2 adsorption capacity using amine-functionalized OMS, is chosen for further study. The effects of amine loading as well as the temperature on the CO_2 adsorption capacity by amine funtionalized OMS materials are studied. After inheriting the concept of amine-functionalized ordered mesoporous silica materials for CO_2 adsorption, we finally introduced the OMS material in more energy saving membrane application. The ordered mesoporous silica membrane is successfully synthesized on porous α-alumina support. Finally, performance studies are investigated and analysed by using binary gas mixture (CO_2/N_2).

1.10. Thesis Outline

The work described in this thesis develops the science and engineering of mesoporous silica materials as well as membranes for molecular transport and separations. A number of significant challenges along this path were addressed by a strategy that combined new approaches for supported membrane fabrication, amine-functionalization, gas separations application, surface property investigations, and characterization techniques. These investigations have addressed several challenges of mesoporous silica membrane technology and created opportunities for applying mesoporous silica materials in a scalable membrane separation platform.

The doctoral thesis is organized in seven chapters as follows:

Chapter 1: This chapter presents a brief overview of global warming and greenhouse gas effect. It also discusses their origin, impacts on environment structure, Indian scenario, guidelines and need for removal of excess quantity and the available CO_2 capture techniques, merits and demerits of each treatment techniques and the requirement of easiest low-cost treatment technique to capture CO_2 from fossil fuel fired emission. Also, this chapter describes the detail literatures studied for the removal of CO_2 using adsorbent based technology as well as membrane based technology focused on ordered mesoporous silica for CO_2 separation. The final part of this chapter highlights the importance and draws clear objectives of this research work.

Chapter 2: This chapter includes some theory related to adsorption and isotherm modeling. The valuation of important parameters such as Henry's constant, adsorption enthalpy and selectivity predictions using Ideal Adsorbed Solution Theory (IAST) are presented. This chapter presents several topics and discussion to provide important background information for this research project. First, the basic principles of the sol-gel technology are explained. After that, the differences between conventional sol-gel synthesis and template-directed synthesis are explained and more specific comments on templated silica structures are given**.** This chapter describes the various reaction mechanisms between CO_2 and aminosilane. It also describes the separation characteristics of different types of porous membrane based on their pore sizes. The membrane based theories are also included.

Chapter 3: This chapter elaborates the detailed studies including the synthesis and characterization of OMS (MCM 48) materials. The amine-modified ordered mesoporous silica (OMS) powder is a good reference material for estimating membrane properties. Their surface characteristics for CO_2 adsorption and separation are performed and elaborated. The OMS materials were functionalized with three different amines. The effects of grafting of different amines on OMS materials for its CO_2 adsorption characteristics are investigated. The CO_2 isotherms at 30^oC are measured up to 10 bar on different amine loaded OMS samples to systematically evaluate the effect of amine on CO_2 adsorption capacity. Effect of temperature is also examined to understand whether physisorption or chemisorption dominates for amine loaded samples. Modeling of CO_2 isotherms is also carried out to get molecular level insight and to calculate Henry's constants.

Chapter 4: This chapter describes the synthesis and characterization for the OMS materials obtained by two different routes such as acidic and basic routes and compares the CO_2 adsorption capacity for those materials. The OMS materials are characterized by using N_2 adsorption-desorption analysis, TGA analysis, XRD analysis, FTIR analysis and TEM analysis. The CO_2 isotherms at 30 ^oC are measured up to 8 bars for OMS samples to find out CO_2 adsorption capacity. CO_2 adsorption studies show better results for OMS materials obtained by acidic route.

Chapter 5: To produce a thin continuous or crack-free ordered mesoporous silica membrane by spin-coating method onto a porous α-alumina disc support, the support should have high quality surface. This chapter presents the detailed study regarding the influence of compaction load and sintering temperature on the surface quality of the α-alumina disc support were investigated by using different characterization techniques including FESEM, flexural strength, XRD, N_2 gas permeation, density/porosity and shrinkage analysis. By using these analyses, the proper sintering temperature and compaction load was established for synthesizing crack-free ordered mesoporous silica membrane.

Chapter 6: In this section, we showed that amine-modified OMS can be used for membrane. We synthesized defect-free OMS membrane. We studied the dependency of support properties for synthesizing the defect-free ordered mesoporous silica membrane. The defect-free membrane was functionalized by 3-aminopropyl groups. The performance study of the amine-modified membrane was performed by using binary gas permeation and analysed to achieve high CO_2 separation factor.

Chapter 7: This chapter draws appropriate conclusions based on this study. This chapter also provides some useful recommendations for future research in the relevant field.

References

[1] UK Stern Review, **2005.** *http://www.hm-treasury.gov.uk/ sternreview_index.htm (accessed on 01/05/2013).*

[2] Pachauri, R. K.; Reisinger, A.; Eds. Fourth Assessment Report on Climate Change; *International Panel on Climate Change: Geneva, Switzerland,* **2007.**

[3] Raupach, M. R.; Marland, G.; Ciais, P.; Le Quéré, C.; Canadell, J.G.; Klepper, G.; Field, C. B. Global and regional drivers of accelerating CO_2 emissions, *Proc. Natl. Acad. Sci. U.S.A.* **2007,** *104,* 10288-10293.

[4] Van der Hoeven, M. CO_2 Emissions from Fuel Combustion: Highlights; Organisation for Economic Co-operation and Development/ International Energy Agency (OECD/IEA): *Paris,* **2012.**

[5] Richert, P. Qualité de l’Air et Changement Climatique: un Même Defí , une Mem̂e Urgence. Une Nouvelle Gouvernance pour l’Atmospher̀e; Special Report of the French Conseil National de l’Air on occasion of the 10th anniversary of the French Loi de l’Air et l’Utilisation Rationnelle de l’Energie; *Paris,* **2007.**

[6] UNFCCC Kyoto Protocol, revised **2013.** http://unfccc.int/ kyoto_protocol/items/ 2830.php (accessed on 01/05/2013).

[7] Greenhouse Gas Emission Trends and Projections in Europe 2006; EEA Report No. 9/2006; Office for Official Publications of the European Communities: Copenhagen, *Denmark,* **2006.**

[8] IEA. CO_2 capture and storage: a key carbon abatement option. Paris, France: International Energy Agency; **2008.**

[9] Ghoniem, A.F. Needs, resources and climate change: clean and efficient conversion technologies. *Prog Energy Combust* **2011,** *37,* 15-51.

[10] Kuramochi, T.; Ramírez, A.; Turkenburg, W.; Faaij, A. Comparative assessment of CO_2 capture technologies for carbon-intensive industrial processes. *Prog Energy Combust* **2012,** *38*, 87-112.

[11] Climate change. In: Pachauri R. K, Reisinger A, editors. Synthesis report contribution of working groups I, II and III to the fourth assessment report of the intergovernmental panel on climate change. *Geneva, Switzerland: IPCC*. **2007,** p.104.

[12] Figueroa, J. D.; Fout, T.; Plasynski, S.; McIlvried, H.; Srivastava, R.D. Advances in CO_2 capture technology-The U.S. Department of Energy's carbon sequestration Program. *Int J Greenhouse Gas Con*. **2008,** *2,* 9-20.

[13] Scholes, C. A.; Smith, K. H.; Kentish, S. E; Stevens, G. W. CO_2 capture from precombustion processes-Strategies for membrane gas separation. *Int. J. Greenhouse Gas Con.* **2010,** *4*, 739-755.

[14] Bredesen, R.; Jordal, K.; Bolland, O. High temperature membranes in power generation with CO_2 capture, *Chem. Eng. Process.* **2004,** *43,* 1129-1158.

[15] Aaron, D.; Tsouris, C. Separation of CO_2 from flue gas: A review, *Sep. Sci. Technol.* **2005,** *40,* 321-348.

[16] MacDowell, N.; Florin, N.; Buchard, A.; Hallett, J.; Galindo, A.; Jackson, G.; Adjiman, C. S.; Williams, C. K.; Shah, N.; Fenell, P. An overview of CO_2 capture technologies, *Energy Environ. Sci.* **2010,** *3,* 1645-1669.

[17] D'Alessandro, D. M.; Smit, B.; Long, J. R. Carbon Dioxide Capture: Prospects for New Materials, Angew. *Chem., Int. Ed.* **2010,** *49*, 6058-6082.

[18] Sumida, K.; Rogow, D. L.; Mason, J. A.; McDonald, T. M.; Bloch, E. D.; Herm, Z. R.; Bae, T. H.; Long, J. R. Carbon dioxide capture in metal-organic frameworks, *Chem. Rev.* **2012,** *112*, 724-781.

[19] Tagliabue, M.; Farrusseng, D.; Valencia, S.; Aguado, S.; Ravon, U.; Rizzo, C.; Corma, A.; Mirodatos, C. Natural gas treating by selective adsorption: Material science and chemical engineering interplay, *Chem. Eng. J.* **2009,** *155*, 553-566.

[20] Li, J. R.; Ma, Y.; McCarthy, M. C.; Sculley, J.; Yu, J.; Jeong, H. K.; Balbuena, P. B.; Zhou, H. C. Carbon dioxide capture-related gas adsorption and separation in metal-organic frameworks, *Coord. Chem. Rev.* **2011,** *255*, 1791-1823.

[21] Arumkumar, S.; Zhao, A.; Shimizu, G. K. H.; Sarkar, P.; Gupta, R. Post-Combustion CO_2 Capture Using Solid Sorbents: A Review, *Ind. Eng. Chem. Res.* **2012,** *51*, 1438-1463.

[22] Drage, T. C.; Snape, C. E.; Stevens, L. A.; Wood, J.; Wang, J.; Cooper, A. I.; Dawson, R.; Guo, X.; Satterley, C.; Irons, R. Materials challenges for the development of solid sorbents for post-combustion carbon capture, *J. Mater. Chem.* **2012,** *22*, 2815-2823.

[23] An, H.; Feng, B.; Su, S. CO_2 capture by electro thermal swing adsorption with activated carbon fibre materials, *Int. J. Greenh. Gas. Con.* **2011,** *5*, 16-25.

[24] Zhou, X.; Yi, H.; Tang, X.; Deng, H.; Liu, H. Thermodynamics for the adsorption of SO_2, NO and CO_2 from flue gas on activated carbon fiber, *Chem. Eng. J.* **2012,** *200-202,* 399-404

[25] Férey, G.; Serre, C.; Devic, T.; Maurin, G.; Jobic, H.; Llewellyn, P. L.; DeWeireld, G.; Vimont, A.; Daturi, M.; Chang, J. S. Why hybrid porous solids capture greenhouse gases? *Chem. Soc. Rev.* **2011,** *40*, 550-562.

[26] D'Alessandro, D. M.; Smit, B.; Long, J. R. Carbon Dioxide Capture: Prospects for New Materials. *Angew. Chem., Int. Ed.* **2010,** *49*, 6058-6082.

[27] Li, J. R.; Ma, Y.; McCarthy, M. C.; Sculley, J.; Yu, J.; Jeong, H. K.; Balbuena, P. B.; Zhou, H. C. Carbon dioxide capture-related gas adsorption and separation in metal-organic frameworks. *Coord. Chem. Rev.* **2011,** *255*, 1791-1823.

[28] Beck, J. S.; Vartuli, J. C.; Roth, W. J.; Leonowicz, M. E.; Kresge, C. T.; Schmitt, K. D.; Chu, C. T. W.; Olson, D. W.; Sheppard, E. W.; McCullen, S. B.; Higgins, J. B.; Schlenkert, J. L. A New Family of Mesoporous Molecular Sieves Prepared with Liquid Crystal Templates. *J. Am. Chem. Soc.* **1992,** *114*, 10834-10843.

[29] Sayari, A.; Yang, Y. Expanding the Pore Size of MCM-41 Silicas: Use of Amines as Expanders in Direct Synthesis and Post Synthesis Procedures. *J. Phys. Chem. B* **1999,** *103*, 3651-3658.

[30] Sayari, A.; Hamoudi, S. Periodic Mesoporous Silica-Based Organic-Inorganic Nanocomposite Materials, *Chem. Mater.* **2001,** *13*, 3151-3168.

[31] Loganathan, S.; Tikmani, M.; Ghoshal, A. K. Novel Pore-Expanded MCM-41 for CO_2 Capture: Synthesis and Characterization, *Langmuir*. **2013,** *29*, 3491-3499.

[32] Dunne, J. A.; Rao, M.; Sircar, S.; Gorte, R. J.; Myers, A. L. Calorimetric heats of adsorption and adsorption isotherms. 2. O_2, N_2, Ar, CO_2, CH_4, C_2H_6, and SF_6 on NaX, H-ZSM-5, and Na-ZSM-5 zeolites, *Langmuir.* **1996,** *12*, 5896-5904.

[33] Barrer, R. M.; Gibbons, R. M. Zeolitic carbon dioxide: energetics and equilibria in relation to exchangeable cations in faujasite, *Trans. Faraday Soc.* **1965,** *61*, 948-961.

[34] Li, S.; Falconer, J. L.; Noble, R. D. SAPO-34 membranes for CO_2/CH_4 separation *J. Membr. Sci.* **2004,** *241*, 121-135.

[35] Cui, Y.; Kita, H.; Okamoto, K. I. Preparation and gas separation performance of zeolite T membrane, *J. Mater. Chem.* **2004,** *14*, 924-932.

[36] Himeno, S.; Tomita, T.; Suzuki, K.; Nakayama, K.; Yajima, K.; Yoshida, S. Synthesis and Permeation Properties of a DDR-Type Zeolite Membrane for Separation of CO_2/CH_4 Gaseous Mixtures, *Ind. Eng. Chem. Res.* **2007,** *46*, 6989-6997.

[37] Kaldis, S. P.; Skoras, G.; Sakellaropoulos, G. P. Energy and capital cost analysis of CO_2 capture in coal IGCC processes via gas separation membranes, *Fuel Process. Technol.* **2004,** *85*, 337-346.

[38] Bernardo, P.; Drioli, E.; Golemme, G. Membrane Gas Separation: A Review/State of the Art, *Ind. Eng. Chem. Res.* **2009,** *48*, 4638-4663.

[39] Corti, A.; Fiaschi, D.; Lombardi, L. Carbon dioxide removal in power generation using membrane technology, *Energy* **2004,** *29,* 2025-2043.

[40] Koros, W. J.; Mahajan, R. Pushing the limits on possibilities for large scale gas separation: which strategies?, *J. Membr. Sci.* **2001,** *175,* 181-196.

[41] Basu, S.; Khan, A. L.; Cano-Odena, A.; Liu, C.; Vankelecom, I. F. Membrane-based technologies for biogas separations, *J. Chem. Soc. Rev.* **2010,** *39*, 750-768.

[42] Mondal, A.; Mandal, B. Synthesis and characterization of crosslinked poly (vinyl alcohol)/poly (allylamine) / 2-amino-2-hydroxymethyl-1, 3-propanediol / polysulfone composite membrane for CO_2/N_2 separation, *J. Membr. Sci.* **2013,** *446,* 383-394.

[43] Mondal. A.; Mandal, B. CO_2 separation using thermally stable crosslinked poly (vinyl alcohol) membrane blended with polyvinyl pyrrolidone / polyethyleneimine / tetraethylene pentamine, *J. Membr. Sci*. **2014,** *460,* 126-138.

[44] Reid, B. D.; Ruiz-Trevino, F. A.; Musselman, I. H.; Balkus, K. J. Jr.; Ferraris, J. P. Gas Permeability Properties of Polysulfone Membranes Containing the Mesoporous Molecular Sieve MCM-41, *Chem. Matter.* **2001,** *13,* 2366-2373.

[45] Casado-Coterillo, C.; Soto, J.; Jimaré, M. T.; Valencia, S.; Corma, A.; Téllez, C.; Preparation and characterization of ITQ-29/polysulfone mixed-matrix membranes for gas separation: Effect of zeolite composition and crystal size, *J. Chem. Eng. Sci.* **2012,** *73,* 116-122.

[46] Huang, Z.; Li, Y.; Wen, R.; Teoh, M. M.; Kulprathipanja, S. Enhanced gas separation properties by using nanostructured PES-Zeolite 4A mixed matrix membranes, *J. Appl. Polym. Sci.* **2006,** *101*, 3800-3805.

[47] Hussain, S.; Koros, W. J. Mixed matrix hollow fiber membranes made with modified HSSZ-13 zeolite in polyetherimide polymer matrix for gas separation, *J. Membr. Sci.* **2007,** *288*, 195-207.

[48] Nishiyama, N.; Momose, W.; Egashira, Y.; Ueyama, K. Partially carbonized polyimide membranes with high permeability for air separation, *J. Chem. Eng. Jpn.* **2003,** *36*, 603-608.

[49] Bredesen, R.; Jordal, K.; Bolland, O. High-temperature membranes in power generation with CO_2 capture, *Chem. Eng. Process.* **2004,** *43*, 1129-1158.

[50] Gascon, J.; Kapteijn, F. Metal-Organic Framework Membranes—High Potential, Bright Future?, *Angew. Chem. Int. Ed.* **2010,** *49*, 1530-1532.

[51] Caro, J. Are MOF membranes better in gas separation than those made of zeolites?, *Curr. Opin. Chem. Eng.* **2011,** *1*, 77-83.

[52] Beck, J. S.; Vartuli, J. C.; Roth, W. J.; Leonowicz, M. E.; Kresge, C. T.; Schmitt, K. D.; Chu, C. T.; Olson, D. H.; Sheppard, E. W.; Mccullen, S. B.; Higgins J. B.; Schlenker, J. L. A new family of mesoporous molecular-sieves prepared with liquid-crystal templates, *J. Am. Chem. Soc.*, **1992,** *114*, 10834-10843.

[53] Zhao, D. Y.; Feng, J. L.; Huo, Q. S.; Melosh, N.; Fredrickson, G. H.; Chmelka, B. F.; Stucky, G. D. Triblock copolymer syntheses of mesoporous silica with periodic 50 to 300 angstrom pores, *Science.* **1998,** *279,* 548-552.

[54] Kresge, C. T.; Leonowicz, M. E.; Roth, W. J.; Vartuli, J. C.; Beck, J. S. Ordered mesoporous molecular-sieves synthesized by a liquid-crystal template mechanism, *Nature.* **1992,** *359,* 710-712.

[55] Hiyoshi, N.; Yogo, K.; Yashima, T. Adsorption of carbon dioxide on amine modified SBA-15 in the presence of water vapor, *Chem. Lett.* **2004,** *33,* 510-511.

[56] Kim, T. W.; Ryoo, R.; Kruk, M.; Gierszal, K. P.; Jaroniec, M.; Kamiya, S.; Terasaki, O. Tailoring the pore structure of SBA-16 silica molecular sieve through the use of copolymer blends and control of synthesis temperature and time,, *J. Phys. Chem. B.* **2004,** *108,* 11480-11489.

[57] Yu, T.; Zhang, H.; Yan, X.W.; Chen, Z. X.; Zou, X. D.; Oleynikov, P.; Zhao, D. Y. Pore structures of ordered large cage-type mesoporous silica FDU-12s, *J. Phys. Chem. B.* **2006,** *110,* 21467-21472.

[58] Ruthstein, S.; Schmidt, J.; Kesselman, E.; Popovitz-Biro, R.; Omer, L.; Frydman, V.; Talmon, Y.; Goldfarb, D. Molecular level processes and nanostructure evolution during the formation of the cubic mesoporous material KIT-6, *Chem. Mater.* **2008,** *20,* 2779-2792.

[59] Yokoi, T.; Yoshitake, H.; Tatsumi, T. Synthesis of anionic-surfactant-templated mesoporous silica using organoalkoxysilane-containing amino groups, *Chem. Mater.* **2003,** *15,* 4536-4538.

[60] Qi, G. G.; Wang, Y. B.; Estevez, L.; Duan, X. N.; Anako, N.; Park, A. H. A.; Li, W.; Jones, C. W.; Giannelis, E. P. High efficiency nanocomposite sorbents for CO_2 capture based on amine-functionalized mesoporous capsules, *Energy Environ. Sci.* **2011,** *4,* 444-452.

[61] Zelenak, V.; Badanicova, M.; Halamova, D.; Cejka, J.; Zukal, A.; Murafa, N.; Goerigk, G. Amine-modified ordered mesoporous silica: Effect of pore size on carbon dioxide capture, *Chem. Eng. J.* **2008,** *144,* 336-342.

[62] Knofel, C.; Descarpentries, J.; Benzaouia, A.; Zelenak, V.; Mornet, S.; Llewellyn, P.L. Functionalised micro-/mesoporous silica for the adsorption of carbon dioxide, *Micropor. Mesopor Mater.* **2007,** *99,* 79-85.

[63] Hiyoshi, N.; Yogo, K.; Yashima, T. Reversible Adsorption of Carbon Dioxide on Amine-Modified SBA-15 from Flue Gas Containing Water Vapor, *Stud Surf Sci Catal.* **2004,** *153,* 417-422.

[64] Knowles, G. P.; Delaney, S. W.; Chaffe, A. I. Amine-functionalised mesoporous silicas as CO_2 adsorbents, *Stud. Surf. Sci. Catal.* **2005,** *156,* 887-896.

[65] Yokoi, T.; Yoshitake, H.; Tatsumi, T. Synthesis of amino-functionalized MCM-41 *via* direct co-condensation and post-synthesis grafting methods using mono-, di- and tri-amino-organoalkoxysilanes, *J. Mater. Chem.* **2004,** *14,* 951-957.

[66] Kim, S.; Ida, J.; Guiants, V. V.; Lin, Y. S. Tailoring Pore Properties of MCM-48 Silica for Selective Adsorption of CO_2, *J. Phys. Chem. B.* **2005,** *109*, 6287-6293.

[67] Ostwal, M.; Singh, R. P.; Dec, S. F.; Lusk, M. T.; Way, J. D. 3-Aminopropyltriethoxysilane functionalized inorganic membranes for high temperature CO_2/N_2 separation, *J. Membr. Sci.* **2011,** *369*, 139-147.

[68] Roth, W. J.; Vartuli, J. C. Synthesis of mesoporous molecular sieves, *Stud. Surf. Sci. Catal.* **2005,** *157*, 91-110.

[69] Inagaki, S.; Fukushima, Y.; Kuroda, K. Synthesis and characterization of highly ordered mesoporous material; FSM-16, from a layered polysilicate, *Stud. Surf. Sci. Catal.* **1994,** *84*, 125-132.

[70] Huang, H. Y.; Yang, R. T.; Chinn, D.; Munson, C. L. Amine-Grafted MCM-48 and Silica Xerogel as Superior Sorbents for Acidic Gas Removal from Natural Gas, *Ind. Eng. Chem. Res.* **2003,** *42*, 2427-2433.

[71] Son, W. J.; Choi, J. S.; Ahn, W. S. Adsorptive Removal of Carbon dioxide using Polyethylenimine-Loaded Mesoporous Materials, *Micropor. Mesopor. Mater.* **2008,** *113*, 31-40.

[72] Gil, M.; Tiscornia, I.; de la Iglesia, O.; Mallada, R.; Santamaría, J. Monoamine-grafted MCM-48: An efficient material for CO_2 removal at low partial pressures, *Chem. Eng. J.* **2011,** *175*, 291-297.

[73] Ma, X.; Wang, X.; Song, C. "Molecular Basket" Sorbent for Separation of CO_2 and H_2S from Various Gas Streams, *J. Am. Chem. Soc.* **2009,** *131*, 5777-5783.

[74] Knowles, G. P.; Graham, J. V.; Delaney, S. W.; Chaffee, A. L. Aminopropyl Functionalized Mesoporous Silica as CO_2 Adsorbents, *Fuel Process. Technol.* **2005,** *86*, 1435-1448.

[75] Knofel, C.; Descarpenteries, J.; Benzaouia, A.; Zelenak, V.; Mornet, S.; Llewellyn, P.L.; Hornebecq, V. Functionalized Micro-/Mesoporous Silica for the Adsorption of Carbon dioxide, *Micropor. Mesopor. Mater.* **2007,** *99*, 79-85.

[76] Zelenak, V.; Badanicova, M.; Halamova, D.; Cejka, J.; Zukal, A.; Murafa, N.; Goerigk, G. Amine-Modified Ordered Mesoporous Silica: Effect of Pore Size on Carbon dioxide Capture, *Chem. Eng. J.* **2008,** *144*, 336-342.

[77] Hiyoshi, N.; Yogo, K.; Yashima, T. Adsorption Characteristics of Carbon dioxide on Organically Functionalized SBA-15, *Micropor. Mesopor. Mater.* **2005,** *84*, 357-365.

[78] Park, D. H.; Nishiyama, N.; Egashira,Y.; Ueyama, K. Separation of organic/water mixtures with silylated MCM-48 silica membranes, *Micropor. Mesopor. Mater.* **2003,** 66, 69-76.

[79] Sakamoto, Y.; Nagata, K.; Yogo, K.; Yamada, K. Preparation and CO_2 separation properties of amine-modified mesoporous silica membranes, *Micropor. Mesopor. Mater.* **2007,** *101*, 303-311.

[80] Kumar, P.; Kim, S.; Ida, J.; Guliants, V. V. Polyethyleneimine-Modified MCM-48 Membranes: Effect of Water Vapor and Feed Concentration on N_2/CO_2 Selectivity, *Ind. Eng. Chem. Res.* **2008,** *47*, 201-208.

[81] McCool, B. A.; Hill, N.; DiCarlo, J.; DeSisto, W. J. Synthesis and characterization of mesoporous silica membranes via dip-coating and hydrothermal deposition techniques, *J. Membr. Sci.* **2003,** *218*, 55-67.

[82] Kumar, P.; Ida, J.; Kim, S.; Guliants, V. V.; Lin, J. Y. S. Ordered mesoporous membranes: Effects of support and surfactant removal conditions on membrane quality, *J. Membr. Sci.* **2006,** *279*, 539-547.

[83] Kumar, P.; Ida, J.; Guliants, V.V. High flux mesoporous MCM-48 membranes: Effects of support and synthesis conditions on membrane permeance and quality, *Micropor. Mesopor. Mater.* **2008,** *110*, 595-599.

[84] Nishiyama, N.; Park, D.H.; Koide, A.; Egashira, Y.; Ueyama, K., A mesoporous silica (MCM-48) membrane: preparation and characterization, *J. Membr. Sci.* **2001,** *182*, 235-244.

[85] Nishiyama, N.; Koide, A.; Egashira, Y.; Ueyama, K. Mesoporous MCM-48 membrane synthesized on a porous stainless steel support, *Chem. Commun.* **1998,** *19*, 2147-2148.

[86] Liu, C.; Wang, L.; Ren, W.; Rong, Z.; Wang, X.; Wang, J. Synthesis and characterization of a mesoporous silica (MCM-48) membrane on a large-pore α-Al_2O_3 ceramic tube, *Micropor. Mesopor. Mater.* **2007,** *106*, 35-39.

[87] Ji, H.; Fan, Y.; Jin, W.; Chen, C.; Xu, N. Synthesis of Si-MCM-48 membrane by solvent extraction of the surfactant template, *J. Non-Cryst. Solids.* **2008,** *354*, 2010-2016.

[88] Chowdhury, S. R.; Schmuhl, R.; Keizer, K.; Elshof, J. E.; Blank, D. H. A. Pore size and surface chemistry effects on the transport of hydrophobic and hydrophilic solvents through mesoporous γ-alumina and silica MCM-48, *J. Membr. Sci.* **2003,** *225,* 177-186.

[89] Schmuhl, R.; Chowdhury, S. R.; Elshof, J. E.; Berg, A. V. D.; Blank, D. H. A. Nanostructured Ion-Selective MCM-48 Membranes, *J. Sol–Gel Sci. Technol.* **2004,** *31*, 249-252.

[90] Nakagawa, K.; Matsuyama, H.; Maki, T.; Teramoto, M.; Kubota, N. Preparation of mesoporous silica membrane by solvent evaporation method for filtration application, *Sep. Purif. Technol.* **2005,** *44,* 145-151.

[91] Grosso, D.; Balkenede, A. R.; Albouy, P. A.; Ayral, A.; Amenitsch, H.; Babonneau, F. Two-Dimensional Hexagonal Mesoporous Silica Thin Films Prepared from Block Copolymers: Detailed Characterization and Formation Mechanism, *Chem Mater* **2001,** *13,* 1848-1856.

[92] Klotz, M.; Ayral, A.; Guizard, C.; Cot, I. Synthesis and characterization of silica membranes exhibiting an ordered mesoporosity. Control of the porous texture and effect on the membrane permeability, *Sep. Purif. Technol.* **2001,** *25,* 71-78.

[93] Liu, C.; Wang, J.; Li, B. Preparation and characterization of ordered mesoporous silica membrane, *J. Non-crystall. Solids.* **2005,** *351,* 409-412.

[94] Hua, Shi, J. L.; Wang, L.; Zhang, W. H. Preparation of mesoporous silica films on a glass slide: surfactant template removal by solvent extraction, *J. Non-Crystall. Solids.* **2001,** *292,* 177-183.

[95] Liu, C.; Wang, L.; Ren, W.; Rong, Z.; Wang, X.; Wang, J. Synthesis and characterization of a mesoporous silica (MCM-48) membrane on a large-pore α-Al_2O_3 ceramic tube, *Micropor. Mesopor. Mater.* **2007,** *106,* 35-39.

[96] Higgins, S.; Kennard, R.; Hill, N.; DiCarlo, J.; DeSisto, W. J. Preparation and characterization of non-ionic block co-polymer templated mesoporous silica membranes, *J. Membr. Sci.* **2006,** *279,* 669-674.

[97] Schmuhl, R.; Chowdhury, S. R.; Elshof, J. E.; Berg, A. V. D.; Blank, D. H. A.; Nanostructured Ion-Selective MCM-48 Membranes, *J. Sol–Gel Sci. Technol.* **2004,** *31,* 249-252.

[98] Chowdhury, S. R.; Peters, A. M.; Blank, D. H. A.; Elshof, J. E. Influence of porous substrate on mesopore structure and water permeability of surfactant templated mesoporous silica membranes, *J. Membr. Sci.* **2006,** *279,* 276-281.

[99] Boffa, V.; Elshof, J. E.; Blank, D. H. A. Preparation of templated mesoporous silica membranes on macroporous α-alumina supports via direct coating of thixotropic polymeric sols, *Micropor. Mesopor. Mater.* **2007,** *100,* 173-182.

[100] Kim, S. Modified ordered mesoporous silica membranes for CO_2/N_2 separation, Master of Science Thesis, *University of Cincinnati, Ohio*; **2003.**

[101] Xomeritakis, G.; Tsai, C. Y.; Brinker, C. J. Microporous sol–gel derived aminosilicate membrane for enhanced carbon dioxide separation, *Sep. Purif. Technol.* **2005,** *42,* 249-257.

Chapter 2

CO_2 CAPTURE BY AMINE MODIFIED ORDERED MESOPOROUS SILICA MATERIALS & MEMBRANES: THEORY, REACTIONS AND TRANSPORT MECHANISMS

In this chapter, several topics are discussed to provide important background information for this research project. First, some theory related to adsorption, Henry's constant and isotherm modelings are discussed. The basic principles of the sol-gel technology are explained. Different synthesis routes of ordered mesoporous silica materials as well as membranes are discussed. Various reaction mechanisms between CO_2 *and amines for the functionalized ordered mesoporous silica are discussed. At the end of the chapter, different theory related to membrane separation and different types of transport mechanisms are explained.*

2.1. Introduction to Adsorption

The adsorption properties of a solid sorbent are governed by the nature and strength of force fields and their distribution along the active surface and pores. These interactions depend on the structure, framework composition, crystal size, and purity of the sorbent. Depending on the attractive forces between adsorbate and adsorbent, adsorption can be divided into two types namely physical adsorption and chemical adsorption. There are two main forces responsible for physical adsorption such as (i) electrostatic forces (e.g., polarization forces, surface field-molecular dipole and surface field gradient-molecular quadrupole interactions), and (ii) van der Waals or nonspecific forces, directly correlated with the sorbate molecular polarizability. In chemisorption, the covalent bond is formed between the surface of the solid adsorbent and target molecules. This covalent bond gives scope for much larger increases in adsorption capacity. Development of functionalized adsorbents aims to improve selectivity towards target molecules over other molecules by introducing or functionalizing the active sites of the adsorbent pores by a chemical group which has high affinity to target molecules.

2.2. Phase Rule for Adsorption

In general, phase equilibrium indicates equality of thermal, mechanical and chemical potentials. Adsorption is a surface phenomenon, and due to additional intensive variable, adsorption has one extra degree of freedom compared to that of bulk phase equilibria. The phase rule for adsorption is thus [**1**],

$$F = C - R + 3 \tag{2.1}$$

Where- F = number of degrees of freedom

C = number of chemical species and

R = number of phases

2.3. Equilibrium Adsorption Isotherm

Due to additional degrees of freedom, the equilibrium amount adsorbed for a pure gas on an adsorbent is a function of two variables (pressure and temperature).

$$A = \phi\{P, T\} \tag{2.2}$$

where, A is the amount adsorbed, P is the pressure and T is the temperature.

At constant temperature, the adsorbed amount is

$$A = \phi\{P\} \tag{2.3}$$

and this relationship is commonly called as an adsorption isotherm. Fugacity (*f*) is used instead of pressure to account for non-ideality in the gas phase at high pressures [**2**] and then isotherm relationship becomes.

$$A = \phi\{f\} \tag{2.4}$$

IUPAC has classified the adsorption isotherms into different types (Figure 2.1) [**3**]. Type I represent the adsorption characteristics of microporous adsorbent in which the molecular diameter of the adsorbate matches exactly with the pore diameter of the adsorbent. These types of isotherms have a definite saturation limit corresponding to the complete filling of the micropores. Non-porous or macroporous adsorbents show types II, III and VI isotherms whereas mesoporous adsorbents exhibit types IV and V isotherms. Shape of isotherms itself indicate that there are stronger gas-solid interactions for type II and IV and weaker one for type III and V. Shape of type VI suggests the multilayer formation either on a plane surface or on the walls of pores which are much larger than the molecular diameter of the adsorbate molecule.

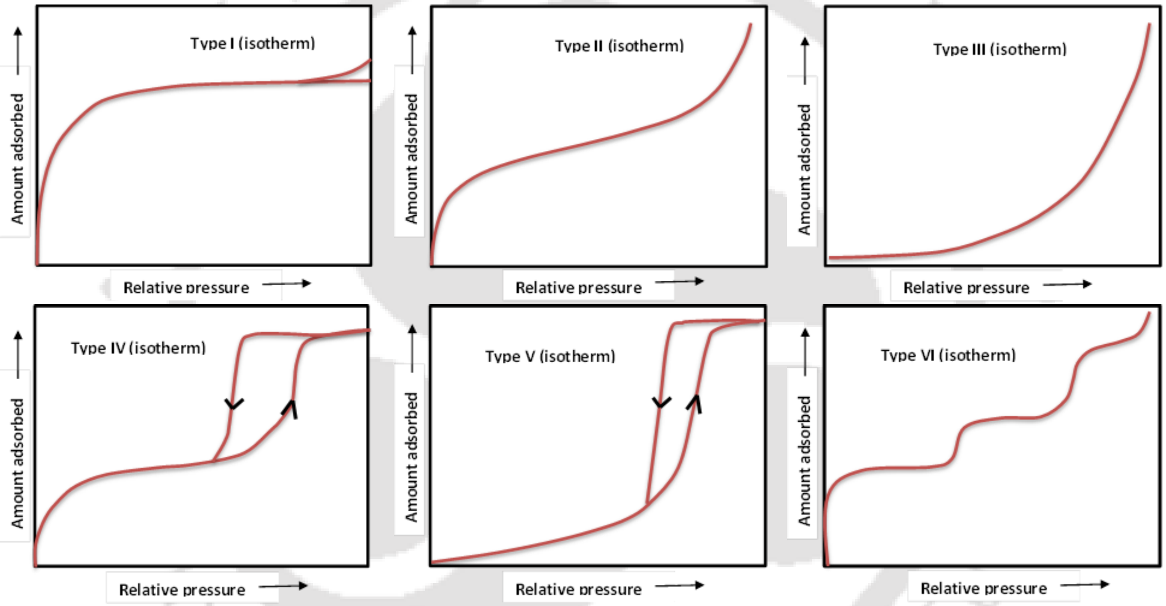

Figure 2.1 IUPAC classifications of adsorption isotherms [**3**].

2.4. Henry's Constant

The linear relationship between fluid phase and adsorbed concentrations is known as Henry's law and Henry's constant is defined as the slope of the isotherm at the limit of zero pressure.

Mathematically, Henry's constant, β, is written as Eq. 2.5.

$$\beta = \left(\frac{A}{P}\right)_{P \to 0} \tag{2.5}$$

Henry’s constant (β) is a measure of vertical interactions between adsorbate and adsorbent.

2.5. Models for Pure Gas Isotherms

In the following section, various adsorption isotherm models used in this work are presented.

2.5.1. Langmuir isotherm

The Langmuir model is based on the following assumptions:

(i) The number of adsorption sites is fixed.

(ii) Only one molecule can be held by each site.

(iii) All the adsorption sites are equally energetic.

(iv) There are no lateral interactions between adsorbate–adsorbate molecules.

Based on the above assumption Langmuir equation is formulated as

$$A = \frac{A^{\max} \beta f}{A^{\max} + \beta f} \tag{2.6}$$

where, A (mmol g^{-1}) is the amount adsorbed, f (bar) is the fugacity, A^{max} (mmol g^{-1}) is the saturation capacity, β (mmol g^{-1} bar^{-1}) is Henry’s constant. Saturation capacity is considered to be independent of temperature; and the temperature dependency for Henry's constant is expressed by

$$\beta = \beta^{(0)} \exp\left(\beta^{(1)}/T\right) \tag{2.7}$$

where, T is temperature in K. The two parameters $\beta^{(0)}$ and $\beta^{(1)}$ are related to entropy and enthalpy of adsorption at zero loading, respectively.

2.5.2. Dual Site Langmuir (DSL) isotherm

The Dual Site Langmuir (DSL) model determines the existence of two types of adsorption sites of different energetic. Each site follows a Langmuir adsorption behavior. A DSL isotherm model is given by [**4**]

$$A = \frac{A_1^{\max}\beta_1 f}{1+\beta_1 f} + \frac{A_2^{\max}\beta_2 f}{1+\beta_2 f} \tag{2.8}$$

where, A_1^{max} and A_2^{max} (mmol g^{-1}) are the saturation capacities of sites 1 and 2, respectively; β_1 and β_2 (bar^{-1}) are the affinity parameters for sites 1 and 2, respectively. Saturation capacities (A_1^{max} and A_2^{max}) are considered to be independent of temperature and the usual temperature dependency was considered for the affinity parameters (Eq. 2.9).

$$\beta_1 = \beta_1^{(0)} \exp\left(\beta_1^{(1)}/T\right); \quad \beta_2 = \beta_2^{(0)} \exp\left(\beta_2^{(1)}/T\right) \tag{2.9}$$

Henry's constant (β) in this model can be calculated as

$$\beta = A_1^{\max}\beta_1 + A_2^{\max}\beta_2 \tag{2.10}$$

2.5.3. Virial isotherm

A virial isotherm is versatile as it can accommodate the heterogeneity in adsorption. Simple virial isotherm with three parameters is expressed as follows [**4**]:

$$\ln\left(\frac{f}{A}\right) = bA + cA^2 - \ln(\beta) \tag{2.11}$$

where, *b* and *c* are second and third virial coefficients for adsorption. The temperature dependency for these parameters is

$$b = b^{(0)} + b^{(1)}/T \ ; \qquad c = c^{(0)} + c^{(1)}/T \tag{2.12}$$

The temperature dependency for β is same as that in Eq. 2.7.

Since the equation is open ended, this isotherm has no limit on the amount adsorbed as the pressure (fugacity) increases. Thus extrapolation of the virial equation beyond the experimental measurements is not suggested. However, within the experimental range of temperature and pressure data, the virial equation is flexible and is also thermodynamically consistent.

In general, an adsorption isotherm is plotted in *A* vs *f* domain. However, for an experimental data analysis perspective, isotherm in a virial domain [*ln(P/A)* vs *A*] can be extremely useful. The intercept [-*ln(β)*] of the virial domain plot can directly be used to obtain Henry's constant (*β*). In addition, the slope of the virial domain plot reflects the energetics of adsorption. Any step or inflection in the virial domain plot indicates the heterogeneity in the adsorbent. This type of information is not easily recognizable from isotherm plotted in conventional domain.

2.5.4. Langmuir-virial isotherm

The Langmuir equation is derived for only energetic homogeneous surface which is generally not possible in a realistic situation. On the other hand, the flexible virial equation is versatile and can describe adsorption on a variety of surfaces. However, this equation does not account for the saturation at high pressure, a phenomena usually observed for most of the cases. Thus, Langmuir and virial models are combined in a Langmuir-virial model [**4**] (Eq. 2.13) to overcome the limitations in either case.

$$\ln\left(\frac{f}{A}\right) = bA + cA^2 + \ln\left(\frac{A^{\max}}{\beta(A^{\max} - A)}\right) \qquad (2.13)$$

This model correctly captures a saturation uptake of A^{max} at high pressure. The temperature dependency for Henry's constant and virial parameters *b*, *c* are given by Eq. 2.7 and Eq. 2.12.

2.6. Theoretical Background for Ordered Mesoporous Silica Synthesis

Huo et al. [**5**] described the formation of a number of materials using the concept of charge matching between the template and inorganic species. Figure 2.2 shows a schematic representation of an organic-inorganic interface under various synthesis conditions. Here, S denotes the surfactant template, I denotes the inorganic species, X represents the halogen ion. The positive (+), negative (-) and the neutral (0) symbols indicate cations, anions and neutral molecules respectively. Based on the pH used, the inorganic species can carry a different charge. For example, for the case where the pH of the synthesis solution is greater than 10, the silica will be in its anionic form which is shown in Figure 2.3. Conversely, for a pH lower than the isoelectric point, at 2, the silicate will be in its cationic form. In the most elementary system, as in the case for the synthesis of order silica at pH >10, the ordering is derived from the direct interaction between the inorganic species and charged surfactant (S^+I^-). In other cases, mediating ions might be necessary to bring about a charge matching within the system. This is obtained by the addition of acid or alkaline moieties. In synthesis conditions below a pH of 2, a halide (Br^-, Cl^-) acts as bridging ion to form a $S^+X^-I^+$ assembly.

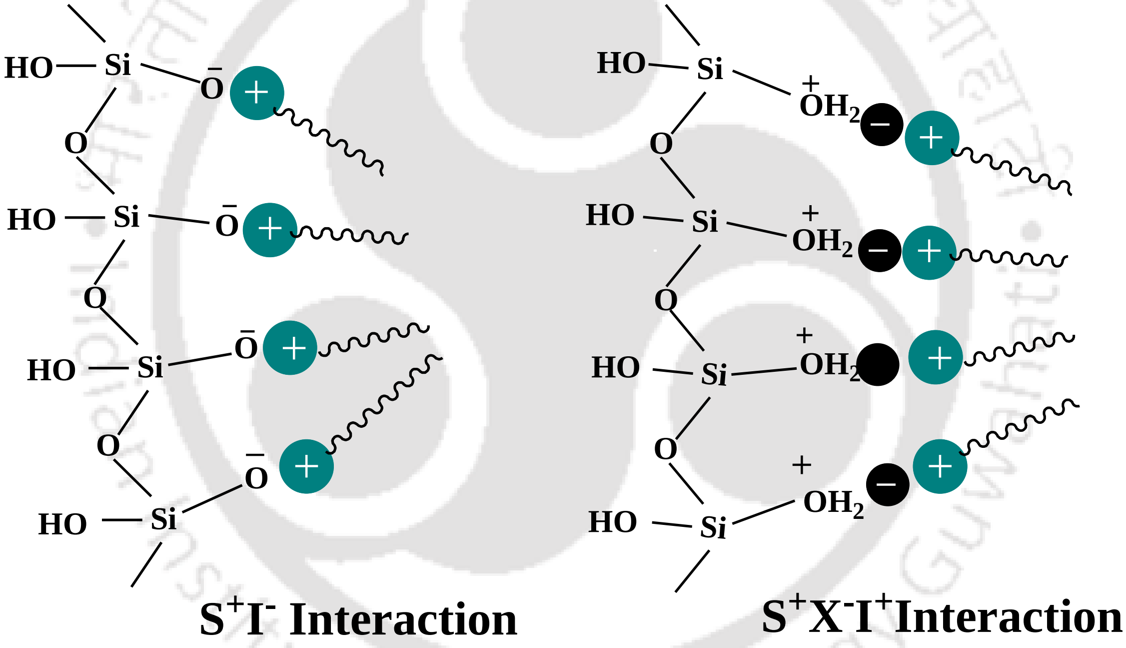

Figure 2.2 Different types of surfactant silica interactions [**6**]

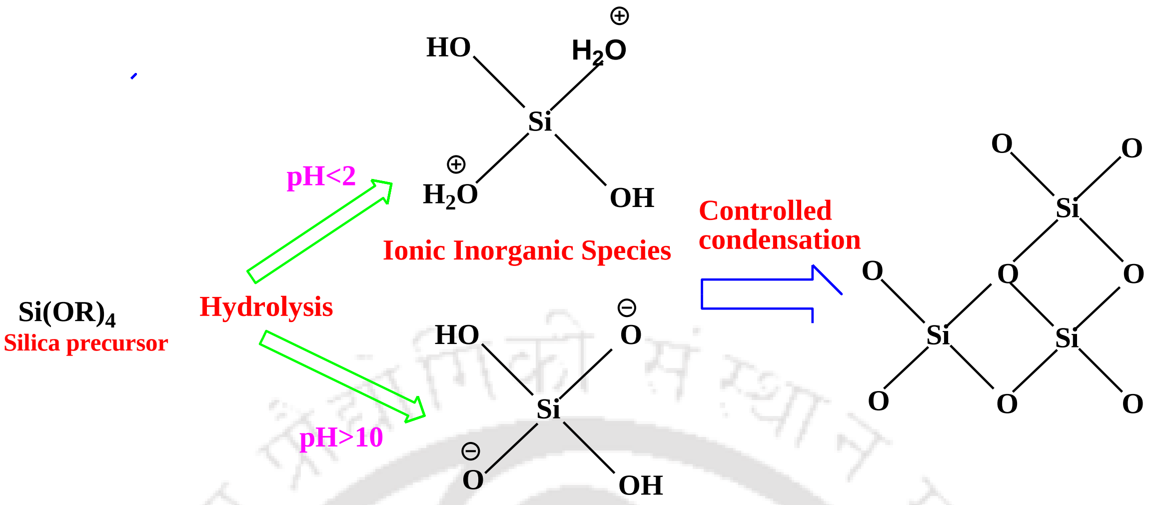

Figure 2.3 Silica precursor at variable pH condition [**6**]

2.6.1. Synthesis mechanism of mesoporous silica by basic route

In the first step of S^+I^- route, the formation of surfactant self-assembly occurs via liquid crystal template mechanism to form a homogeneous surfactant solution in common solvent media (usually aqueous). Then silicate precursor (I^-), such as tetraethyl or tetra methyl orthosilicate (TEOS or TMOS) or inorganic sodium silicate is added to the surfactant solution when it gets hydrolysed under basic condition (pH>10) to form a silicate oligomer sol. Next, inorganic-organic hybrid formation occurs by the aggregation and condensation of oligomers with surfactant micelle via cooperative assembly. And finally precipitates in the form of a gel. For further condensation, solidification and reorganization of the material to an ordered arrangement, hydrothermal treatment is applied to the gel [**7-8**]. Finally, after a certain time the resultant product is cooled, filtered, washed and dried. The surfactant of the as-synthesized solid is removed through calcination or solvent extraction. After removing the surfactant, the final ordered meso structured silica material is obtained [**9-10**]. M41S silica materials were first synthesized in alkaline condition [**11**]. This is the most well-known, old and convenient method of silica synthesis. Commonly, CTAB and SDS (sodium dodecyl sulphate) are used as surfactants [**12**], and sodium hydroxide (NaOH), potassium hydroxide (KOH), and ammonia solution ($NH_3.H_2O$) are used as base.

2.6.2. Synthesis mechanism of mesoporous silica by an acidic route

The silica-CTAB self-assembly process under acidic conditions was described as a $S^+X^-I^+$ process. This $S^+X^-I^+$ pathway is mediated by counter ions of opposite charge to that of the surfactant head group. It uses the long quaternary ammonium surfactant as a structure directing agent in acid condition, where $S^+ = C_nH_{3n+1}\ N^+(CH_3)_3$, n = 8-18; $X^- = Cl^-$, Br^- ,SO_4^{2-} , NO_3^- , etc., I^+ is a cationic silicate species. Huo et al. proposed [**13**] that in $S^+X^-I^+$ route, the acid anion X^- plays a crucial role. It serves as a buffer in the repulsion between the I^+ and S^+ by means of weak hydrogen bonding forces. Due to its weaker surfactant-silicate interaction in $S^+X^-I^+$, the association of S^+X^- determines the structure and morphology of mesoporous materials. It is noted that, the acidic system has the pH value lower than 2, the soluble silicate species promote acidic ionization, because their isoelectric point (IEP) is larger than 2 [**14-15**]. Thus the mesoporous materials framework is considered as formation via the $S^+X^-I^+$ self-assembly route in acidic media [**5**]. It is believed that acidic condensation of silica is slower than basic. Hydrochloric acid (HCl), nitric acid (HNO_3), sulphuric acid (H_2SO_4) sometimes weak acids like phosphoric acid (H_3PO_4), acetic acid (CH_3COOH) etc. are also used as a catalyst for silica synthesis under this condition.

2.6.3. Different techniques to synthesize ordered mesoporous silica membrane

The most common methods to prepare membranes from a synthesis solution or precursor sol are growth from solution method, the synthesis solution is brought to contact with a second phase. The second phase could be solid support where the membrane is deposited. Generally solid support submerged in the synthesis solution is subjected to hydrothermal synthesis at the required temperature and time to allow the formation of membrane at the solid support interface [**16-17**].

In the solvent evaporation method, a liquid film containing silica precursor, solvent and surfactant is formed on a substrate followed by evaporation of the solvent [**18**]. The solvent evaporation method for ordered mesoporous silica membranes is conducted by three different routes which are spin-coating [**19**], dip-coating [**20**] and slip-casting [**21**].

2.6.4. Mesoporous silica membrane formation by EISA mechanism

The formation mechanism of membrane of mesoporous silica on to α-alumina support is by Evaporation Induced Self Assembly (EISA) mechanism. This is the most common method for synthesizing mesoporous silica films, and it is used for e.g. spin or dip coating. In EISA, the start solvent consists of a silica precursor (TEOS) and surfactants (CTAB) dissolved in a water/ethanol solution. The surfactant concentration is here below CMC. By varying the initial composition of the surfactant containing solution, it is possible to vary the structure of the final film. The solution is spin coated onto the support, such as α-alumina in our case. After deposition of the solution onto the support, the ethanol evaporates and the concentration of water and surfactants increase. Hence, the surfactant concentration increases above CMC and micelles start to form on the support

[**22-24**]. The process is illustrated in Figure. 2.4. All the major reaction steps involved in the formation of mesoporous silica membranes are as follows.

Hydrolysis:	$Si(OR)_4 + nH_2O \rightarrow Si(OR)_{4-n}(OH)_n + nROH$
Condensation:	$(OR)_3SiOH + HOSi(OR)_3 \rightarrow (OR)_3Si\text{-}O\text{-}Si(OR)_3 + H_2O$ or
	$(OR)_3SiOR + HOSi(OR)_3 \rightarrow (OR)_3Si\text{-}O\text{-}Si(OR)_3 + ROH$
Gelation:	Formation of a spanning cluster across the vessel, giving a network with high viscosity, which entraps the remaining solution.
Aging:	A range of processes, including the formation of further cross-links, associated shrinkage of the gel as covalent links replace non-bonded contacts, Ostwald ripening and structural evolution with changes in pore sizes and pore wall strengths.
Drying:	The loss of water, alcohol and other volatile components. This first happens via syneresis (expulsion of the liquid as the gel shrinks) and then via evaporation of liquid from within the pore structure with associated development of capillary stress, which frequently leads to cracking. It does also include supercritical drying, in which capillary stress is avoided by the use of supercritical fluids (eg.CO_2) in conditions where there are no liquid/vapour interfaces.
Densification:	Thermal treatment, leading to the collapse of the open structure and formation of a dense ceramic.

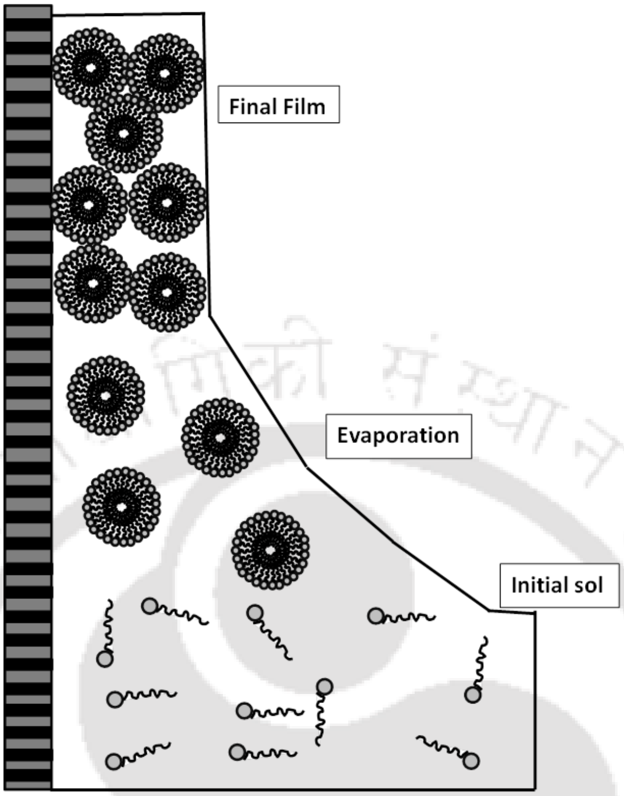

Figure 2.4 Evaporation induced self-assembly mechanism for film formation

2.7. Spin Coating Method

In spin coating method, a small amount of coating sol (silica) is poured on a flat smooth support (α-alumina) and then centrifugal force is applied on it to flow the liquid outward so that a thin film is formed on to the support. At the end of the process the excess liquid will flow outside the support and solvent evaporation will take place and a thin uniform film will be formed. By this process one can get a thin uniform film which may not get in the dip coating process. But in this process we need a flat and smooth surface of the support. By changing the spin speed and the amount of solvent used in sol, the thickness of the film can be varied.

The following are the steps involved in the spin-coating process which is also shown schematically in the Figure 2.5.

2.7.1. Steps involved in Spin Coating methods

Stage1: Excess of sol is deposited on the surface of support.

Stage 2: (Spin-up) the sol flows radially outward by centrifugal force.

Stage 3: (Spin-off) Excess of sol flows to the perimeter and leaves in a form of droplets.

Stage 4: Evaporation takes place leading to the formation of uniform thin film.

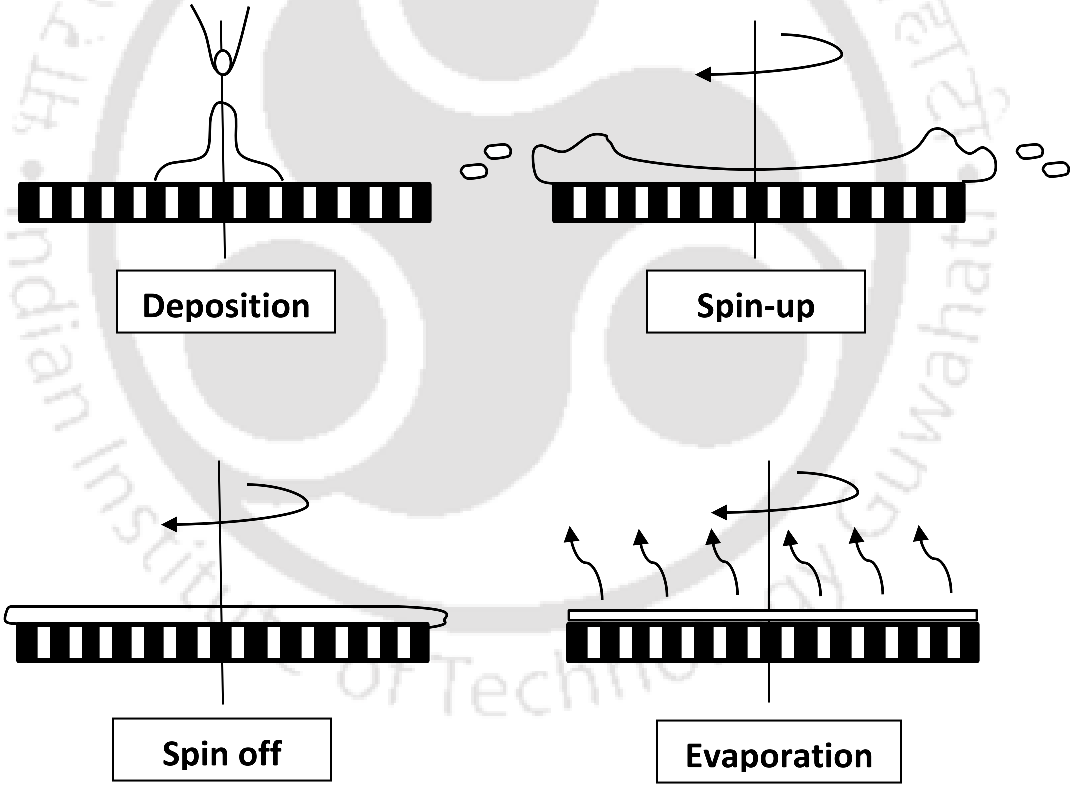

Figure 2.5 The steps involved in the spin-coating process

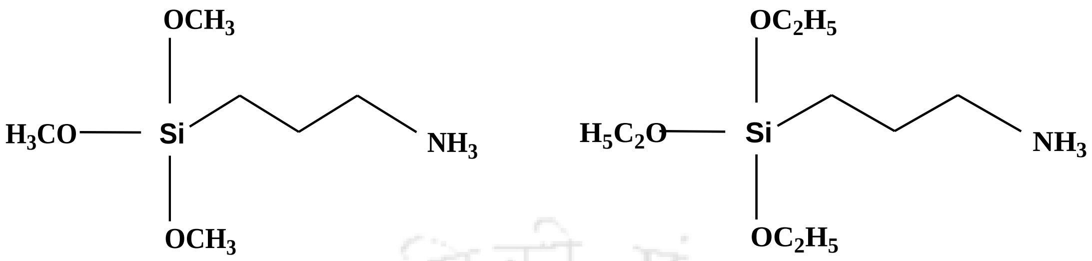

3-aminopropyltrimethoxysilane (3-APTMS) **3-aminopropyltriethoxysilane (3-APS)**

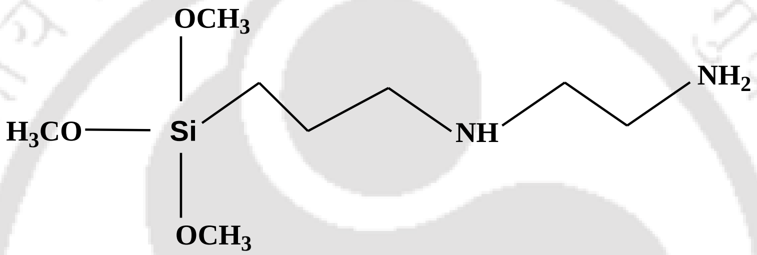

3-(2-aminoethylamino)propyl trimethoxysilane (3-2-Am)

Figure 2.6 Structural formulaes of some important aminosilanes

2.8. Gas Permeation through Amine Modified Silica Pore

Figure 2.6 represents structural formulaes of some amino-silane used in this work. The proposed mechanism by which CO_2 is transported using surface tethered amines is presented in Figure 2.7 & Figure 1.1 (see Chapter 1) [**25-26**]. CO_2 reacts with one amine group and forms a carbamate species (NHCOO−) in which two nitrogen atoms of amine are involved. The reaction mechanisms are as follows. These reactions are basically an acid-base reaction (Figure 2.7) where the CO_2 molecule is covalently bonded to the one of the amines, and the other amine is converted to an alkyl ammonium ion. Figure 1.1

(see Chapter 1) designates the schematic of a pore channel of the amine modified silica membrane. Amine groups are positioned closely due to the crosslinking when reacted with the CO_2 gas molecules. As a result, the effective pore size is significantly decreased and blocks the permeation of the unwanted gas of bigger molecular diameter. For an amine modified membrane, the CO_2 transfers between adjacent strands by the combination of thermally induced undulations of the amine strands with partial pressure driving force [**27**].

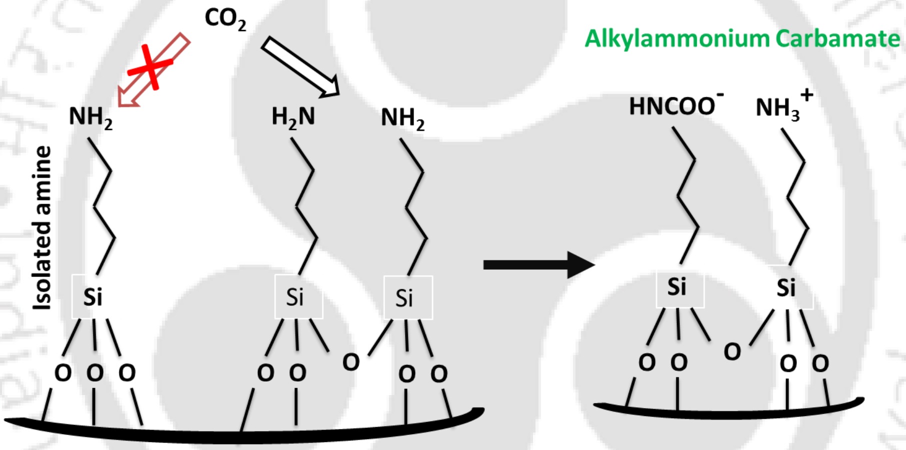

Figure 2.7 Mechanism of carbamate formation [**27**]

According to Kim et al, [**28**] during dry gas permeation, CO_2 adsorption to the amine modified silica membrane occurs on the amine pairs of primary-primary, primary-secondary, and secondary-secondary amines. The reactions are shown in Figure 2.8. It was observed that the reactions barely occur on the pairs of primary-tertiary and secondary-tertiary due to the steric hindrance.

As described above this is an acid-base reaction. Unlike primary and secondary amines, tertiary amine pairs are not involved in the CO_2 adsorption [**29**].

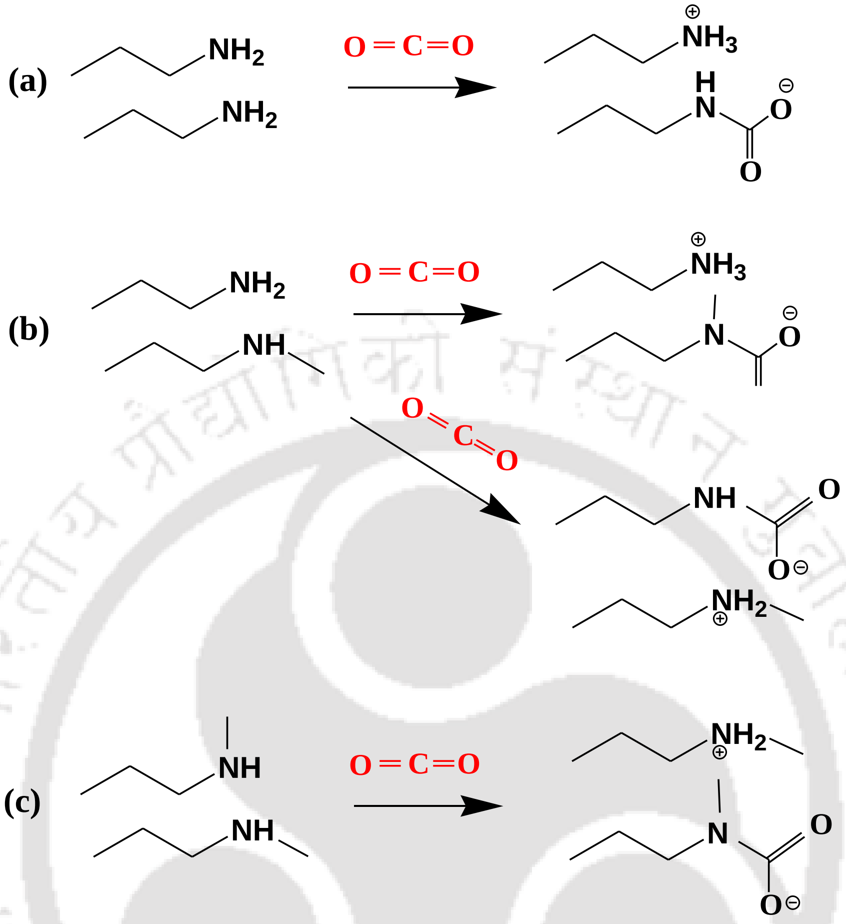

Figure 2.8 Mechanisms of CO_2 adsorption to the pairs of (a) primary-primary, (b) primary-secondary, and (c) secondary-secondary amines [**28**].

In the presence of water vapor, the CO_2 adsorption capacity of the amine modified silica membrane increases considerably, leading to higher CO_2 solubility [**30**]. Additionally, there is probably a slight contribution of adsorption by tertiary-tertiary amine pairs in the presence of water vapor [**29**]. In the presence of moisture, the nature of the chemical interactions between the amine modified silica membrane and CO_2 changes. The CO_2 hypothesized adsorption mechanism to the primary amine groups in the presence and absence of moisture are shown in Figure 2.9. The interaction between the basic surface and acidic CO_2 molecules is thought to result in the formation of surface ammonium carbamates under anhydrous conditions and in the formation of ammonium, bicarbonate and carbonate species in the presence of water. So in dry CO_2 permeation, adsorption capacities are limited to one mole of CO_2 for every two moles of surface-bound amine groups and in the presence of water, adsorption capacities may increase up to two moles of CO_2 per two moles of surface-bound amine groups. Due to each amine reacts with CO_2 molecule separately; the amine groups are less close to each other. This is an advantage over the dry condition for the CO_2 separation.

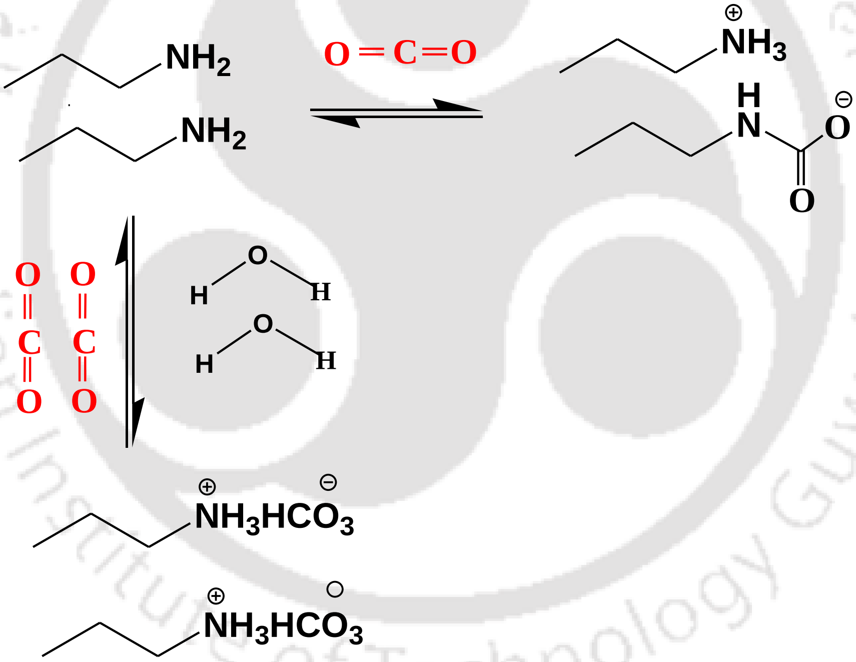

Figure 2.9 Surface reaction of tethered amine groups with CO_2 [**28**].

2.9. Fundamentals of Molecular Transport in Membranes

A good membrane should have both high selectivity and permeation of gases. The performance of a membrane can be determined by the terms permeance/permeability and separation factor/selectivity.

The permeance (P_A) of component A in a membrane is given by:

$$P_A \equiv \frac{\mathrm{N}_A}{A(\Delta P_A)} \tag{2.14}$$

where P_A is the permeance of the component A through the membrane, N_A is the moles of component A transferred per unit time, A is the membrane area, ΔP_A is the partial pressure difference of component A between the upstream and downstream side of the membrane.

The permeability (π_A) is given by:

$$\pi_A = P_A l \tag{2.15}$$

Where *l* is the thickness of the membrane.

The ideal selectivity of a membrane for the mixture A and B is hence the ratio of their permeabilities given by the equation:

$$\alpha_{A/B} = \frac{\pi_A}{\pi_B} = \frac{\left(\frac{y_A}{y_B}\right)}{\left(\frac{x_A}{x_B}\right)} \tag{2.16}$$

where x is the molar fractions of the corresponding gas component in the feed and y is the molar fractions of the corresponding gas component in the permeate.

2.10. Mass transport mechanisms

According to pore size, the porous inorganic membranes are usually subdivided into macro-porous (d_p > 50 nm), meso-porous (2 nm < d_p < 50 nm) and micro-porous (d_p < 2 nm) [**31**]. For sufficiently small pore sizes, the micro-porous membranes can be considered molecular sieves, since they "sieve out" large molecules from mixtures. However, most micro-porous membranes do not employ a pure sieving mechanism, but influence the motion of various species to a different extent. Figure 2.10 shows an outline of different mass transport mechanisms [**32**].

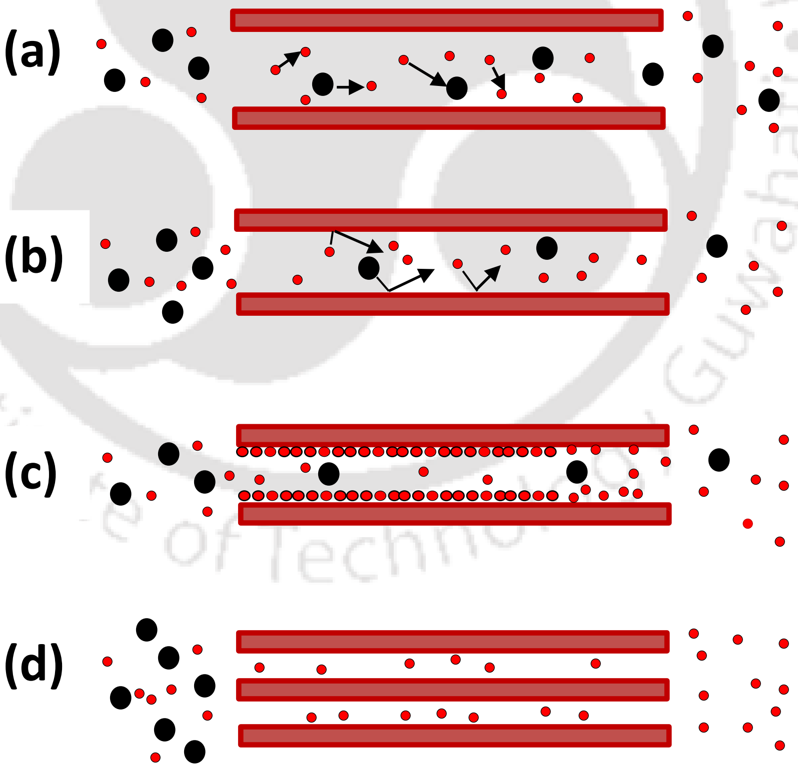

Figure 2.10 Mechanisms of mass transport through porous media: a) Viscous flow(Poiseuille); b) Knudsen diffusion; c) surface diffusion; d) molecular sieving

In macro- and meso-porous media the nature of the flow is determined by the comparative magnitude of the mean free path λ of molecules and the pore diameter d_p. The ratio of λ over d_p is referred to as the Knudsen number *Kn*

$$Kn=\lambda/d_p$$

2.10.1. Free molecule regime

When the ratio of the mean free path over the pore size is large ($\lambda >> d_\mathrm{p}$) collisions of molecules with the pore walls are predominant. In the time interval between intermolecular collisions many molecule-wall collisions occur and molecules are in thermal equilibrium with the wall. This transport regime is referred to as the free molecule regime, or Knudsen regime. The latter designation is connected with the well-known formula derived by Knudsen et al. [**33**], for the diffusive flow of molecules in a long tube in this regime

$$N_{Kn} = -D_{Kn}\left(\frac{\partial c}{\partial z}\right) \tag{2.17}$$

where the Knudsen diffusion coefficient $D_{Kn} = \frac{1}{3}\bar{v}\,d_p$ depends on the mean molecular speed $\bar{v}$ and the pore diameter d_p. An expression for the mean molecular speed can be obtained from the kinetic theory of gases $\bar{v} = \sqrt{\frac{8RT}{\pi M}}v$ [**34-35**], where *R* and *T* have their usual meaning and *M* is the molecular weight of the gaseous species [kg· mol^{-1}]. The Knudsen diffusion coefficient is similar to that for the self-diffusion of a gas, after replacing the mean free path with the pore diameter.

For free molecular transport in a porous medium the Knudsen expression has to be modified to account for the structure of the porous medium. This can be done by introducing a structure parameter K_0, after which the Knudsen diffusion coefficient becomes [**36**]

$$D_{Kn} = \frac{4}{3} K_o \bar{v} \tag{2.18}$$

For cylindrical pores the structure factor K_0 equals

$$K_o = \frac{1}{4}\frac{\varepsilon}{\tau} d_p \tag{2.19}$$

where ε is the dimensionless porosity and τ the dimensionless tortuousity.

Clearly, free molecular diffusion is a selective transport mechanism, since the flux is inversely proportional to the molecular mass of a species. This is due to the decrease in mean molecular velocity with increasing molecular weight. The decrease of the flux with increasing temperature is due to the fact that the concentration of an ideal gas (p/RT) decreases linearly with temperature, while the molecular velocity increases with the square root of temperature.

2.10.2. Viscous flow

When the mean free path is much smaller than the pore size ($\lambda << d_p$), information of intermolecular collisions is persistent. From the kinetic theory of gases an expression for the self-diffusion coefficient of a gas can be obtained, $D_{Kn} = \frac{1}{3} \bar{v}\, \lambda$. When a gradient in absolute pressure exists, momentum transport leads to drift velocities of the molecules. At low Reynold numbers, the non-selective viscous transport of a Newtonian fluid through a porous medium can be described by Darcy’s law, which for transport of an ideal gas in one dimension becomes

$$N = -\frac{B_0}{\eta}\frac{p}{RT}\left(\frac{\partial p}{\partial z}\right) \qquad (2.20)$$

Where B_0 is a structure parameter [m^2] and η the viscosity [Pa.s].

2.10.3. Gaseous diffusion

If the pore size is much larger than the mean free path and more than one type of species are present there is momentum transfer from the light (fast) molecules to the heavy (slow) ones, which gives rise to a non-selective non-viscous mass transport mechanism. This transport mechanism is referred to as gaseous diffusion.

2.10.4. Surface diffusion

For sufficiently low temperature and/or high pressure, adsorption of molecules onto the surface of the pore walls can occur. When the adsorbed molecules are mobile, surface diffusion can take place. The extent of surface diffusion is determined by the amount of molecules adsorbed and their mobility.

2.10.5. Molecular sieving

In molecular sieving the gas components are separated based on size exclusion (the size being the kinetic diameter of the gas molecules).

In order to function as a molecular sieve, membranes must have pore diameters that are in between those of the gas molecules to be separated. If the membrane has pore sizes between the diameter of the smaller and the larger gas molecules, then only the smaller molecule can permeate and a very high separation would be achieved. In practical situations, there will be a distribution of pore size in the membranes, and thus the gas permeability is actually influenced by a combination of transport mechanisms.

References

[1] Smith, J. M.; Van Ness, H. C. Introduction to Chemical Engineering Thermodynamics. *Fourth Edition, McGraw-Hill, New York,* **1987.**

[2] Talu, O. Needs, status, techniques and problems with binary gas adsorption experiments. *Adv. Colloid Interface Sci.* **1998,** *76-77*, 227-269.

[3] Barton, T. J.; Bull, L. M.; Klemperer, W. G.; Loy, D. A.; McEnaney, B.; Misono, M.; Monson, P. A.; Pez, G.; Scherer, G. W.; Vartuli, J. C.; Yaghi, O. M. Tailored Porous Materials. *Chem. Mater.* **1999,** *11*, 2633-2656.

[4] Chowdhury, P. Gas Adsorption on Cu-BTC and Cr-BDC Metal Organic Frameworks (MOFs). PhD Dissertation, *Indian Institute of Technology, Guwahati,* **2010.**

[5] Huo, Q.; Margolese, D. I.; Ciesla, U.; Feng, P.; Gier, T. E.; Sieger, P.; Leon, R.; Petroff, P. M.; Schuth, F.; Stucky, G. D. Generalized synthesis of periodic surfactant/inorganic composite materials, *Nature*, **1994,** *368*, 317-321.

[6] Pal, N.; Bhaumik, A. Soft templating strategies for the synthesis of mesoporous materials: Inorganic, organic–inorganic hybrid and purely organic solids, *Adv. Colloid Interface Sci.* **2013,** *189-190*, 21-41.

[7] Wan, Y.; Zhao, D. On the Controllable Soft-Templating Approach to Mesoporous Silicates, *Chem. Rev.* **2007,** *107*, 2821-2860.

[8] Berggren, A.; Palmqvist, A. E. C.; Holmberg, K. Surfactant-templated mesostructured materials from inorganic silica, *Soft. Matter.* **2005,** *1*, 219-226.

[9] Chandra, D.; Bhaumik, A. Highly active 2D hexagonal mesoporous titanium silicate synthesized using a cationic-anionic mixed surfactant assembly, *Ind. Eng. Chem. Res.* **2006,** *45,* 4879-4883.

[10] Vivero-Escoto, J. L.; Chiang Y. D.; Wu, K. C-W.; Yamauchi, Y. Recent progress in mesoporous titania materials: adjusting morphology for innovative applications, *Sci Technol. Adv. Mater.* **2012,** *13,* 1-9.

[11] Kresge, C. T.; Leonowicz, M. E.; Roth, W. J.; Vartuli, J. C.; Beck, J. S. Ordered mesoporous molecular-sieves synthesized by a liquid-crystal template mechanism, *Nature.* **1992,** *359,* 710-712.

[12] Guidotti, M.; Gavrilova, E.; Galarneau, A.; Coq, B.; Psaroa, R.; Ravasio, N. Epoxidation of methyl oleate with hydrogen peroxide. The use of Ti-containing silica solids as efficient heterogeneous catalysts, *Green. Chem.* **2011,** *13,* 1806-1811.

[13] Huo, Q.; Margolese, D. I.; Ciesla, U.; Demuth, D. G.; Feng, P.; Gier, T. E.; Chmelka, B. F.; Schuth, F.; Stucky, G. D. Organization of Organic Molecules with Inorganic Molecular Species into Nanocomposite Biphase Arrays, *Chem. Mater.* **1994,** *6,* 1176-1191.

[14] Iler, R.K. The Chemistry of Silica, *Wiley, New York,* **1979,** pp. 489, 644, 651, 674.

[15] Yang, Y.; Zhang, J.; Yang, W.; Wu, J.; Chen, R. Adsorption properties for urokinase on local diatomite surface, *Appl. Surf. Sci.* **2003,** *206,* 20-28.

[16] de la Iglesia, O.; Pedernera, M.; Mallada, R.; Lin, Z.; Rocha, J.; Coronas, J. Synthesis and characterization of MCM-48 tubular membranes, *J. Membr. Sci.* **2006,** *280,* 867-875.

[17] McCool, B. A.; Hill, N.; Dicarlo, J.; DeSisto, W. J. Synthesis and characterization of mesoporous silica membranes via dip-coating and hydrothermal deposition techniques, *J. Mmbr. Sci.* **2003,** *218,* 55-67.

[18] Guliants, V. V.; Carreon, M. A.; Lin, Y. S. Ordered mesoporous and macroporous inorganic films and membranes, *J. Membr. Sci.* **2004,** *235,* 53-72.

[19] Gomez-Vega, J. M.; Iyoshi, M.; Kim, K. Y.; Hozumi, A.; Sugimura, H.; Takai, O. Spin coated mesoporous silica coatings for medical applications, *Thin Solid Films* **2001,** *615,* 398-399.

[20] Grosso, D.; Balkenende, A. R.; Albouy, P. A.; Babonneau, F. Structural analysis of hexagonal mesoporous silica films produced from triblock-copolymer structuring sol–gel, *Stud. Surf. Sci. Catal.* **2000,** *129,* 673-682.

[21] Miyata, H.; Noma, T.; Watanabe, M.; Kuroda, K. Preparation of mesoporous silica films with fully aligned large mesochannels using nonionic surfactants, *Chem. Mater.* **2002,** *14,* 766-772.

[22] Brinker, C. J.; Lu, Y.; Sellinger, A.; Fan, H. Evaporation-induced self-assembly: nanostructures made easy, *Adv. Mater.* **1999,** *11,* 579-585.

[23] Grosso, D.; Cagnol, F.; Soler-Illia, G.; Crepaldi, E.; Amenitsch, H.; Brunet-Bruneau, A.; Bourgeois, A.; Sanchez, C. Fundamentals of Mesostructuring Through Evaporation-Induced Self-Assembly, *Adv. Funct. Mater*. **2004,** *14,* 309-322.

[24] Chao, K.; Liu, P.; Huang, K. Thin films of mesoporous silica: characterization and applications, *Comptes. Rendus. Chimie*. **2005,** *8*, 727-739.

[25] Hiyoshi, N.; Yogo, K.; Yashima, T. Adsorption characteristics of carbon dioxide on organically functionalized SBA-15, *Micropor. Mesopor. Mater*. **2005,** *84(1–3)*, 357-365.

[26] Cussler, E. L.; Aris, R.; Bhown, A. On the limits of facilitated diffusion, *J. Membr. Sci.* **1989,** *43 (2–3)*, 149-164.

[27] Ostwal, M.; Pal Singh, R.; Dec, S. F.; Lusk, M. T.; Way, J. D. 3-Aminopropyltriethoxysilane functionalized inorganic membranes for high temperature CO_2/N_2 separation, *J. Membr. Sci*. **2011,** *369*, 139-147.

[28] Kim, H. J. Modified mesoporous silica membranes for separation applications, PhD Dissertation, *Georgia Institute of Technology, Georgia*, **2013.**

[29] Bollini, P.; Didas, S. A.; Jones, C. W. Amine-oxide hybrid materials for acid gas separations, *J. Mater. Chem.* **2011,** *21*, 15100-15120.

[30] Xu, X. C.; Song, C. S.; Miller, B. G.; Scaroni, A. W. Influence of moisture on CO_2 separation from gas mixture by a nanoporous adsorbent based on polyethylenimine-modified molecular sieve MCM-41, *Ind. Eng. Chem. Res.* **2005,** *44*, 8113-8119.

[31] Gregg S. J.; Sing, K. S. W. Adsorption, Surface Area and Porosity, *Academic Press, New York*, **1967.**

[32] Benes, N. E. Mass Transport in Thin Supported Silica Membranes, PhD Dissertation, *University of Twente,* **2000.**

[33] Knudsen M. Die Gesetze der Molekular strömung und der innern Reibunsströmung der Gase durch, *Ann. Phys.* **1909,** *28,* 75-130.

[34] Kennard E. H. Kinetic Theory of Gases, *McGraw-Hil Inc., New York,* **1938.**

[35] Furry, W.H. On the elementary Explanation of Diffusion Phenomena in Gases, *Am. J. Phys.* **1948,** *16,* 63-78.

[36] Mason E. A.; Malinauskas, A. P. Gas Transport in Porous Media: The Dusty Gas Model, *Elsevier, New York,* **1983.**

Chapter 3

CO_2 ADSORPTION CHARACTERISTICS FOR PURE & AMINE MODIFIED ORDERED MESOPOROUS SILICA POWDERS

This chapter elaborates detailed studies including the synthesis and characterization of ordered mesoporous silica (OMS) materials such as MCM-48. The amine-modified OMS powder is a good reference material for estimating membrane properties. Their surface characteristics for CO_2 adsorption and separation were performed and elaborated. The OMS materials were functionalized with three different amines. We investigated the effect of grafting of different amines on MCM-48 on its CO_2 adsorption characteristics. The CO_2 isotherms at 30 ^oC are measured up to 10 bar on different amine loaded MCM-48 samples to systematically evaluate the effect of amine on CO_2 adsorption capacity. While at low pressures up to 4 bar, amine loaded sample exhibit more CO_2 uptake, at a higher pressures pure MCM-48 showed better CO_2 loading. The effect of temperature is also examined to understand whether physisorption or chemisorption dominates for amine loaded samples. Modeling of CO_2 isotherms is also carried out to get molecular level insight and to calculate Henry's constants.

3.1. Introduction

For post combustion CO_2 capture, absorption of CO_2 into aqueous alkanolamine solutions is the most common technique. However, the scientific community is actively involved in search of alternate technologies due to the high energy requirement for the amine absorption process in addition to the corrosive nature of the solvents used for absorption. Adsorption is considered a promising technology for the removal of CO_2 from flue gas or other gaseous mixtures due to low regeneration cost, no corrosion and simplicity of this process. The main challenge for the development of sorbent is not only to possess the desired selectivity and sorption capacity toward the target gases but also facilitating control of the overall treatment process. A wide range of uniform pore size and the high density of silanol groups in mesoporous silica materials make them attractive for the introduction of functional groups with high coverage. For CO_2 capture related applications, amine functional groups are rigorously used chemical functionalities. Overall, it is well known that amine functional group on the mesoporous surface plays a critical role in CO_2 adsorption.

Amine functionalized mesoporous materials are found to have a good CO_2 adsorption capacity especially under sub-atmospheric pressures [**1-4**]. However, most of the surface functionalization studies on mesoporous materials are focused on MCM-41 silica, which has one-dimensional pore channel structure prone to diffusion limitations and pore blockage. In contrast, MCM-48 possesses the three-dimensional interconnected cubic pore structure and is considered as a better potential support than MCM-41 [**5**]. Few reports are available on CO_2 adsorption on amine modified MCM-48 [**5-8**]. Generally,

CO_2 interactions enhance with the increase in amino group density in the support material. However, the highest efficiency, defined as the mole of adsorbed CO_2 per mole of amino group, is known to be for monoamines [**9**]. The reported efficiency ranges from 0.09 to 0.89 for monoamine-functionalized mesoporous silica materials [**10-11**]. This huge variation in efficiency suggests that the functionalization process either has a low reproducibility or, more likely, varies strongly due to the difference for materials with different structures and pore sizes. In fact, the highest values for dry conditions and low partial pressures of CO_2 are reported to be ~0.5 for pore-expanded MCM-41, PE-MCM-41 [**11**], and three-dimensional pore structure MCM-48 [**5**].

In this work, the effect of grafting of different amines on MCM-48 on its CO_2 adsorption characteristics is investigated. CO_2 isotherms at 30 ^{o}C are measured up to 10 bar on different amine loaded MCM-48 samples to systematically evaluate the effect of amine on CO_2 adsorption. While at low pressure up to 4 bar, amine loaded sample exhibit more CO_2 uptake, at higher pressures, pure MCM-48 sample showed better CO_2 loading. The effect of temperature is also examined to understand whether physisorption or chemisorption dominates for amine loaded samples. Modeling of CO_2 isotherms is also carried out to get molecular level insight and to calculate Henry's constants.

3.2. Materials

Sodium hydroxide (NaOH) and anhydrous toluene (EMPARTA^{R} ACS) were purchased from MERCK, Germany. Tetraethyl orthosilicate (TEOS), N-hexadecyl trimethyl ammonium bromide (CTAB), 3-aminopropyltriethoxysilane (3-APS), 3-

aminopropyltrimethoxysilane (3-APTMS), and 3-(2-aminoethylamino) propyl trimethoxysilane (3-2-Am) were supplied by Sigma Aldrich, India.

3.3. Experimental

3.3.1. Synthesis

3.3.1.1. Synthesis of MCM-48 by basic route

A mixture of 110 ml of deionized water, 2 g of NaOH and 14.6 g cetyltrimethylammoniumbromide (CTAB) were taken in a beaker and stirred at 50 ^{o}C until the CTAB was completely dissolved [12]. Then this solution was cooled down to room temperature and 20 g of tetraethoxysilane (TEOS) was added to the solution followed by stirring for 30 min to make the silica sol. The silica sol was then transferred to a teflon vessel, and kept for 3 days at a temperature of 90 ^{o}C in an oven. The product was thoroughly washed with distilled water in a filter paper and then dried in an oven at 60 ^{o}C. Finally, MCM-48 powder was obtained by calcination at 550 ^{o}C with heating and cooling rate of 0.5 ^{o}C/min.

3.3.1.2. Synthesis of amine-grafted MCM-48

1 g of calcined MCM-48 materials obtained by a basic route was taken to a dry 250 mL 3 neck round bottomed flask. The MCM-48 powder was then kept at 150 °C for around 4 h to desorb any pre-adsorbed moisture or gases. 50 mL of anhydrous toluene was added to the mixture and was stirred for 10 min to enable the dispersion of MCM-48 material. Then the calculated amount (9, 10, 15 or 20 mmol) of different amino-silane viz. 3-aminopropyltriethoxysilane (3-APS), 3-aminopropyltrimethoxysilane (3-APTMS), and 3-

(2-aminoethylamino) propyl trimethoxysilane (3-2-Am) were added to the above mixture and stirred at ~140 °C under reflux for 24 h. Accordingly, samples are named as 3-APS-9, 3-APTMS-9, 3-2-Am-9, 3-APS-10 and so on, where 3-APS, 3-APTMS and 3-2-Am are the respective aminosilanes and the numeric value ‘9’, ‘10’, ‘15’ and ‘20’ stands for the amount of amino silane added to the MCM-48 sample. The obtained product was vacuum filtered and washed with anhydrous toluene to remove any physisorbed aminosilane from the sample. Finally, the amine-grafted MCM-48 powder was vacuum dried at 70 °C for 8 h and stored in a dry sample box.

3.3.2. Characterization techniques

Thermogravimetric analysis (TGA) was performed on Mettler Toledo thermogravimetric analyser (TGA/SDTA model 851). The measurements were carried out under a nitrogen atmosphere at a heating rate of 10 °C/min. Nitrogen physisorption measurements at 77 K were conducted on a Beckman Coulter surface area analyzer (Coulter SA model 3100). Samples were degassed at 110 °C for 4 h prior to N_2 adsorption – desorption measurements. The specific surface area was calculated from the BET (Brunauer−Emmett−Teller) model and pore size distribution was obtained through the BJH (Barrett−Joyner−Halenda) approach. The total pore volume was estimated at a relative pressure of 0.99, assuming that full surface saturation had been achieved with nitrogen. X-ray diffraction (XRD) patterns of MCM-48 samples were carried out under an air atmosphere at room temperature on a Bruker A8 advance instrument operating at 40 kV and 40 mA using Cu Kα (λ = 1.5406 Å) radiation. 2θ ranges between (1−10)° at a scanning rate of 0.02° s^{-1} and a step size of 0.5 s. FTIR spectrum analyses (SHIMADZU, IR Affinity 1, Japan) were also performed to resolve the organic chemical groups of bare and functionalized MCM-48 powder. FTIR spectra were recorded in the 4000 - 500 cm^{-1} wave number region using spectroscopic-quality KBr powder with 40 scans per sample and 4 cm^{-1} resolution.

3.3.3. CO_2 adsorption measurements

CO_2 isotherms were measured following Sieverts method at 30 ^oC. The Quantachrome-iSorb HP1 unit was used to perform all the measurements [**Appendix 1**]. Adsorbent samples were activated by heating them at 120 ^oC under vacuum. The dead volume of sample tube was obtained from helium measurement using non-adsorbing helium assumption.

3.4. Results and Discussions

3.4.1. Thermo-gravimetric analysis

Thermo-gravimetric analyses (TGA) of all the samples are shown in Figure 3.1. As expected, there is only one weight loss below 100 ^oC for MCM-48 sample due to removal of moisture. Above 100 ^oC, the TGA curve shows additional weight loss for pure MCM-48 sample, associated with condensation of surface silanol groups. Thereafter, the sample shows constant weight. In contrast, amine grafted samples exhibit one more weight loss corresponding to the decomposition of grafted amine. For all samples, removal of amine starts beyond 130 ^oC [8]. Thermal stability of samples also seems to be satisfactory in the context of flue gas application (as flue gas temperature typically ranges between 70-120 ^oC. The reduction in weight is more pronounced for the sample with higher amine loading (like 3-APS-20).

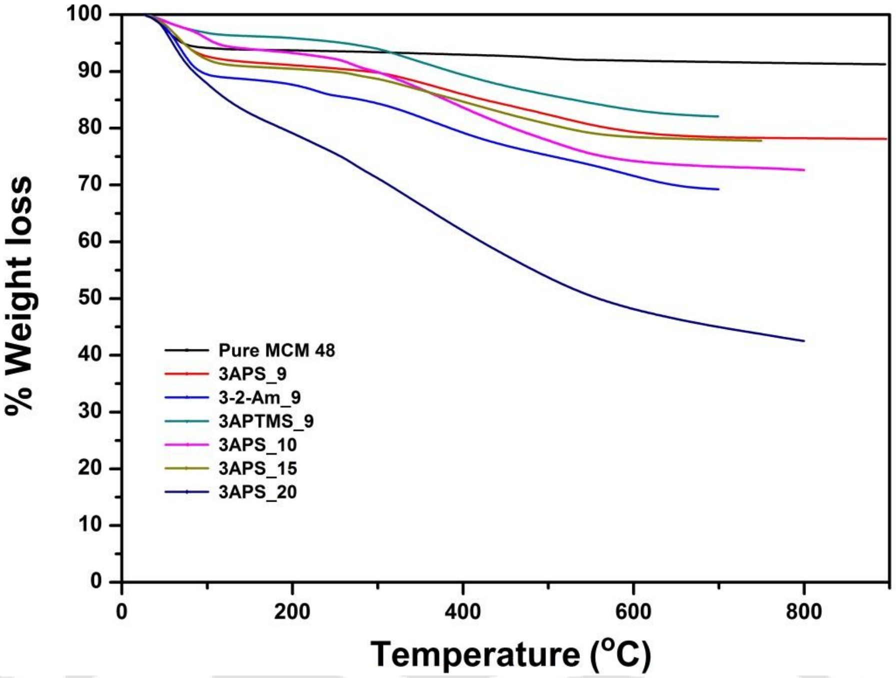

Figure 3.1 Thermogram of different MCM-48 based samples under the flow of N_2.

3.4.2. Surface area analysis

N_2 physisorption isotherms at 77 K (Figure 3.2) were measured for the calculation of surface area and pore volume. Pure MCM-48 material exhibits a typical type IV shape (characteristic of mesoporous material) for N_2 adsorption isotherm, while that of the amine grafted MCM-48 material is the type I microporous. BET surface area and pore volume of all the samples are given in Table 3.1. Surface area and pore volume of MCM-48 material obtained in this work are similar to that reported in the literature [**6-7**]. After the attachment of 9 mmol of 3-APS, 3-APTMS or 3-2-Am, surface area is reduced from 1133 m^2 g^{-1} to 263 – 300 m^2 g^{-1} range. The similar reduction in the surface area is also reported in the literature [**6-7**] after grafting with amine. For samples with higher 3-APS content (10, 15 and 20 mmol), the reduction in surface area and pore volume is drastic; this may be due to blocking of pores.

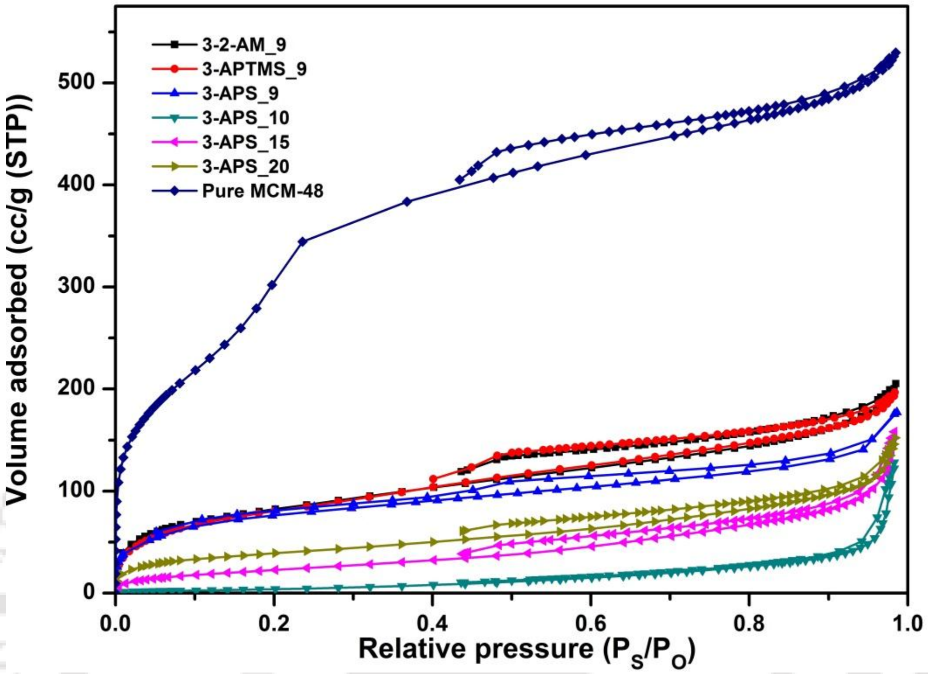

Figure 3.2 Adsorption isotherm of N_2 on MCM-48 based samples at 77 K.

Table 3.1 BET surface area and pore volume of the different MCM-48 samples.

Sample	BET surface area, m^2 g^{-1}	Pore volume, cm^3 g^{-1}
Pure MCM-48	1133.35	0.81
3-2-Am_9	299.21	0.31
3-APTMS_9	299.09	0.30
3-APS_9	263.82	0.27
3-APS_10	15.54	0.18
3-APS_15	86	0.23
3-APS_20	141.94	0.22

3.4.3. Fourier-transform infrared spectroscopy (FTIR) analysis

Figure 3.3 shows the FTIR spectra for pure calcined MCM-48 materials and different amine functionalized MCM-48 materials. It can be observed from the figure that a sharp absorption band at 3748 cm^{-1} and a broad absorption band at around 3500 cm^{-1} are present for pure MCM-48 materials. The absorption band at 3748 cm^{-1} corresponded to OH stretching of free silianol groups and 3500 cm^{-1} corresponded to hydrogen-bonded SiOH groups [**13**]. There are no bands for single SiOH groups in amine-modified MCM-48 materials. Since, all the single SiOH groups were reacted during the attachment of functional groups, and the bands were disappeared.

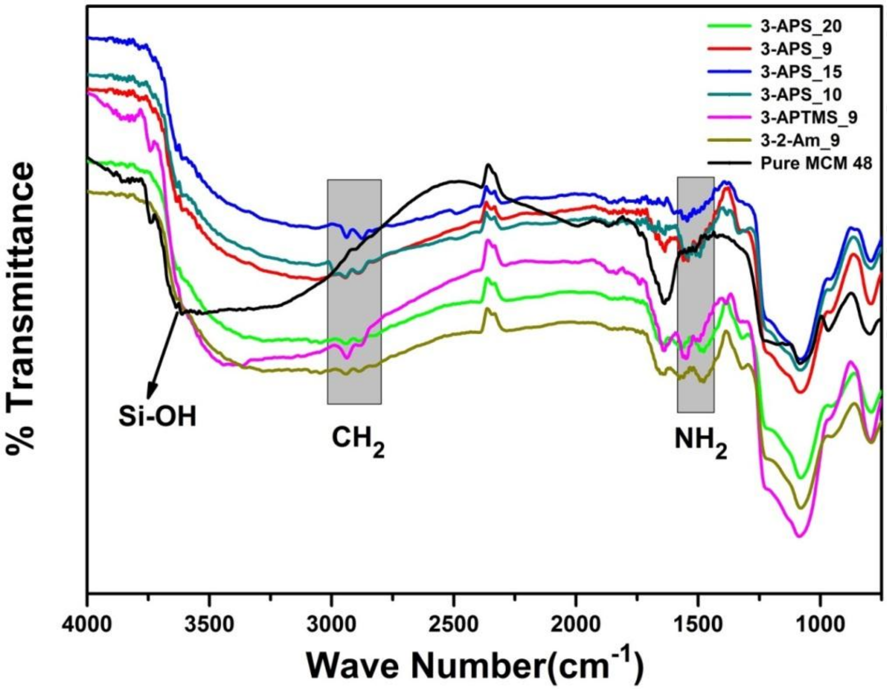

Figure 3.3 FTIR spectra on different MCM-48 based materials.

The band around 1590 cm^{-1} is attributed to the NH_2 scissoring vibration [**14-16**]. This band indicates that the MCM-48 materials were successfully functionalized by the amine groups. The bands at 2931-2835 cm^{-1} are due to CH stretching in propyl groups.

3.4.4. X-ray diffraction (XRD) analysis

Figure 3.4 shows the XRD pattern for pure MCM-48 materials. It can be observed that a dominant (211) peak with small (220), (420) and (322) reflections, are attributed to 3D-cubical (Ia3d) pore structure [**17**]. The structure of the MCM-48 before and after functionalization with different amines (3-aminopropyltriethoxysilane (3-APS), 3-aminopropyltrimethoxysilane (3-APTMS), and 3-(2-aminoethylamino) propyl trimethoxysilane (3-2-Am)) as well as the structure for different loading of 3-APS are ch-

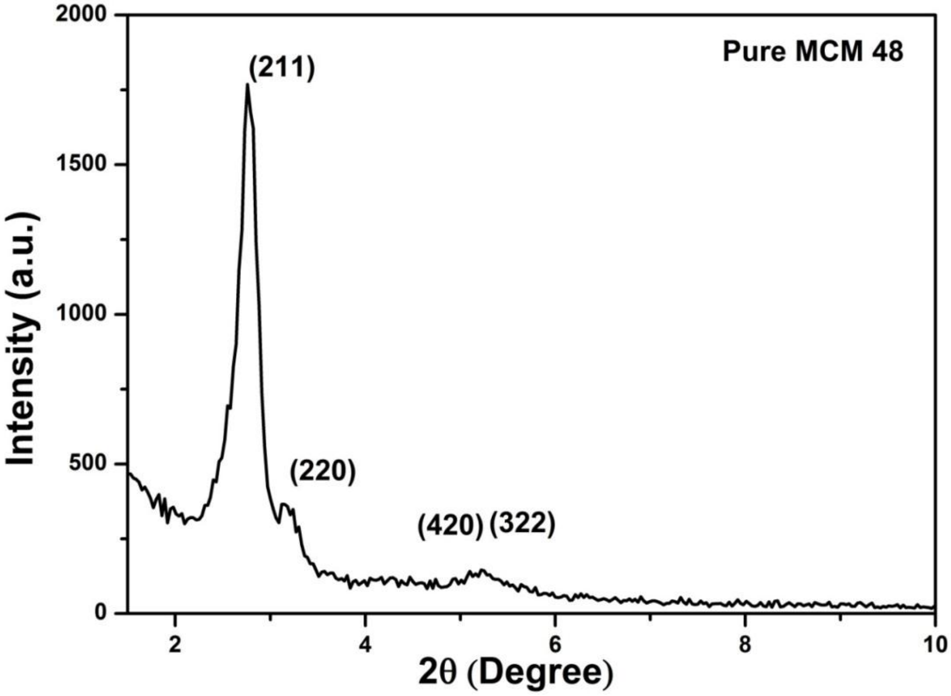

Figure 3.4 XRD pattern of pure MCM-48 sample.

-racterized and compared in Figure 3.5. A considerable decrease in peak intensity was observed in amine functionalized OMS (MCM-48) materials. This was possibly attributed due to the pore filling by the aminosilane. The reflections at higher indices almost disappeared. These changes in the pattern are due to partial loss of the space correlation of the pores.

Many literatures [**18-21**] observed this kind of resultant disorder after silylation of mesoporous silica materials.

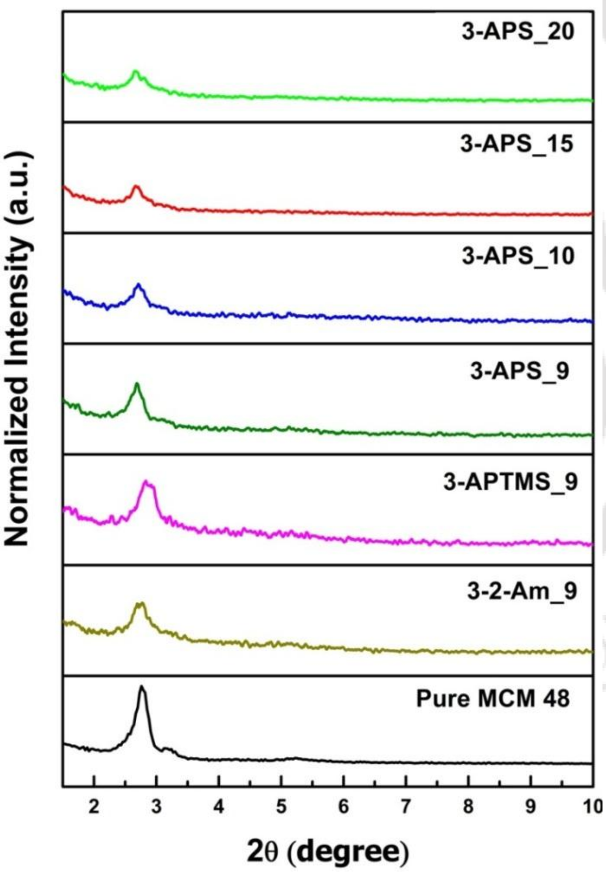

Figure 3.5 XRD pattern of pure and amine modified MCM-48 samples.

3.4.5. CO_2 adsorption analysis

CO_2 isotherms at 30 ^oC of different MCM-48 samples are shown in Figure 3.6. Flue gas streams come out at about ambient pressure with CO_2 concentration of 12 − 20% which means the CO_2 partial pressure in flue gas streams ranges from 0.12 to 0.20 bar. Thus, it is desirable to have a good CO_2 adsorption capacity in this pressure range for an adsorbent used for removal of CO_2 from the flue gas streams. CO_2 adsorption at 0.2 bar and 30 ^oC is increased significantly from ~0.1 mmol g^{-1} to ~0.84 mmol g^{-1} after grafting of 9 mmol of different on 1 g of MCM-48 material. CO_2 uptake 0.2 bar obtained for amine grafted MCM-48 samples is similar to that reported by some other research groups like Gil et al. [**8**], and is slightly higher than that reported by Kim et al. [**6**]. A detailed comparison between CO_2 uptake obtained in this work with that of other several reported adsorbents is presented in Table 3.2.

CO_2 loading on pure MCM-48 sample surpasses to that of other samples due to its higher surface area as saturation uptake is generally governed by surface area [**26**]. It should be noticed here that till 1.8 bar, isotherms of all amine grafted samples overlap to each other. This indicates that the degree of grafting is similar for all three considered 3-2 Am, 3-APTMS, 3-APS amines. The small difference between uptakes of different amine grafted samples can easily be attributed to the difference in their surface area. For further investigation, 3-APS amine is chosen. To demonstrate the effect of loading of different quantities of amine, CO_2 isotherms of 9 and 20 mmol 3-APS loaded samples at 30 ^oC are compared in the Figure 3.7. Interestingly, isotherms on both samples follow each other throughout the measurement range and there is no effect of putting more 3-APS amine than 9 mmol (for 1 gm of MCM-48) during grafting. These results suggest that all of the functional group of MCM-48 materials are getting occupied for 9 mmol loading of 3-APS amine itself and additional 3-APS molecules are not getting free functional groups in MCM-48 to get grafted while adding 20 mmol 3-APS. Isotherms of 3-APS_20 at different temperatures are compared in figure 3.8 (the numeric value 30 C, 60 C and 75 C stands for the corresponding temperatures in degree C) in order to understand the effect of temperature on adsorption characteristics of these samples. It can be observed that adsorption uptake decreases with the increase of temperature. This indicates that the interactions between CO_2 molecules and adsorbent samples are exothermic in nature. Similar behaviour is reported in the literature for amine grafted samples [**25**].

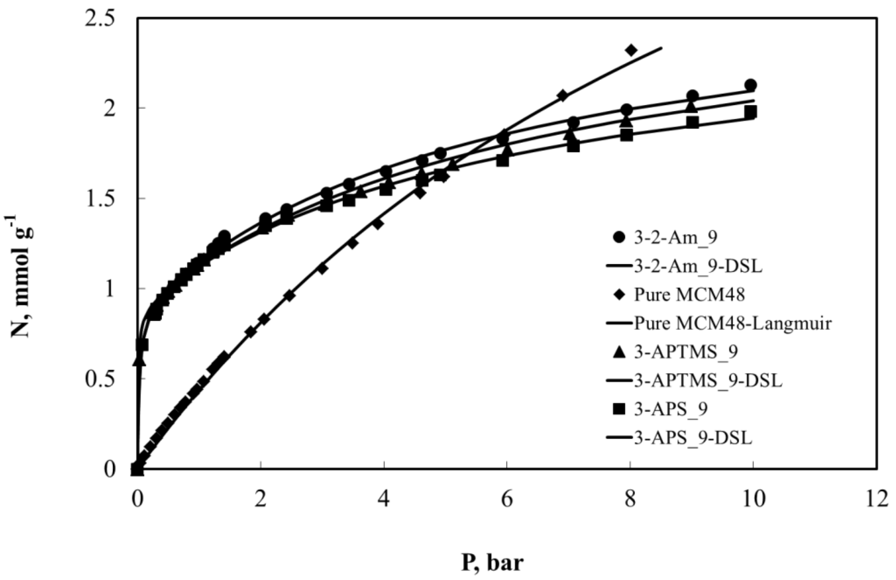

Figure 3.6 CO_2 isotherms of different MCM-48 samples at 30 ^{o}C. Symbols are experimental data and lines are fits obtained using Langmuir (for pure MCM-48 sample) and DSL (for amine grafted MCM-48 samples) isotherm parameters from Table 3.3.

Table 3.2 CO_2 Adsorption Capacity of 3-APS Grafted Silica Adsorbents[a]

Support material	**Amine content (mmol N/g)**	**CO_2 Adsorption Capacity (mmol/g)**	**References**
Silica gel	1.20	0.41	[**22**]
Xerogel	1.70	1.12	[**5**]
HMS	1.93	0.86	[**23**]
SBA-15	2.10	1.05	[**24**]
MCM-41	2.22	1.20	[**25**]
MCM-48	2.45	0.80	[**6**]
MCM 48	2.28	1.68	[**8**]
MCM 48	2.30	2.05	[**5**]
MCM 48	**2.77**	**1.16**	**This work**
MCM 48	**4.80**	**1.18**	**This work**

[a] ~1 bar, ~30°C

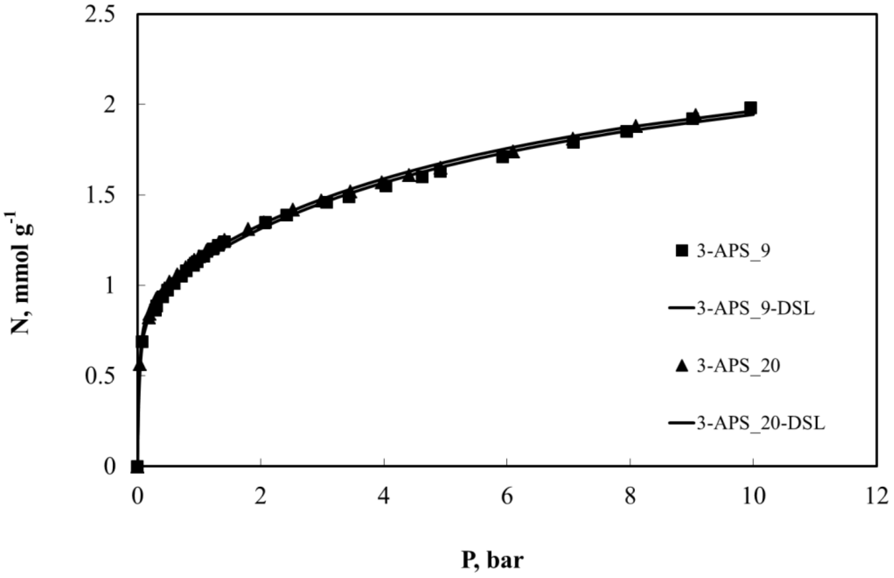

Figure 3.7 CO_2 isotherms of OMS (MCM-48) samples with different 3-APS loading content at 30 °C.

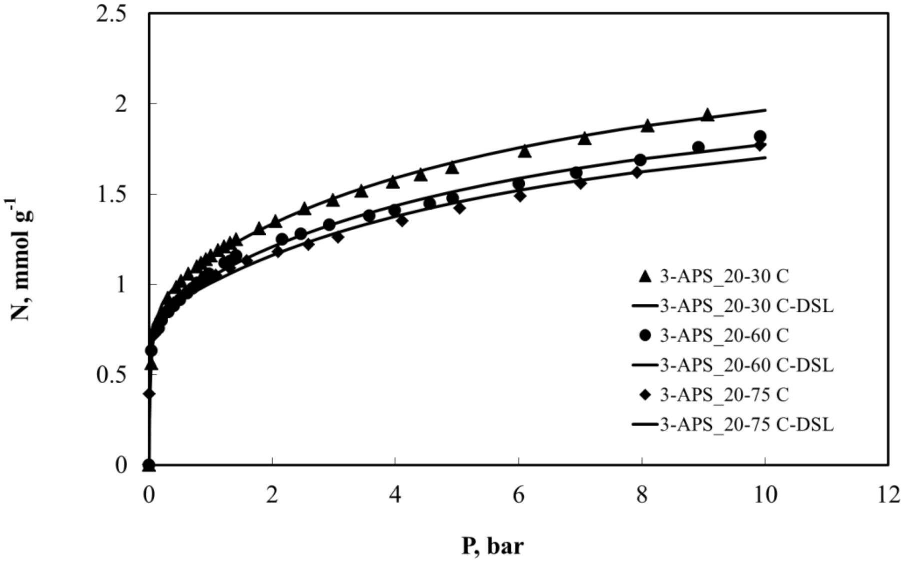

Figure 3.8 CO_2 isotherms of 20 mmol 3-APS loaded MCM-48 sample at different temperatures.

Isotherm modeling gives molecular level insights into adsorption characteristics. CO_2 isotherm of pure MCM-48 material follows the Langmuir model (Eq. 3.1) indicating the homogeneous adsorption nature of MCM-48 structure. In contrast, CO_2 isotherm on amine grafted samples could not be fitted using a Langmuir equation. Indeed, a Dual Site Langmuir (DSL) model (Eq. 3.2) describes the adsorption behavior of amine grafted samples well. Interactions between CO_2 molecules and functionalized $-NH_2$ groups are expected to be significantly stronger than those between CO_2 molecules and rest of the accessible surface of a sample. This difference in interactions is resulting into Dual Site adsorption behavior for amine grafted samples. In the fitted DSL model, the first site with higher adsorption energetics corresponds to $-NH_2$ groups whereas second site having lower adsorption energetics relates to the rest of the accessible surface. Fit parameters for all the samples are enlisted in Table 3.3. These fits are included in Figure. 3.6 – 3.8 in the form of lines along with the experimental data.

A Langmuir (DSL) model can be written as

$$A = \frac{A_{\max} bP}{1 + bP} \tag{3.1}$$

where A (mmol g^{-1}) is the excess amount adsorbed, P (bar) is the pressure, A_{max} (mmol g^{-1}) is the saturation capacity, b (bar^{-1}) is the affinity parameters.

The Dual Site Langmuir (DSL) model can be written as

$$A = \frac{A^1_{\max} b_1 P}{1 + b_1 P} + \frac{A^2_{\max} b_2 P}{1 + b_2 P} \tag{3.2}$$

Table 3.3 Model parameters for adsorption isotherms on different MCM-48 materials*.

Sample Name	**Parameters**	**CO_2 coefficient**	**Std.error**
Pure MCM 48	A_{max}	5.50	0.202
	b	0.086	0.0045
3-2-Am_9	A^1_{max}	0.873	0.0225
	b_1	39.007	7.2901
	A^2_{max}	1.915	0.058
	b_2	0.178	0.0172
3-APS_9	A^1_{max}	0.918	0.0236
	b_1	32.247	5.4114
	A^2_{max}	1.656	0.0687
	b_2	0.165	0.0205
3-APS_20	A^1_{max}	0.931	0.0168
	b_1	39.403	4.1599
	A^2_{max}	1.65	0.0542
	b_2	0.169	0.016
3-APS_10	A^1_{max}	0.81	0.0132
	b_1	40.514	4.494
	A^2_{max}	1.449	0.0495
	b_2	0.141	0.0129
3-APS_15	A^1_{max}	0.829	0.0158
	b_1	868.555	321.165
	A^2_{max}	1.285	0.047
	b_2	0.257	0.0308
3-APS_20_45	A^1_{max}	1.0321	0.0797
	b_1	16.771	6.1661
	$A2_{max}$	1.783	0.6527
	b_2	0.0911	0.0663
3-APS_20_60	A^1_{max}	0.846	0.0219
	b_1	56.255	11.0728
	A^2_{max}	1.499	0.081
	b_2	0.164	0.0243
3-APS_20_75	A^1_{max}	0.809	0.0183
	b_1	225.974	40.4106
	A^2_{max}	1.441	0.1106
	b_2	0.163	0.0297
3-APTMS_9	A^1_{max}	0.875	0.0193
	b_1	95.763	17.4415
	A^2_{max}	1.912	0.0921
	b_2	0.157	0.0192

* *The units of* A_{max}, A^1_{max} and A^2_{max} *are* (mmol g^{-1}); and for b_1 and b_2 are (bar^{-1})

where, A^1_{max} and A^2_{max} (mmol g^{-1}) are the saturation capacity of adsorption site 1 and 2 respectively, b_1 and b_2 (bar^{-1}) are the affinity parameters of site 1 and 2 respectively. Saturation loadings are considered to be independent of temperature

Henry's constant measures the adsorbate – adsorbent interaction at zero loading. Hence, Henry's constants at 30 ^oC are shown in Figure 3.9 to demonstrate the effect of amines on the interaction of CO_2 molecules with the surface of amine loaded MCM-48 samples at zero loading. Henry's constants are calculated from modeling fits. It can be seen that Henry's constant of MCM-48 material (0.47 mmol g^{-1} bar^{-1}) is significantly lower than that of samples containing 9 mmol of different amines (29 - 84 mmol g^{-1} bar^{-1}). This huge variation in Henry's constant clearly indicates that CO_2 molecules are having specific interaction with amino functional groups, which is much stronger than weak van-der Wall interactions in case of pure MCM-48 sample. In one hand, Henry's constant should be higher to have better CO_2 uptake at low pressure, however, for sake easier regeneration, Henry's constant should also not be very high. Hence, a striking balance between adsorption uptake and Henry's constant is required to obtain optimal process performance. The CO_2 uptake at 0.20 bar and 30 ^oC of 3-APS_9 sample is comparable to that of other amine loaded samples but lower Henry's constant for 3-APS_9 make this a better material for the CO_2 capture from flue gas. Hence, for further study, 3-APS amine loaded samples are considered.

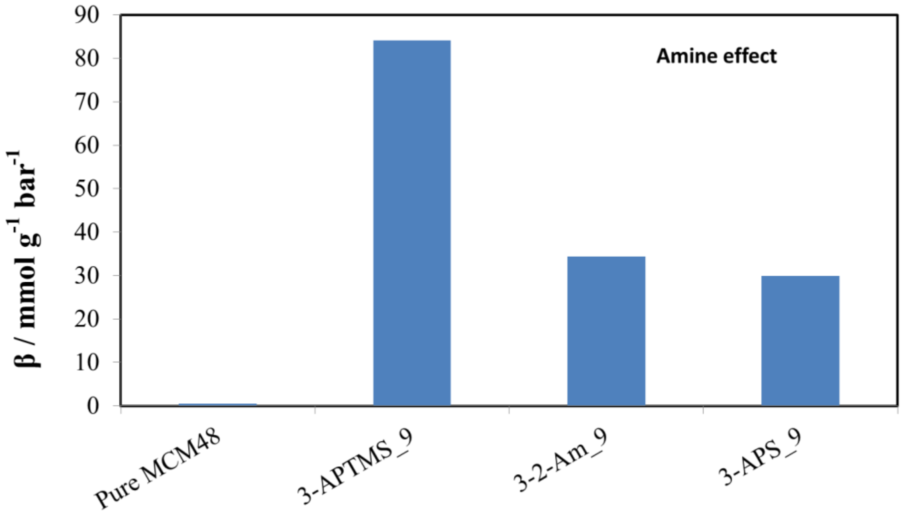

Figure 3.9. CO_2 Henry's constant of pure MCM-48 and amine loaded MCM-48 samples at 30 °C.

Henry's constant of 3-APS_9 and 3-APS_20 samples at 30 °C are compared in Figure 3.10 to observe the effect of the amount of amine -grafting. It can be seen that the difference between Henry's constant of the two samples is very marginal. This trend is in sequence with the trend observed for isotherms. As earlier mentioned during isotherm discussion, similar values of Henry's constants for both samples suggests that 9mmol of 3-APS per 1 gm of -MCM-48 saturates functional groups of OMS (MCM-48) sample during grafting.

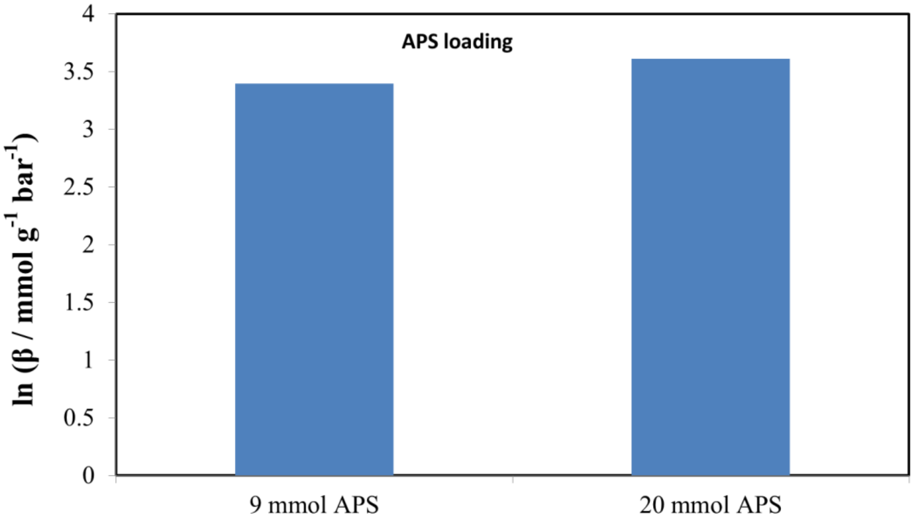

Figure 3.10. Henry's constant of 3-APS loaded OMS (MCM-48) samples at 30 °C.

4.5. Conclusions

The effects of grafting of different amines are investigated on MCM-48 materials for its CO_2 adsorption characteristics. Pure MCM-48 material exhibits a typical type IV shape (characteristic of mesoporous material) for N_2 adsorption isotherm, while that of the amine grafted MCM-48 material is the type I microporous. It is observed that at low pressures up to 4 bar, amine loaded MCM-48 samples exhibit more CO_2 uptake, whereas at higher pressures pure MCM-48 shows better CO_2 loading at room temperature (30 °C). CO_2 adsorption at 0.2 bar and 30 °C is increased significantly from ~0.1 mmol g^{-1} to ~0.84 mmol g^{-1} after grafting of 9 mmol of different amine on 1 g of MCM-48 material. CO_2 uptake obtained for amine grafted MCM-48 samples is comparable to the available literature. The degree of grafting is similar for all three amines such as 3-2 Am, 3-APTMS, 3-APS considered in this work. Small differences between uptakes of different amine grafted samples are attributed to the difference in their surface areas. It can be observed that adsorption uptake decreases with the increase of temperature. This indicates that the interactions between CO_2 molecules and adsorbent samples are exothermic in nature. CO_2 isotherm of pure MCM-48 material follows the Langmuir model indicating the homogeneous adsorption nature of MCM-48 structure. In contrast, CO_2 isotherm on amine grafted samples follow Dual Site Langmuir (DSL) model. It can be seen that Henry's constant of pure MCM-48 material (0.47 mmol g^{-1} bar^{-1}) is significantly lower than that of samples containing 9 mmol of different amines (29 - 84 mmol g^{-1} bar^{-1}) indicating that CO_2 molecules are having specific interaction with amino functional groups, which is much stronger than weak van der Waals interactions in case of the pure MCM-48 sample.

References

[1] Hicks, J.C.; Drese, J. H.; Fauth, D. J.; Gray, M. L.; Qi, G.; Jones, C. W. Designing adsorbents for CO_2 capture from flue gas-hyperbranched aminosilicas capable of capturing CO_2 reversibly. *J. Am. Chem. Soc.* **2008,** *130*, 2902-2903.

[2] Chandrasekar, G.; Son, W. J.; Ahn, W. S. Synthesis of mesoporous materials SBA-15 and CMK-3 from fly ash and their application for CO_2 adsorption. *J. Por. Mater.* **2009,** *16*, 545-551.

[3] Hiyoshi, N.; Yogo, K.; Yashima, T. Adsorption Characteristics of Carbon dioxide on Organically Functionalized SBA-15, *Micropor. Mesopor. Mater.* **2005,** *84*, 357-365.

[4] Jang, H. T.; Park, Y.; Ko, Y. S.; Lee, J. Y.; Margandan, B. Highly siliceous MCM-48 from rice husk ash for CO_2 adsorption. *Int. J. Greenh. Gas. Con.* **2009,** *3,* 545-549.

[5] Huang, H. Y.; Yang, R. T.; Chinn, D.; Munson, C. L. Amine-grafted MCM-48 and silica xerogel as superior sorbents for acidic gas removal from natural gas. *Ind. Eng. Chem. Res.* **2003,** *42*, 2427-2433.

[6] Kim, S.; Ida, J.; Guliants, V. V.; Lin, J. Y. S. Tailoring pore properties of MCM-48 silica for selective adsorption of CO_2. *J. Phys. Chem. B.* **2005,** *109*, 6287-6293.

[7] Margandan, B.; Lee, J. Y.; Ramani, A.; Jang, H. T. Synthesis of chloropropylamine grafted mesoporous MCM-41, MCM-48 and SBA-15 from rice husk ash: their application CO_2 chemisorption. *J. Porous Mater.* **2010,** *17*, 475-484.

[8] Gil, M.; Tiscornia, I.; de la Iglesia, O.; Mallada, R.; Santamaría, J. Monoamine-grafted MCM-48: An efficient material for CO_2 removal at low partial pressures. *Chem. Eng. J.* **2011,** *175,* 291-297.

[9] Chang, F.Y.; Chao, K. J.; Cheng, H. H.; Tan, C. S. Adsorption of CO_2 onto amine grafted mesoporous silicas. *Sep. Purif. Technol.* **2009,** *70,* 87-95.

[10] Choi, S.; Drese, J. H.; Jones, C.W. Adsorbent materials for carbon dioxide capture from large anthropogenic point sources. *Chem. Sus.Chem.* **2009,** *2(9),* 796-854.

[11] Harlick, P. J. E.; Sayari, A. Applications of pore-expanded mesoporous silica. 5. Triamine grafted material with exceptional CO_2 dynamic and equilibrium adsorption performance. *Ind. Eng. Chem. Res.* **2007,** *46,* 446-458.

[12] Sakamoto, Y.; Nagata, K.; Yogo, K.; Yamada, K. Preparation and CO_2 separation properties of amine-modified mesoporous silica membranes. *Micropor. Mesopor. Mater.* **2007,** *101,* 303-311.

[13] Jaroniec, C. P.; Kruk, M.; Jaroniec, M.; Sayari, A. Tailoring Surface and Structural Properties of MCM-41 Silicas by Bonding Organosilanes, *J. Phys. Chem. B* **1998,** *102,* 5503.

[14] Cauvel, A.; Renard, G.; Brunel, D. Monoglyceride Synthesis of Heterogeneous Catalysis Using MCM-41 Type Silicas Functionalized with Amino Groups, *J. Org. Chem.* **1997,** *62,* 749.

[15] Lasperas, M.; Llorett, T.; Chaves, L.; Rodriguez, I.; Cauvel, A.; Brunel, D. Heterogeneous Catalysis and Fine Chemicals. *Elsevier Science: New York*, **1997;** Vol. IV, p 75.

[16] Macquarrie, D. J. Direct Preparation of Organically Modified MCM-type Materials. Preparation and Characterisation of Aminopropyl-MCM and 2-Cyanoethyl-MCM. *Chem. Commun.* **1996,** 1961-1962.

[17] Tomski, P. 1st Ohio Carbon Dioxide Reduction, Sequestration and Capture Forum, **2001.**

[18] Mercier, L.; Pinnavaia, T. Heavy Metal Ion Adsorbents Formed by the Grafting of a Thiol Functionality to Mesoporous Silica Molecular Sieves: Factors Affecting Hg(II) Uptake, *J. Environ. Sci. Technol.* **1998,** *32,* 2749-2754.

[19] Evans, J.; Zaki, A. B.; El-Sheikh, M. Y.; El-Safty, S. A. Incorporation of Transition-Metal Complexes in Functionalized Mesoporous Silica and Their Activity toward the Oxidation of Aromatic Amines. *J. Phys. Chem. B.* **2000,** *104*, 10271-10281.

[20] Zhao, X. S.; Lu, G. Q. Modification of MCM-41 by Surface Silylation with Trimethylchlorosilane and Adsorption Study. *J. Phys. Chem. B* **1998,** *102,* 1556-1561.

[21] Autochshuk, V.; Jaroniec, M. Functionalized Mesoporous Materials Obtained via Interfacial Reactions in Self-Assembled Silica−Surfactant Systems. *Chem. Mater.* **2000,** *12,* 2496-2501.

[22] Leal, O.; Bolivar, C.; Ovalles, C.; Garcia, J. J.; Espidel, Y. Reversible Adsorption of Carbon Dioxide on Amine Surface-Bonded Silica Gel. *Inorg. Chim. Acta* **1995,** *240*, 183-189.

[23] Knowles, G. P.; Graham, J. V.; Delaney, S. W.; Chaffee, A. L. Aminopropyl-Functionalized Mesoporous Silicas as CO_2 Adsorbents. *Fuel Process. Technol.* **2005,** *86*, 1435-1448.

[24] Bollini, P.; Brunelli, N. A.; Didas, S. A.; Jones, C. W. Dynamics of CO_2 Adsorption on Amine Adsorbents. 2. Insights into Adsorbent Design. *Ind. Eng. Chem. Res.* **2012,** *51*, 15153-15162.

[25] Loganathan, S.; Tikmani, M.; Ghoshal, A. K. Novel pore-expanded MCM-41 for CO_2 capture: synthesis and characterization. *Langmuir.* **2013,** *29*, 3491-3499.

[26] Mishra, P.; Edubilli, S.; Mandal, B.; Gumma, S. Adsorption Characteristics of Metal Organic Frameworks Containing Coordinatively Unsaturated Metal Sites: Effect of Metal Cations and Adsorbate Properties. *J. Phys. Chem. C.* **2014,** *118 (13)*, 6847-6855.

Chapter 4

SYNTHESIS & CHARACTERIZATION OF PURE ORDERED MESOPOROUS SILICA (OMS) POWDER OBTAINED BY ACIDIC AND BASIC ROUTES FOR CO_2 ADSORPTION

This chapter describes the synthesis and characterization for the OMS materials obtained by acidic route and compares the CO_2 adsorption capacity for for the OMS materials obtained by acidic route and basic route. The OMS materials are characterized by using N_2 adsorption-desorption analysis, TGA analysis, XRD analysis, FTIR analysis and TEM analysis. The CO_2 isotherms at 30 ^oC are measured up to 8 bars for OMS samples to find out CO_2 adsorption capacity. CO_2 adsorption studies show better results for OMS materials obtained by acidic route.

4.1. Introduction

Several synthesis strategies were discussed to synthesize ordered mesoporous silica materials (OMS) in literature [**1-4**]. The OMS materials include MCM-41, MCM-48, SBA-1, SBA-2, SBA-3, SBA-7, etc. Mesoporous silica materials are formed generally by micelle-templating process. In the presence of surfactant, the process may follow electrostatically driven cooperative assembly pathway or the non-ionic route [**5**]. The surfactant acts as structure directing agent. Electrostatic interaction may follow S^+I^- or $S^+X^-I^+$ pathways where S+ = $C_nH_{3n+1}N^+(CH_3)_3$, n = 8–18, and I^- is the anionic silicate species. X^- = counter cation. The steps followed by electrostatic interaction pathway are (1) displacement of the surfactant counterions by inorganic cations forming organic-inorganic pairs, which self-organize into a liquid crystal-like mesophase, (2) crosslinking of the inorganic species and (3) a rigid replica of the underlying liquid crystalline phase forms [**5**]. Huo et al.[**6**] proposed the synthesis of OMS by the S^+I^- route. In this route the reaction is carried out in alkaline conditions by self-assembly of anionic silicates and cationic surfactant molecules. The synthesis is performed under conventional hydrothermal conditions, which usually requires the reaction system be under a liquid self-pressure, and at high temperature for a long reaction time. However, the $S^+X^-I^+$ route achieves self-assembly via a different route from the former, but it uses the same long quaternary ammonium surfactant as a structure directing agent in acid condition, where X^- = Cl^-, Br^-, etc., and I^+ is a cationic silicate species. The acid anion, X^-, serves as buffer between the I^+ and the S^+ by means of weak hydrogen bonding forces in this route. Thus the $S^+X^-I^+$ route can offer more versatile structures and morphologies than the S^+I^- route, due to its weaker surfactant/silicate interaction in $S^+X^-I^+$. The association of S^+X^-

determines the structure and morphology of the mesoporous materials. The detail studies for OMS material under basic route have been discussed in Chapter 3 for CO_2 adsorption. However, an effort has been made in the present work to develop a comparative study for the OMS materials obtained by acidic route and basic route for CO_2 adsorption. This chapter describes the synthesis and characterization for the OMS materials obtained by acidic route and compares the CO_2 adsorption capacity for the OMS materials obtained by acidic and basic routes.

4.2. Materials

Ethyl alcohol (EMSURE R ACS, ISO, Reag. PhEur) and HCl (35%) were purchased from MERCK, Germany. Tetraethyl orthosilicate (TEOS), N-hexadecyl trimethyl ammonium bromide (CTAB), were supplied by Sigma Aldrich, India.

4.3. Experimental

4.3.1. Synthesis

4.3.1.1. Synthesis of OMS by basic route

The synthesis procedure is described in **section 3.3.1.1.**

4.3.1.2. Synthesis of OMS by acidic route

The silica sol of this work was prepared as per the method described by Besson et al. [**7**]. A mixture of EtOH, TEOS and diluted HCl (0.056 M, pH = 1.67) was taken into a beaker and was stirred for 1 h at room temperature. Then a required amount of CTAB was added to the mixture at room temperature with continuous stirring to dissolve it completely. The final sol was stirred continuously for 24 h for aging. The final molar ratio of the silica sol was CTAB: TEOS: H_2O (HCl): EtOH = 0.1:1:0.28:22. The silica sol was then taken out from the beaker and poured in a flat and open petridish. The sol was kept for overnight at room temperature in a laminar flow chamber (Dlab Tech, Clean Bench) for drying. Then the dried silica was removed by a spatula in powder form. Finally, the powder was calcined in the chamber furnace (Nabertherm, Germany) at 550^{o}C for 6 h with the heating and cooling rate of 0.5 ^{o}C/min.

4.3.2. Characterization techniques

The details about characterization of OMS powder samples have been elaborated in Chapter 3 (see section 3.3.2).

In addition to that, the transmission electron microscopic (TEM), high resolution TEM (HRTEM), and selected area electron diffraction (SAED) pattern of the samples deposited on formvar-carbon-coated copper grids have been performed in a JEOL JEM-2100 transmission electron microscope (operated at a maximum accelerating voltage of 200 kV). The powder samples are dispersed in 1 ml of ethanol. After 1 h, a few drops of suspension are deposited on the copper microgrid and are dried in air. The micro grids are evacuated for 1 h and TEM observation has been carried out.

4.3.3. CO_2 adsorption measurements

The details about CO_2 adsorption measurements have been described in Chapter 3 (see section 3.3.3).

4.4. Results and Discussions

4.4.1. Surface area analysis

The N_2 adsorption/desorption isotherms and pore size distributions of the prepared OMS materials obtained by two different routes are shown in Figures 4.1 & 4.2, respectively. The OMS sample obtained by acidic route and basic route are denoted as OMS_AC & OMS_H, respectively. Both the isotherms observed for the OMS materials show a typical type IV adsorption-desorption isotherm which confirms that the materials are ordered mesoporous in nature. N_2 adsorption-desorption isotherm pattern, surface area and pore volume of the OMS materials are highly comparable with the reported literature [**8-10**]. The BET surface areas of the OMS materials, total pore volume calculated from the nitrogen adsorption data in the relative pressure range of 0.01-1, are given in Table 4.1.

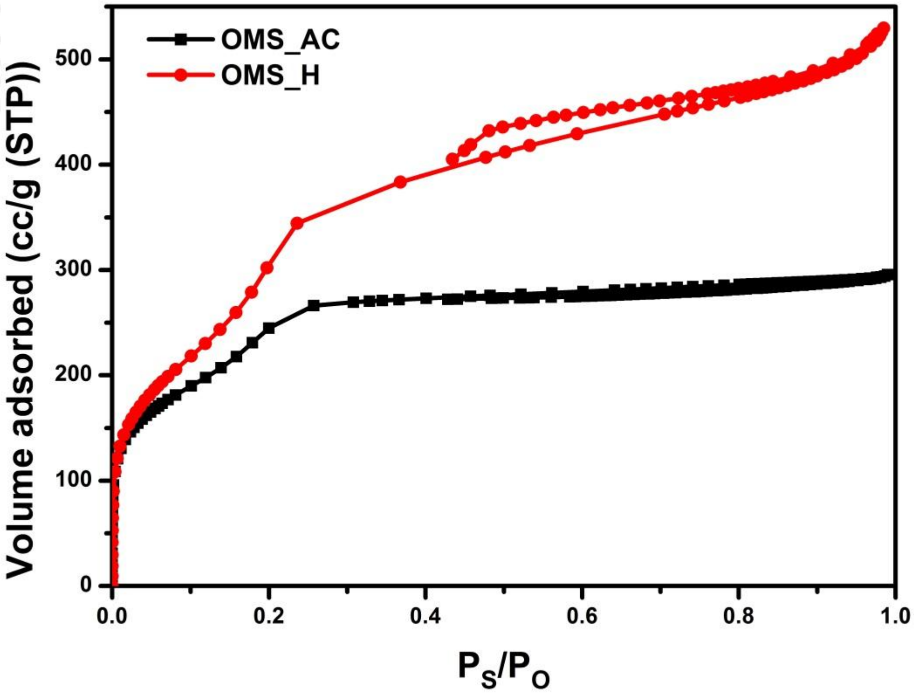

Figure 4.1 Adsorption-desorption isotherm of N_2 on different OMS samples at 77 K.

Table 4.1 BET surface area and pore volume of different OMS samples.

Sample Name	**BET surface area (m^2/g)**	**Pore volume (cc/g)**
OMS_H	1133.35	0.8114
OMS_AC	890.46	0.4541

It is observed from the table that the surface areas as well as pore volume of the OMS_H materials are larger compare to the sample OMS_AC. The pore size distribution is determined from desorption isotherm by the BJH method as shown in Figure 4.2.

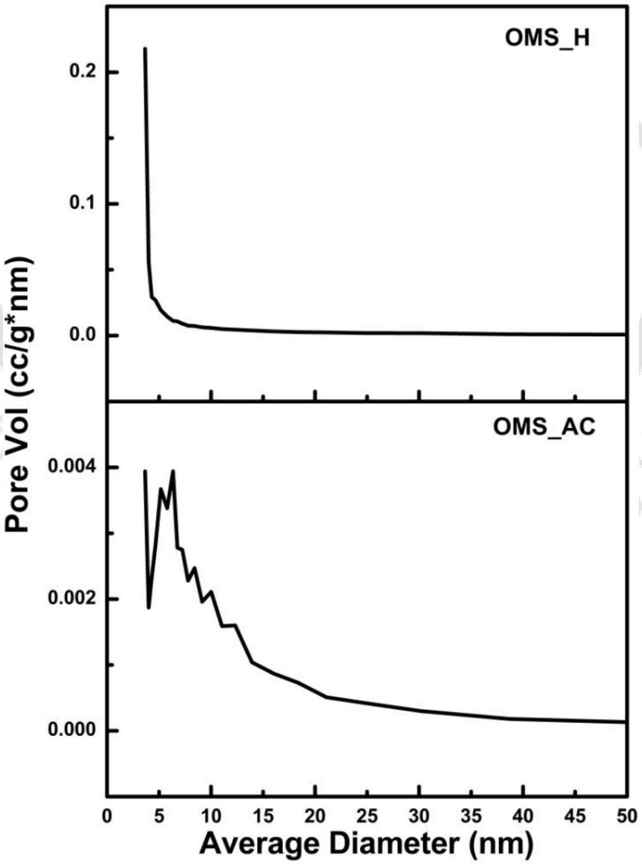

Figure 4.2 BJH pore size distribution profile for samples OMS_AC & OMS_H samples

It is observed from the figure that the average pore size for the sample MCM_AC is larger than the average pore size of the sample OMS_H. Figure 4.2 clearly shows that the average pore diameter of OMS_H is less than 5 nm whereas the average pore diameter of MCM_AC is around 6-7 nm. Due to the limitation of the instrument it is impossible to detect the average pore size of less than 5 nm. But the Figure 4.2 depicts that the value is definitely less than 5nm for sample OMS_H. The average pore diameter of the OMS materials such as MCM-41, MCM-48 are comparable with our results.

4.4.2. FTIR analysis

Figure 4.3 shows the FTIR spectrum for both the OMS materials synthesized by different routes after calcination. It is observed that there is no significant change in the FTIR bands between OMS_H and OMS_AC powders. The bands corresponding to ordered mesoporous silica materials are in same position for both the materials. The band at 960 cm^{-1} is corresponding to the presence of Si–OH stretching vibration. A broad band seen at around 3500 cm^{-1} is attributed to surface silanol groups. The asymmetric and symmetric stretching vibrations of Si-O-Si are seen at 1070 cm^{-1} and 799 cm^{-1} respectively. The band at 958 cm^{-1} is attributed to Si-OH asymmetric vibrations [**11**]. All the bands corresponding to the organic groups are disappeared for the sample calcined at 550 ^{o}C. This proves that the surfactant is removed from the sample calcined at 550 ^{o}C.

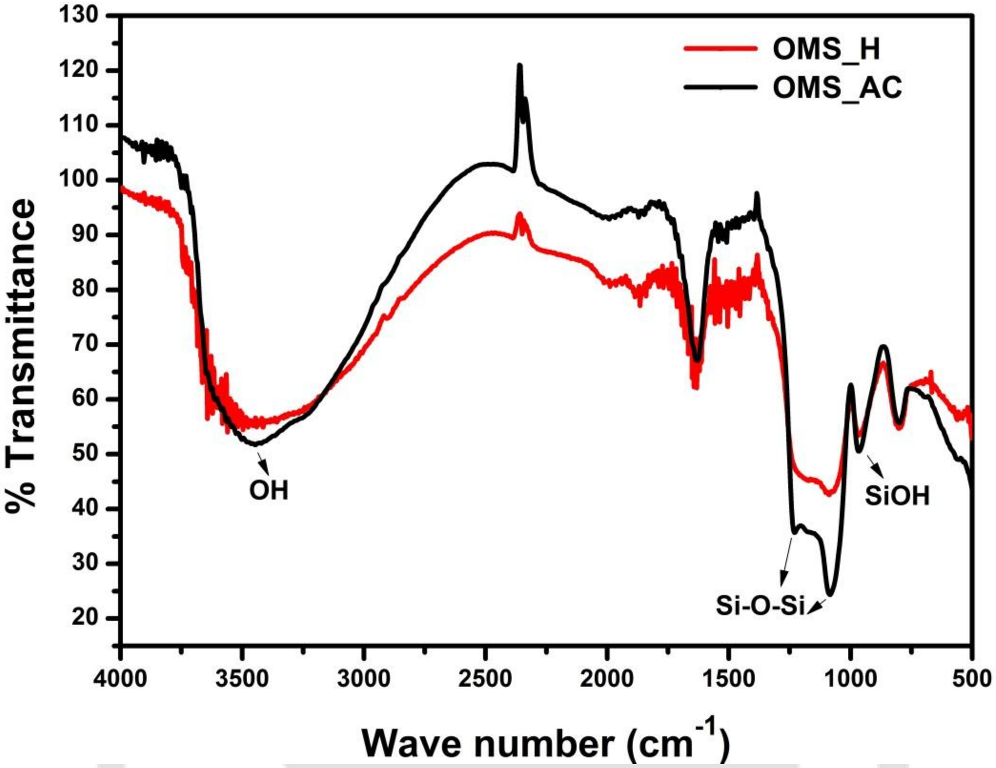

Figure 4.3 FTIR spectra for OMS materials synthesized by various routes

4.4.3. Thermo-gravimetric analysis

Thermo gravimetric (TGA) analysis of the OMS materials is shown in Figure 4.4. The figure exhibits an initial weight loss in the temperature range 30–100 °C for both the samples due to loss of moisture and hydrated water. After the region 200–600 °C, there is a marginal/negligible weight loss which indicates thermally stable nature of both the materials. This also indicates that the surfactant is completely removed from both the OMS materials after calcination at 550 ^{o}C.

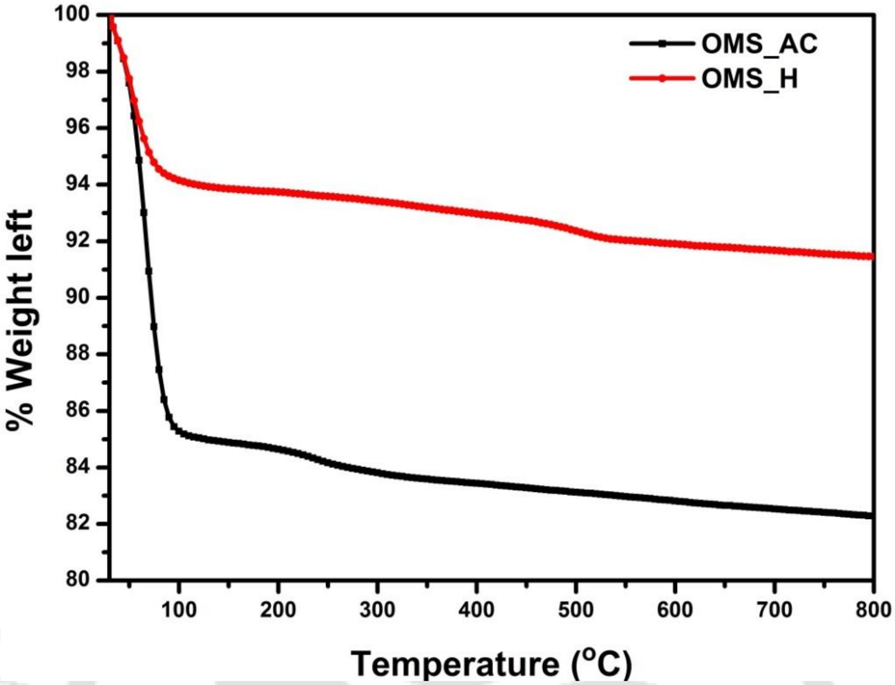

Figure 4.4 Thermo-gravimetric analysis for the OMS samples synthesized by various routes

4.4.4. X-ray diffraction analysis

X-ray diffraction patterns for the OMS materials are shown in Figure 4.5. For the powder material of OMS_H produced by hydrothermal method, it is observed from the figure that the XRD patterns are identical to MCM-48 which is already discussed in Chapter 3 (see section 3.4.4). Whereas the XRD pattern for OMS_AC is identical to MCM-41. The XRD profiles for the OMS_AC demonstrate a strong (100) peak and three higher order reflections such as (110), (200) and (210) at 2θ range of 2^o-10^o. It can be observed for the sample OMS_H that a dominant (211) peak with small (220), (420) and (322) reflections, are attributed to 3D-cubical (Ia3d) pore structure [**12**] whereas, the presence of (1 0 0), (1 1 0) and (2 0 0) diffraction peaks in the OMS_AC specifies the existence of well-resolved hexagonally assembled pore geometry [**9, 13**]. The presence of the prominent peaks for both the samples also signifies the confirmation of good crystallinity of the prepared powder.

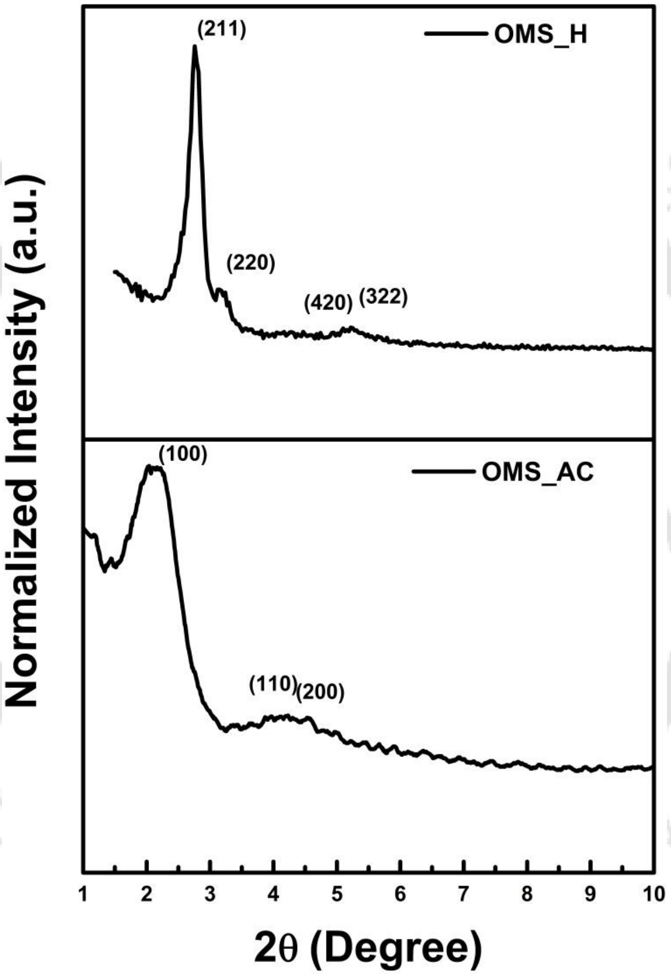

Figure 4.5 X-ray diffraction peaks for the OMS materials

4.4.5. Transmission electron microscopy (TEM) analysis

The TEM image shown in Figures 4.6(a) and 4.6(b) clearly illustrates an ordered arranged pore channel structure. The highly ordered mesoporous structures are observed over a wide area of both the sample. The Figure 6(a) shows 3-D cubical structure of MCM-48 materials [**8**] which matches with the XRD pattern. However, the figure 6 (b) shows hexagonal structures of MCM-41 [**14**] which also matched with the XRD patterns of OMS_AC sample. The hexagonal structures of OMS_AC sample are also confirmed by the SAED pattern in Figure 4.7.

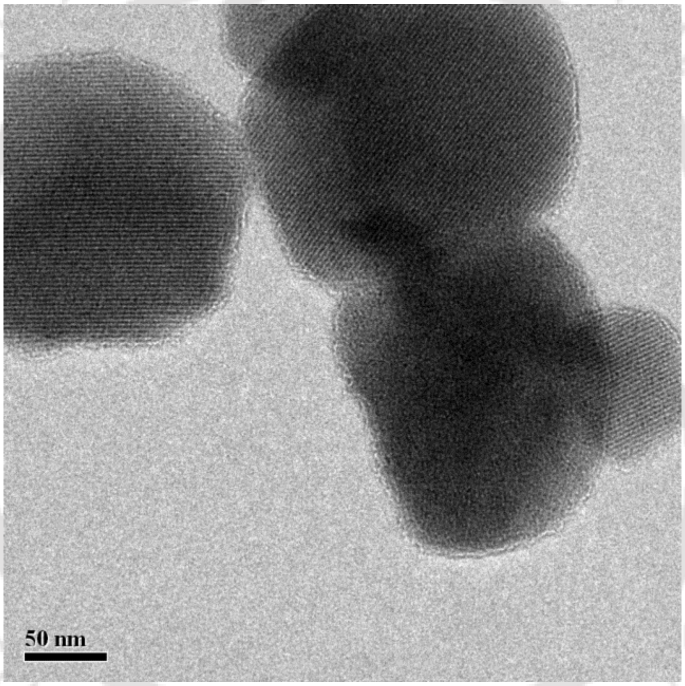

Figure 4.6(a) TEM image of OMS synthesized under basic route (OMS_H)

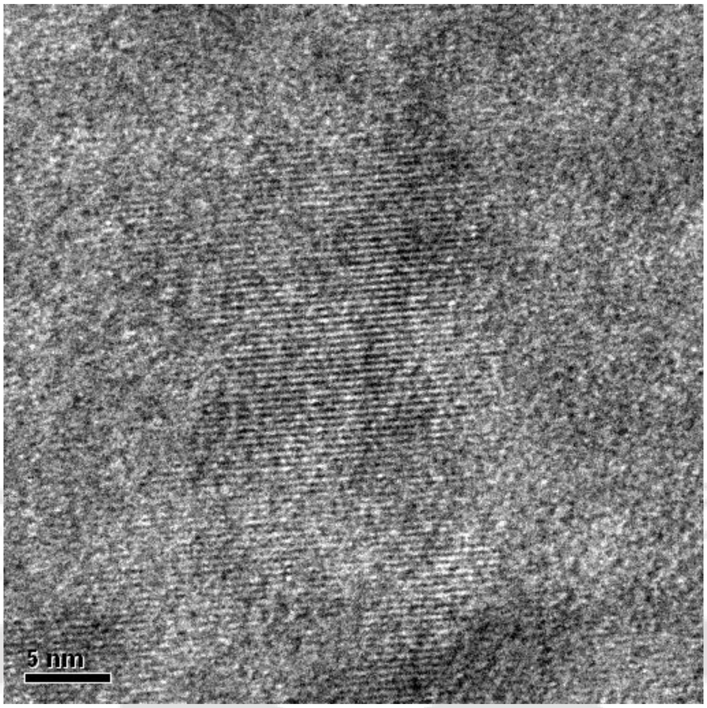

Figure 4.6(b) TEM image of OMS synthesized under acidic route (OMS_AC)

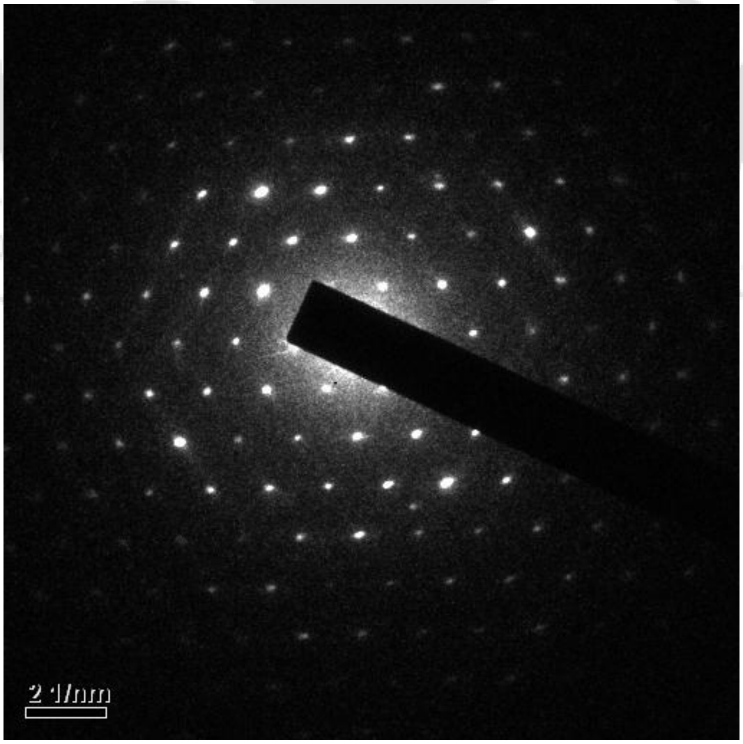

Figure 4.7 The SAED patterns of OMS synthesized under acidic route (OMS_AC)

4.4.5. CO_2 adsorption analysis

The CO_2 adsorption capacity measurements on to samples OMS_AC & OMS_H are obtained at room temperature at the pressure range of ~ (0-9) bar is shown in Figure 4.8. The isotherms are found to be Type I according to the IUPAC classification for adsorption isotherms. The adsorption capacities of samples OMS_AC ranging from low pressure to 8 bar gives slightly higher value compared to OMS_H materials.

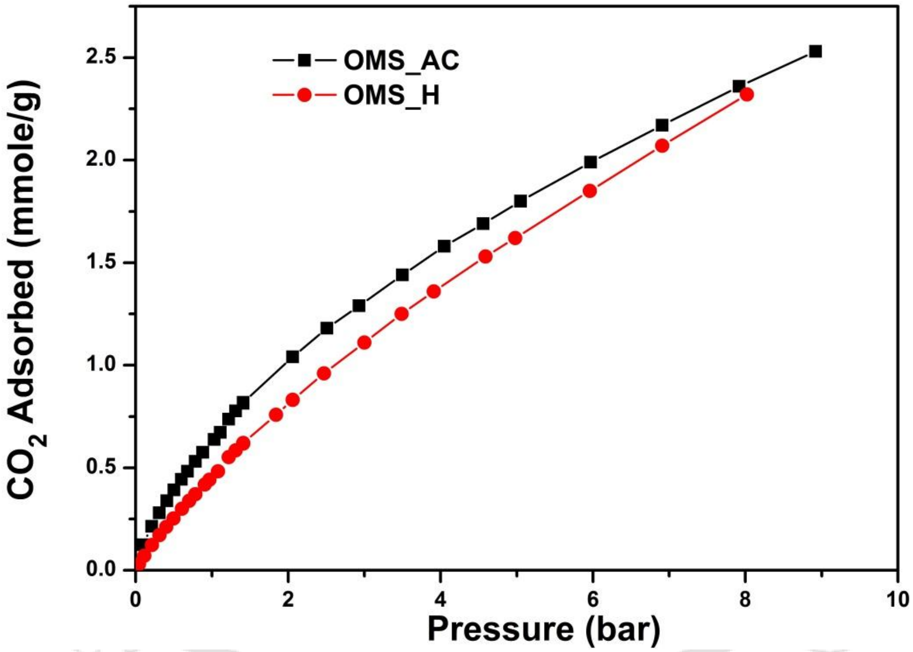

Figure 4.8 CO_2 adsorption isotherm of samples OMS_AC & OMS_H at 30 ^oC

At high pressure after about 8 bar it seems higher CO_2 adsorption capacity for the sample OMS_H compared to OMS_AC. High surface area and high pore volume may be possible reason for higher CO_2 adsorption capacity for OMS_H samples at higher pressures which is consistent with the literature [**15**]. At lower pressure ranges the higher CO_2 adsorption capacity for OMS_AC samples may be due to the higher average pore diameter. It is seen from the figure 4.8 that at about 1 bar pressure the CO_2 adsorption capacity for OMS_AC and OMS_H samples are observed to be ~0.63 mmol/g and ~0.48 mmol/g respectively. Hence, sample OMS_AC can be utilized for CO_2 capture due to cost effectiveness.

4.5. Conclusions

Both hydrothermal (basic) as well acidic routes gives well-ordered mesoporous pore structures for the materials. It is found that an energy intensive process for synthesizing ordered mesoporous materials by using acidic route gives a promising alternative for CO_2 capture technologies. Therefore, this technology can act as a promising scope for membrane synthesis by coating process for CO_2 capture.

References

[1] Mortera, R.; Fiorilli, S.; Garrone, E.; Verné, E.; Onida, B. Pores occlusion in MCM-41 spheres immersed in SBF and the effect on ibuprofen delivery kinetics: a quantitative model. *Chem. Eng. J.* **2010**, *156*, 184-192.

[2] Pang, X.; Gao, J.; Tang, F**.** Controlled preparation of rod- and top-like MCM- 41 mesoporous silica through one-step route. *J. Non-Cryst. Solids.* **2005,** *351*, 1705-1709.

[3] Frasch, J.; Lebeau, B.; Soulard, M.; Patarin, J. Insitu investigations on cetyltrimethylammonium surfactant/silicate systems, precursors of organized mesoporous MCM-41-type siliceous materials. *Langmuir*. **2000,** *16*, 9049-9057.

[4] Angloher, S.; Kecht, J.; Bein, T. Optimization of reaction conditions for the metalorganic modification of MCM-41. *Chem. Mater*. **2007,** *19*, 3568-3574.

[5] Sayari, A.; In: Yang P, editor. The chemistry of nanostructured materials. USA: World Scientific; **2003.** p. 39.

[6] Huo, Q.; Margolese, D. I.; Ciesla, U.; Demuth, D. G.; Feng, P.; Gier, T. E.; Chmelka, B. F.; Schuth, F.; Stucky, G.D. Organization of Organic Molecules with Inorganic Molecular Species into Nanocomposite Biphase Arrays. *Chem. Mater*. **1994,** *6*, 1176-1191.

[7] Besson, S.; Ricolleau, C.; Gacoin, T.; Jacquoid, C.; Boilot, J. P. A New 3D Organization of Mesopores in Oriented CTAB Silica Films. *J. Phys. Chem. B* **2000,** *104*, 12095-12097.

[8] Gil, M.; Tiscornia, I.; de la Iglesia, Ó.; Mallada, R.; Santamaría, J. Monoamine-grafted MCM-48: An efficient material for CO_2 removal at low partial pressures. *Chem. Eng. J.* **2011,** *175*, 291-297.

[9] Liou, T. H. A green route to preparation of MCM-41 silicas with well-ordered mesostructure controlled in acidic and alkaline environments. *Chem. Eng. J.* **2011,** *171,* 1458-1468.

[10] Xiang, W. D.; Yang, Y. X.; Zheng, J. L.; Cao, L.; Ding, H.J.; Liu, X.N. Synthesis of mesoporous silica by cationic surfactant templating in various inorganic acid sources. *Mater. Sci. Poland.* **2010,** *28,* 709-730.

[11] Loganathan, S.; Tikmani, M.; Ghoshal, A. K. Novel pore-expanded MCM-41 for CO_2 capture: synthesis and characterization. *Langmuir*. **2013,** *29*, 3491-3499.

[12] Kresge, C. T.; Leonowicz, M. E.; Roth, W. J.; Vartulli, J. C.; Beck, J. S. Ordered mesoporous molecular sieves synthesized by a liquid-crystal template mechanism. *Nature*. **1992,** *359*, 710-712.

[13] Udayakumar, S.; Pandurangan, A.; Sinha, P. K. Mesoporous materialas catalyst for the production of fine chemical: synthesis of dimethyl phthalate assisted by hydrophobic nature MCM-41. *J. Mol. Catal. A: Chem*. **2005,** *240*, 139-154.

[14] Liu, Z.; Wei, Y.; Qi, Y.; Zhang, S.; Zhang, Y.; Liu, Z. Synthesis of MCM-41 type materials with remarkable hydrothermal stability from UTM-1. *Micropor. Mesopor. Mater*. **2006,** *93*, 205-211.

[15] Belmabkhout, Y.; Serna-Guerrero, R.; Sayari, A. Adsorption of CO_2 from dry gases on MCM-41 silica at ambient temperature and high pressure.1:Pure CO_2 adsorption. *Chem. Eng. Sci.* **2009,** *64*, 3721-3728.

Chapter 5

SYNTHESIS AND OPTIMIZATION OF HIGH SURFACE QUALITY α-ALUMINA COMPACT MEMBRANE SUPPORT

This chapter reports the effect of sintering temperature and compaction load on the quality of α-alumina membrane support for dry compaction method. The effect of initial compaction load on porosity, pore size, flexural strength and shrinkage during synthesis of α-alumina support at various sintering temperatures are investigated to find the best quality support for synthesizing spin-coated silica membrane for gas separation application. This part of work has been published in ***Ceramics International*** *40 (2014) 11299–11309.*

5.1. Introduction

In the preparation of mesoporous ceramic membranes, the quality of the support is of crucial importance to the membrane layer integrity. There is relatively very little study published in open literature on the support development compared to the huge efforts to develop better membranes for gas separation. Design and fabrication of porous ceramic membrane requires several layers of different materials. The foundation of the structure is a thick, macro-porous support that carries one or more intermediate as well as selective top layers of other ceramic materials [**1**]. A defect on the surface of the selective top layer significantly decreases the selectivity. Since only the top layer has separating capacities, the support must have an excellent surface morphology for deposition of subsequent layers but retain sufficient permeability. So it is consequently very important to favour the development of low cost, high Surface /Volume ratio, highly permeable supports, and good surface quality ensuring the right conditions for coating high-quality membrane layers.

A ceramic membrane support is commonly prepared by shaping a powder into a green body and then by sintering the obtained green body into the final membrane support. In case of green bodies' processing, it is common to use organic binders. These organic binders are eliminated during the heat treatment step. Most of the silica membranes reported in the literature are deposited either on alumina-based supports (macro porous α-Al_2O_3 with a mesoporous final layer) [**2-4**] or on Vycor glass [**5**]. α-Al_2O_3 is a more desirable support than Vycor glass because of its higher permeability and resistance to high pressures. Stainless steel is also used as a support in several studies [**6**]. Metals simplify the sealing problem at high temperature but their high expansion coefficients hardly match with that of silica. α-alumina support of small pore size is normally prepared by sintering compacted α-alumina powder at higher temperature. Properties such as pore size, porosity, density, particle size, etc.) of the membrane support change significantly under processing conditions like sintering temperature, control of heating and cooling rate, sintering time, etc. [**7**]. Effects of sintering on properties of the alumina compacts have been studied in the literature [**8-13**]. Some of these studies reported that mean pore sizes of compacts with the increase in sintering temperature increased [**8, 10**]. However, Page and Pan [9] observed that the pore size remained constant during the sintering process. Fang and Palmour III [**10**] reported that the transition of pore size during the sintering process depends on the porosity of the green compacts. Lim et al. [**13**] reported that despite being agglomerate-free green body to start with, agglomeration of particles still occurred during sintering. The main reason was believed to be the local differential densification effect produced by different co-ordination numbers of the individual particles. This led to the formation of channel-like pores, which then evolved into smaller isolated pores. A lower sintering temperature for α-alumina is preferred for the reduction of processing cost and finer grain sizes [**14**]. The sintering of α-alumina at different temperatures was studied with the sintering time of about 1 to 10 h [**11-16**]. Kumar et al. [**4**] reported the sintering treatment of α-alumina support at1500 ^{o}C for 30 h to obtain pore size of 200 nm. Effect of initial compaction load on the α-alumina membrane support quality has not been studied thoroughly in the literature. However, in the dry compaction method, starting with compacted green support may increase the density of the final support at a lower sintering temperature. Applying more initial loads during the synthesis will give more densified green disc. Meanwhile, the good quality membrane support (with lower pore size, sufficient porosity, sufficient gas permeability and smooth surface) can be useful for synthesis of a defect free thin-film MCM-48 membrane [**4**] on it.

5.2. Materials

Poly (vinyl alcohol) (98-99 mol% hydrolyzed powder) was obtained from Loba Chemie Pvt. Ltd, Mumbai, India. α-Alumina powder (Alfa Aesar, 99.9% (metals basis), size<1 micron APS powder, SA 6-8 m^2/g) was procured from Alfa Aesar, USA.

5.3. Experimental

5.3.1. Membrane support synthesis

The membrane supports were prepared by dry compaction method using poly(vinyl alcohol) (PVA) as a binder. Initially, the binder solution was prepared by adding small amount (2 wt %) of solid PVA with distilled water followed by heating the mixture at 80^oC to get a clear solution (viscous in nature). The final powder was prepared by mixing a required amount of binder solution (~10 wt%) in dry α-alumina powder followed by sieving. A requisite amount of the mixed α-alumina powder was uniaxially pressed in a Compression Testing Machine (Aimil) by applying different constant loads (50 kN, 150 kN, 250 kN and 350 kN) for 5 minutes. A custom made stainless steel mould (Figure 5.1.) was used to make the circular disc membrane support. The supports thus obtained were carefully kept in a hot air oven at 150^oC for 24h for drying. Thereafter, the sintering was done at different temperatures (1200^oC, 1300^oC, 1400^oC and 1500^oC) using high temperature chamber furnace with P310 controller (Nabertherm, Germany) (Figure 5.2.).

The supports were kept for 4h (holding time) at those temperatures with the heating and cooling rate of ~2^{o}C/minute. To obtain smooth surface as well as required diameter for the gas permeation module (Figure 4.4), sintered membranes were then polished using silicon carbide abrasive paper (No. C-320). The membrane supports thus obtained were cleaned ultrasonically (Elmasonic P-30H) in de-ionized water and dried at 150^{o}C overnight in a hot air oven to remove any contaminants. The final polished α-alumina supports are shown in Figure 5.3.

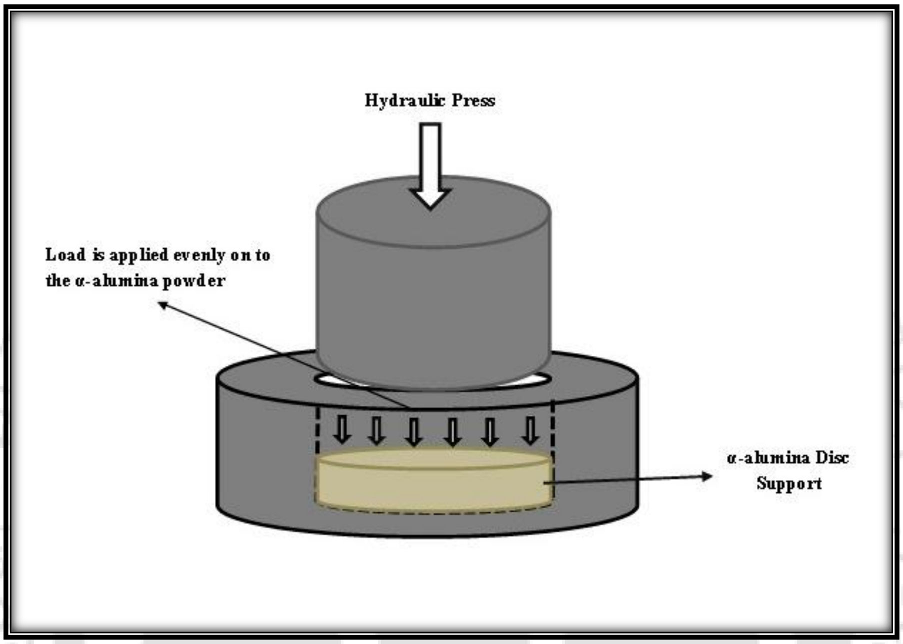

Figure 5.1 Stainless steel mold for support preparation

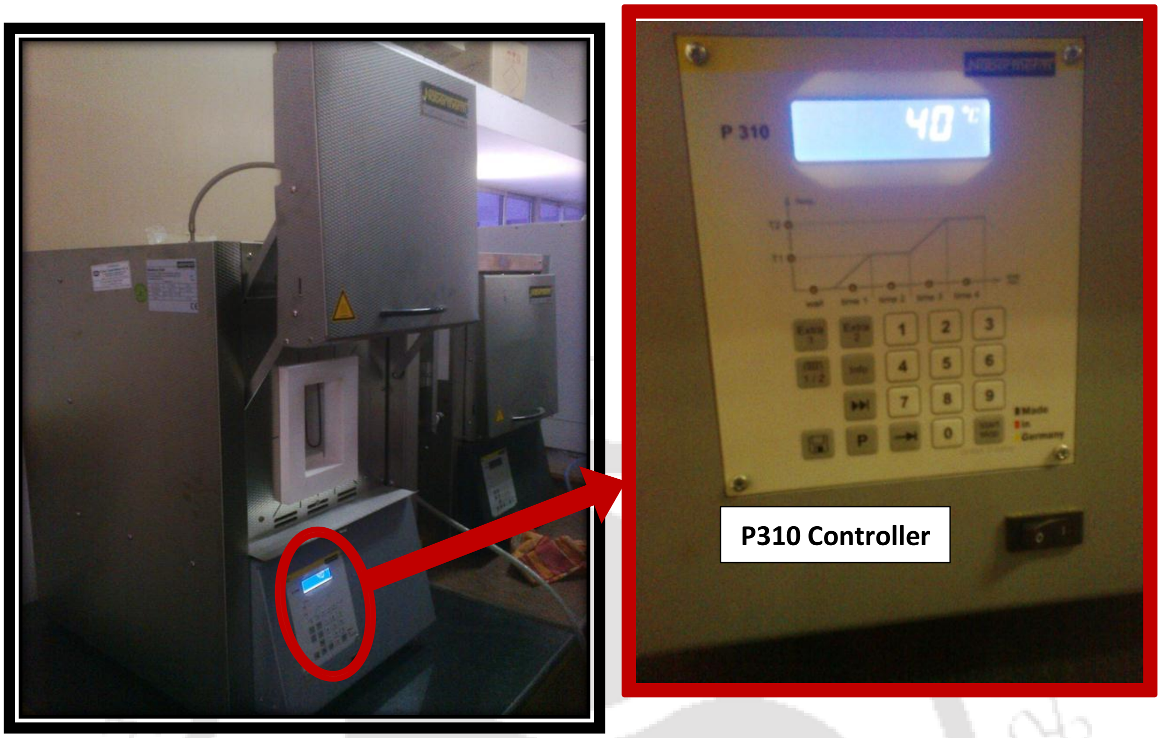

Figure 5.2 Programmable furnace with P310 controller

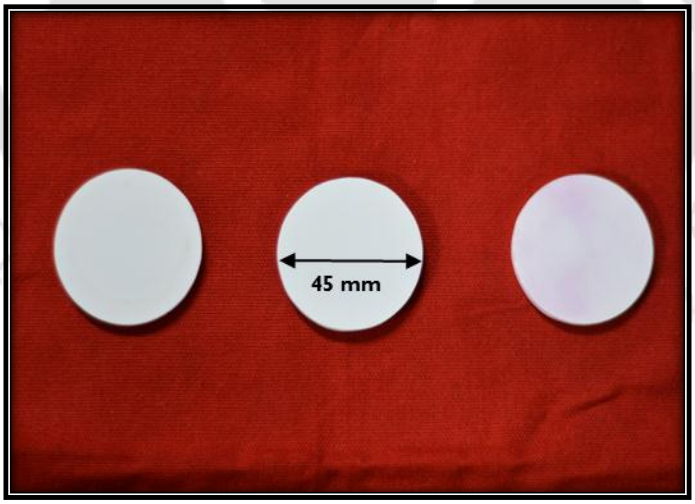

Figure 5.3 α-alumina membrane support after sintering and polishing

5.3.2. Characterization techniques

The crystallographic phases of the membrane supports were determined by (Bruke D8) advanced X-ray diffraction (XRD) measurement with Cu Kα radiation of wave length λ=1.54056 Å for 2θ angles between 30^o and 80^o. Flexural strength of the sintered membrane support discs were measured by 3 point flexural strength analysis using Universal tensile testing instrument (Deepak Polyplast) by ASTM D790 method. The particle size distribution of raw α-alumina powder was measured in a Delsa Nano particle analyser (BECKMAN COULTER).

Surface morphology and micro-structural analysis of the membrane supports were done using field emission electron microscope (FESEM) (Sigma- Zeiss). The estimation of average support pore size from FESEM micrographs was carried out using ImageJ software (Version 1.37). The average particle size and average surface pore size were determined [**17**] taking at least 50 pores visible from the FESEM image with maximum dimension of the pores and the particles. Since average particle size and average pore size values are critically dependent on the sampling procedure, five FESEM pictures were evaluated using the software. These micrographs were taken from the randomly selected sections of the membrane support. This ensured that the obtained pore size represented the existing porous texture of the membrane support. The area average pore diameter (d_s) from FESEM analysis of the membrane was evaluated by assuming cylindrical porous texture of the membrane as:

$$d_s = \left[\frac{\sum_{i=1}^{n} n_i\, d_i^2}{\sum_{i=1}^{n} n_i}\right]^{0.5} \tag{5.1}$$

where, *n* is the number of pores, d_i is the pore diameter (μm) of i^{th} pore.

Single gas permeation experiments through the supports were carried out by a custom made permeation module as shown in Figure 5.4. N_2 gas was used for the permeation measurements. Based on these gas permeation data, average pore radius (r_g) was estimated as follows [18]:

$$K = 2.133\frac{r_g\, v}{l_p}\frac{\varepsilon}{q^2} + 1.6\frac{r_g^2}{l\eta}\frac{\varepsilon}{q^2}P \tag{5.2}$$

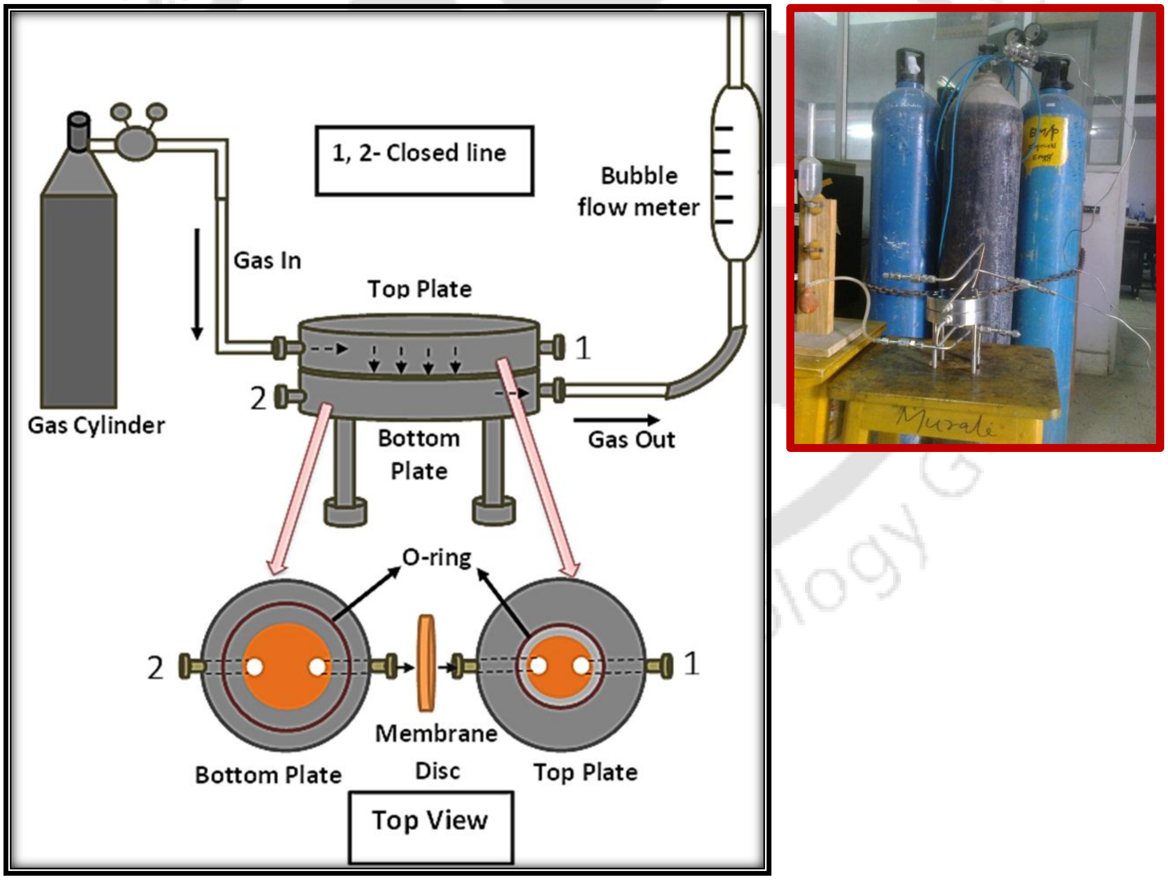

Figure 5.4 Schematic representation of single gas permeation set-up (picture in the right side)

where, v (m/s) is the molecular mean velocity of the gas, l_p(m) is the pore length, q is the tortuosity, η (Pa s) is the viscosity of gas, P is the average pressure on the membrane support, and K (m/s) is the effective permeability factor.

The effective permeability factor is obtained from the following equation:

$$K = \frac{P_2 Q}{S\Delta P} \tag{5.3}$$

where, P_2 is the membrane support pressure at permeate side, Q (m^3/s) is the volumetric flow rate, S (m^2) is the permeable area of the membrane support, and ΔP is the trans-membrane pressure drop.

Pore radius of the membrane support was calculated using the following equation:

$$r_g = 1.333 \frac{B}{C} v\eta \tag{5.4}$$

where, C and B are the slope and intercept, respectively, obtained from equation (5.2).

Porosity of the synthesized membrane support was obtained by Archimedes' principle using water as wetting liquid. The supports were first dried in an air oven at 110◦C for 6 h. The dry weight (W_1) of a support was measured. After that the supports were immersed in water in a vacuum desiccator for about 24 h at room temperature. The supports were then taken out from the water and the outer surface water was removed by using tissue paper. Then the weight of each wet membrane support (W_2) was measured. The porosity (ε) of each membrane support was determined by the following relation.

$$\varepsilon = \frac{(W_2 - W_1)}{V \times \rho_w} \tag{5.5}$$

where, ρ_w is the density of water. Apparent density of the membrane (ρ), membrane volume (v) and % shrinkage in diameter (S_h) were calculated from the following equations.

$$\rho = \frac{w}{v} \tag{5.6}$$

$$v = \frac{\pi {d_m}^2}{4} \times l_t \tag{5.7}$$

$$S_h = \frac{(d_i - d_f)}{d_i} \times 100 \tag{5.8}$$

where, w is the membrane mass after sintering, d_m is the diameter of the membrane after sintering and l_t is the thickness of the membrane before sintering, d_i is the initial diameter i.e. before sintering and d_f is the final diameter of the membrane i.e. diameter after sintering.

5.4. Results and Discussions

5.4.1. Raw α-alumina powder properties

The average particle size was obtained as 0.35 µm (Figure 5.5.). The obtained value was in agreement with the supplied data for particle size < 1 micron (99.9% Alfa Aesar, USA).

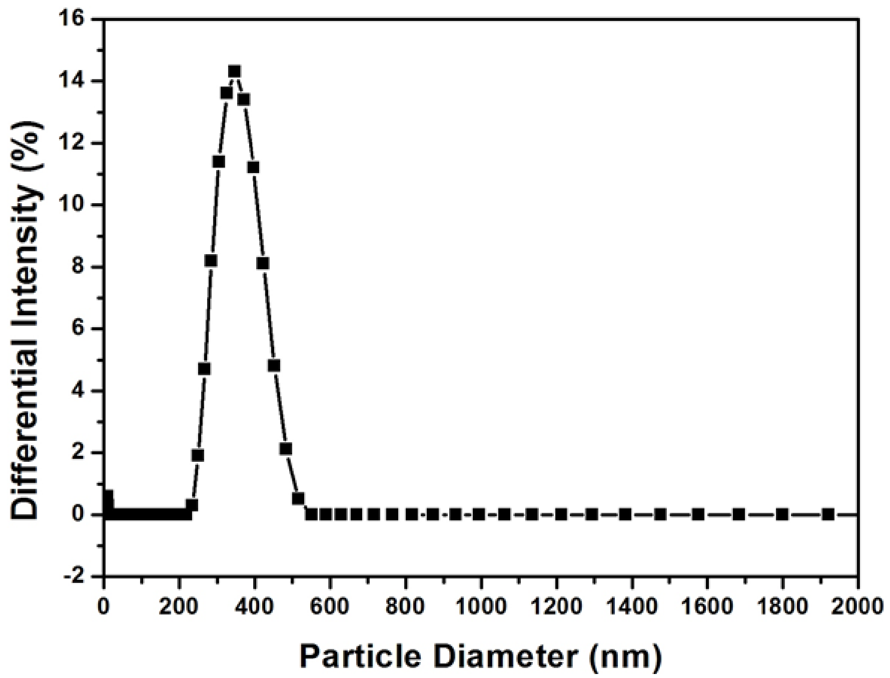

Figure 5.5 Particle size distribution of pure α- alumina powder

The XRD analysis of the raw α-alumina powder is shown in Figure 5.6. This figure depicts that the crystal pattern of α-alumina powder is rhombohedra. The surface area of the α-alumina powder was 6–8 m^2/g as reported by the supplier.

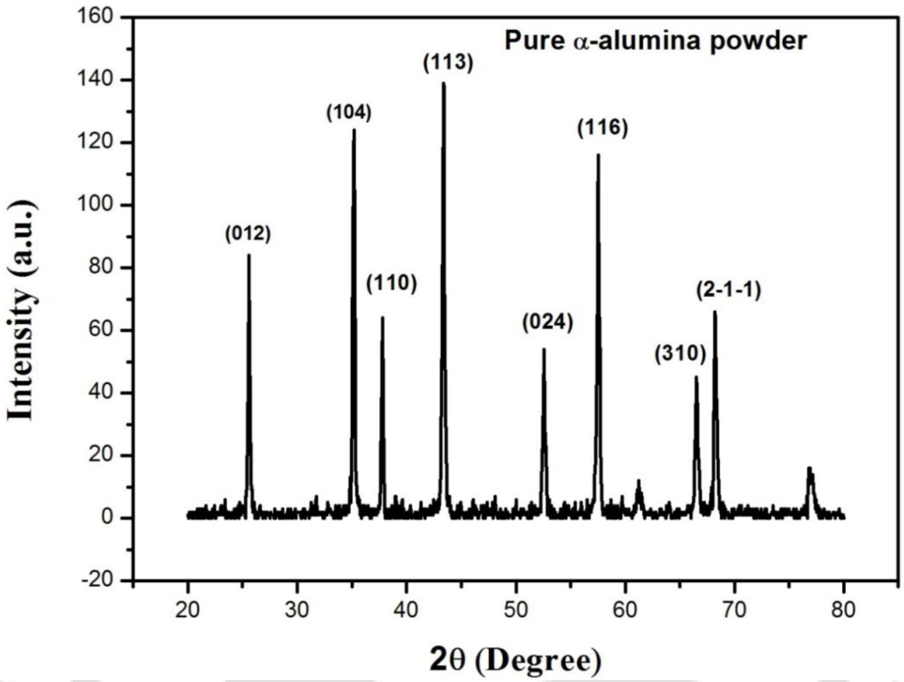

Figure 5.6 XRD patterns of raw α-Alumina powder

5.4.2. Support properties

5.4.2.1. *XRD analysis*

The XRD analyses of the synthesized supports are shown in Figures 5.7 and 5.8. These figures depict the change in peak intensity with change in the sintering temperature. It has been observed that with increase in temperature for a constant load (Figure 5.7.), the peak intensity increased, which represents higher crystallinity. This might be due to the fact that with increase in the sintering temperature the recrystallization and growth of the α-alumina microcrystals increase [**19**]. Changes in the peak intensity with different applying load for a constant temperature (Figure 5.8.) were not visible significantly. Figures 5.7 and 5.8 depict no additional peaks or missing peaks at different conditions.

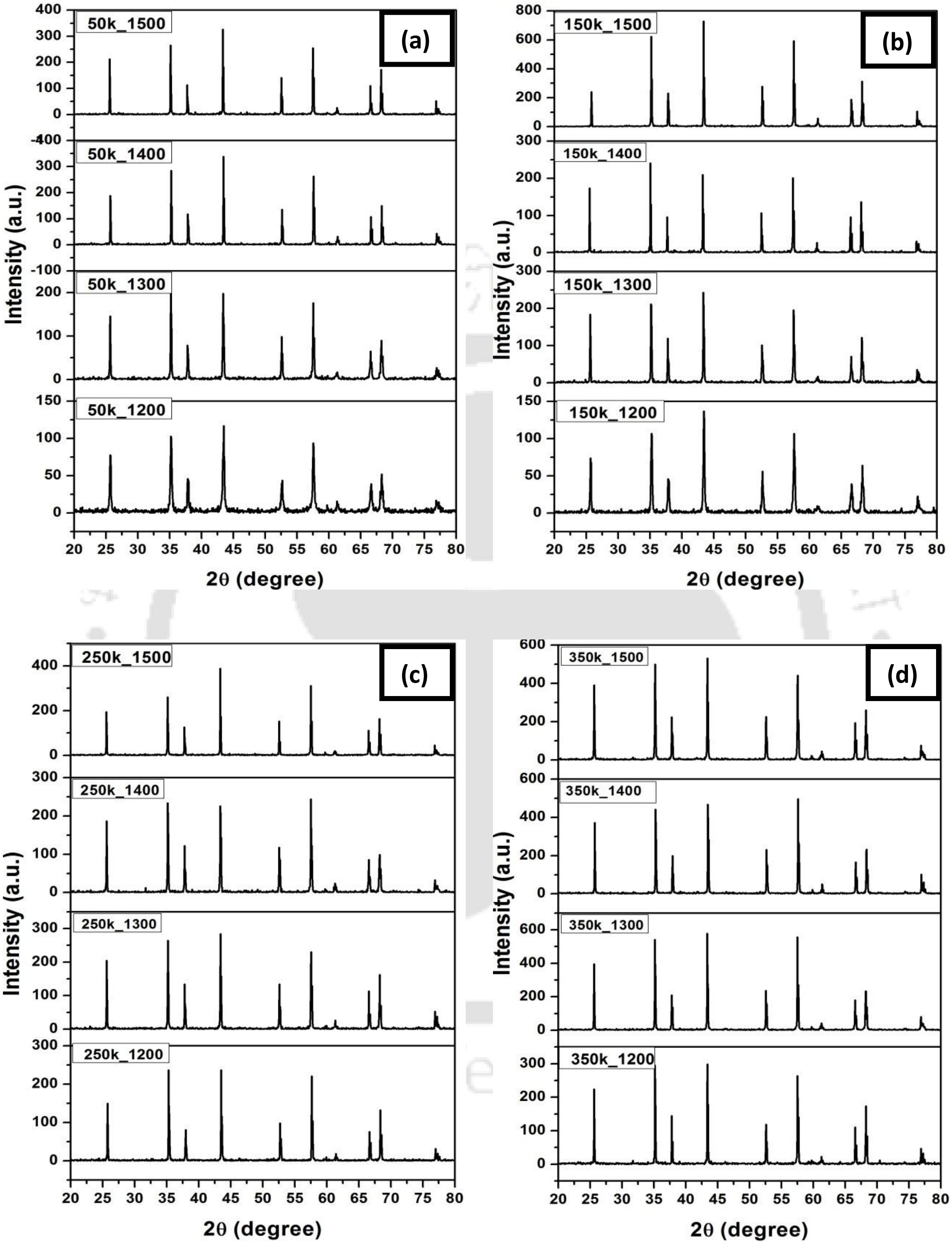

Figure 5.7 XRD patterns of the sintered α-Alumina membrane support at **(a)** 50kN, **(b)** 150 kN, **(c)** 250 kN and **(d)** 350 kN load at different temperatures.

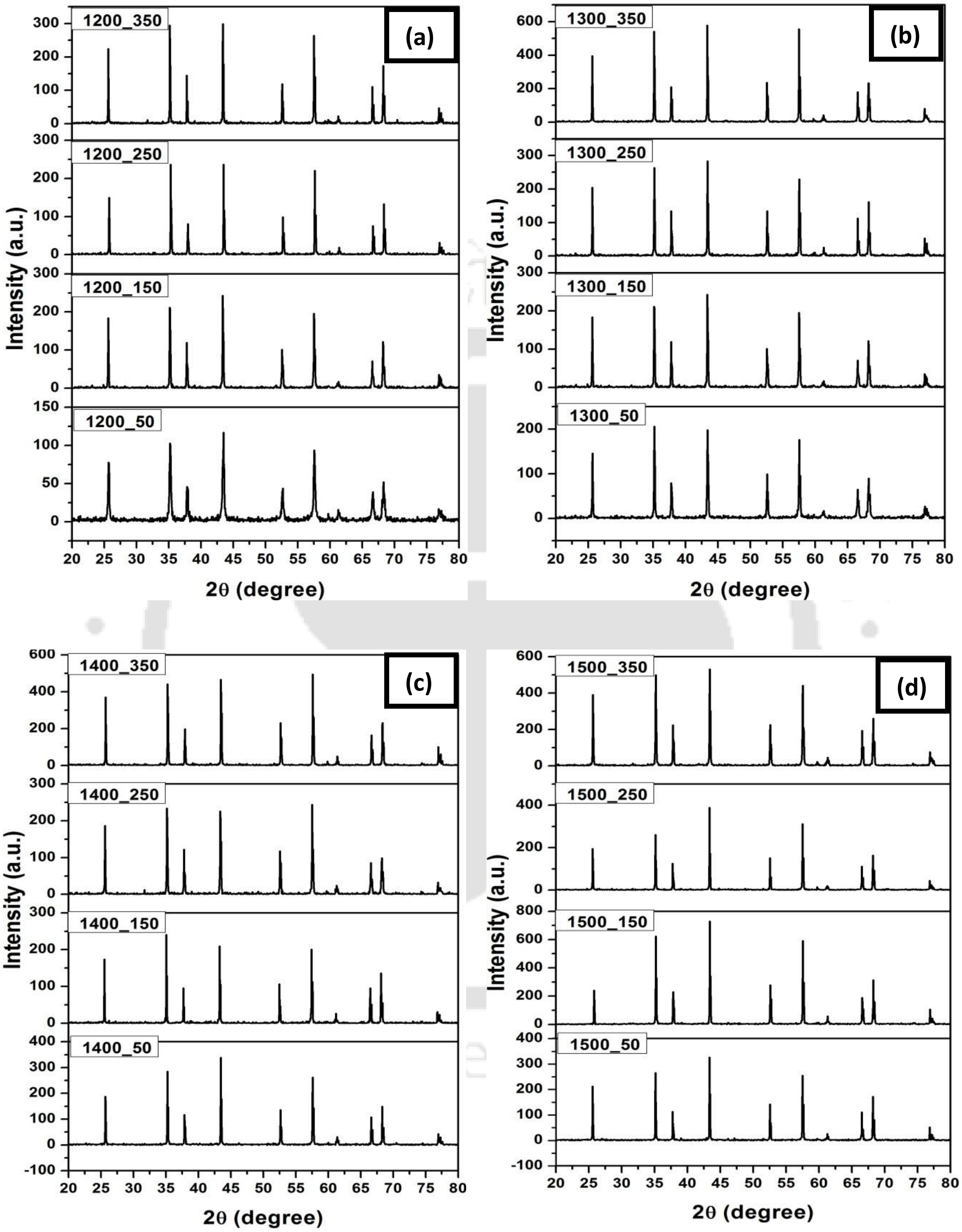

Figure 5.8 XRD patterns of the sintered α-Alumina membrane support at **(a)** 1200^{o}C, **(b)** 1300^{o}C, **(c)** 1400^{o}C and **(d)** 1500^{o}C at different load.

Therefore, no phase change was observed with change in sintering temperature as well as change in applied load.

5.4.2.2. *Flexural strength analysis*

Figure 5.9 shows that the flexural strength of the synthesized membrane supports gradually increases with temperature. The maximum flexural strength was obtained at 350 kN load and 1500 ^{o}C sintering temperature. The obtained flexural strength at that condition was close to 200 MPa, which is much higher compared to the value ~27 MPa obtained at 1200 ^{o}C sintering temperature and 50 kN compaction load. However, our results are comparable with values reported by Mottern et al. [**20**]. They also prepared α-alumina supports with a low temperature phosphate bonding technique using MAP (mono aluminium phosphate) and achieved the flexural strength of ~100 MPa. Results shown in Figure 5.9 depict that both the processing conditions (sintering temperature as well as compaction load) influence the flexural strength greatly. It was found that the compaction load played a significant role on the flexural strength. For a constant sintering temperature, the flexural strength increases with the compaction load. The possible reason behind high flexural strength is due to high density of the support disc. For a constant sintering temperature condition, and on applying higher compaction load, the neighbouring particles of the disc come closer and ultimately favour early and more sintering during the heat treatment. Therefore, for a constant sintering temperature, the grain growth increases with increase in compaction load and the flexural strength of the membrane disc increases sharply.

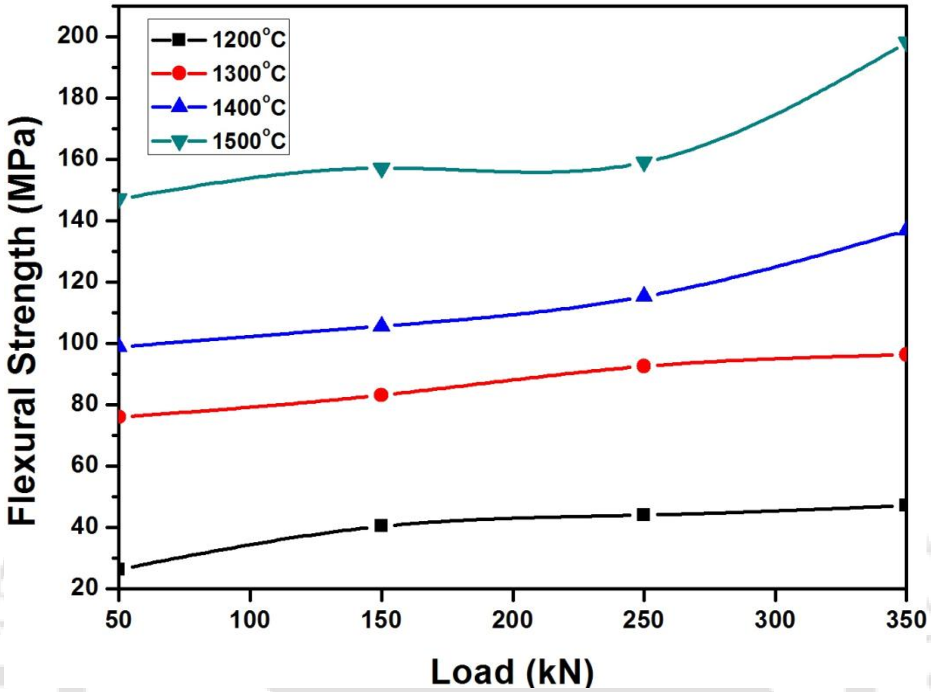

Figure 5.9 Flexural strength vs. compaction load for the supports synthesized at different sintering temperature.

5.4.2.3. *FESEM analysis*

The FESEM images of the membrane supports synthesized at 1200 ^{o}C at different applied load conditions are shown in Figure 5.10. It can be observed from Figure 5.10 that α-alumina particles underwent neck growth with adjacent particles. Decrease in pore sizes with increase in the sintering temperature was observed. This might be due to the rearrangement of small and regular primary particles. When the sintering temperature was increased to 1300 ^{o}C (Figure 5.11.), the particle sizes and sintering growth rate were almost same as that for1200 ^{o}C.

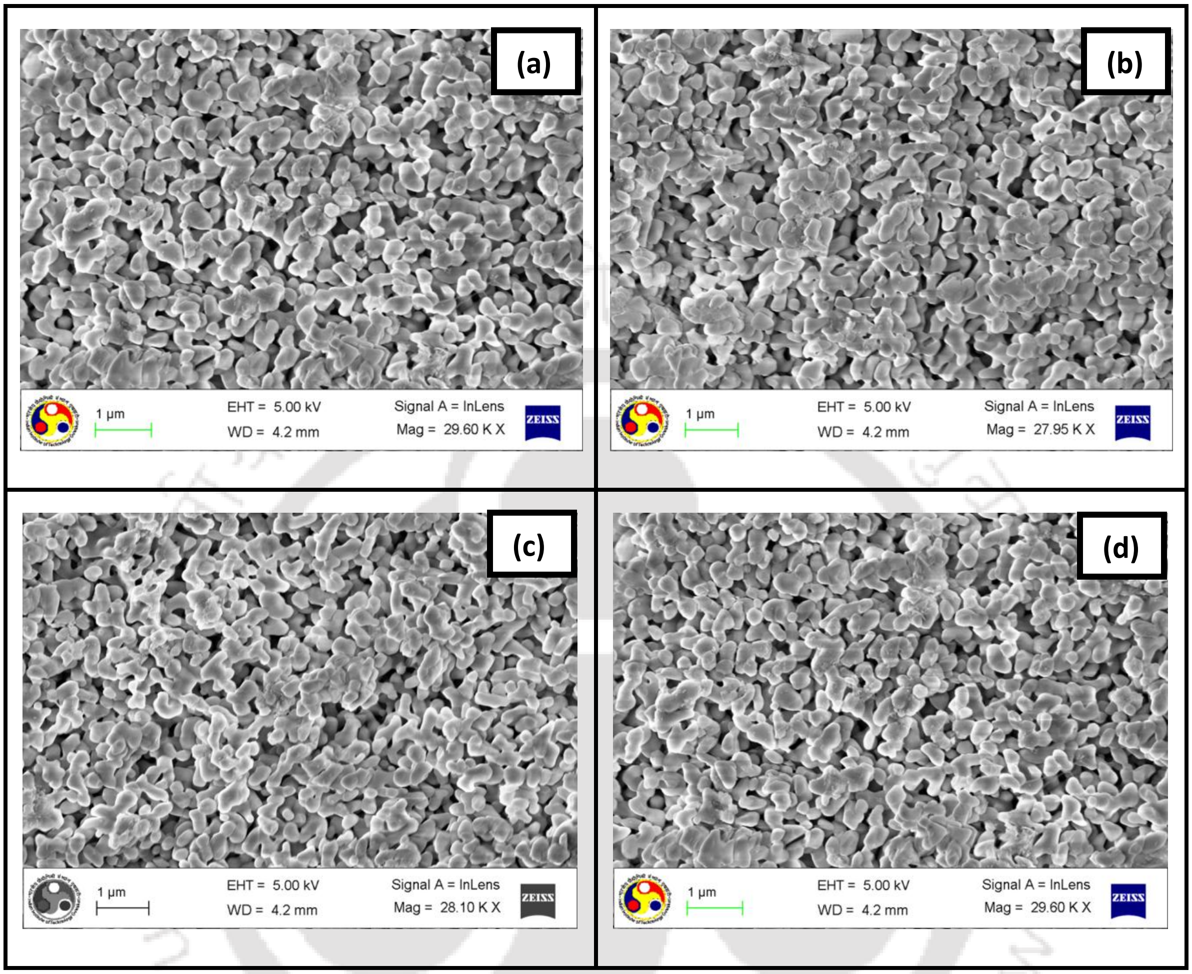

Figure 5.10 FESEM image of the α-Alumina disc membrane support synthesized at 1200^{o}C sintering temperature at **(a)** 50 kN, **(b)** 150 kN, **(c)** 250 kN and **(d)** 350 kN initial load.

However, as the sintering temperature increased to 1400 ^{o}C, a decrease in numbers of pores was observed due to significant increase in grain growth rate (Figure 5.12.). Finally, pores were almost eliminated at1500 ^{o}C (Figure 5.13.). As described before, at a particular sintering temperature the sintering starts earlier for 350 kN load compared to the other load conditions. Also, sintering with the higher rate of grain growth was observed until 1500 ^{o}C. As a result the minimum number of pores and the largest average particle sizes were obtained at 1500 ^{o}C and 350 kN load. Particle sizes and pore sizes (Table 5.1) at different conditions show that supports having lower pore sizes can be obtained at a lower sintering temperature if we apply higher compaction load. The volumetric diffusion and grain boundary diffusion is believed to be the possible sintering mechanism [**21-22**].

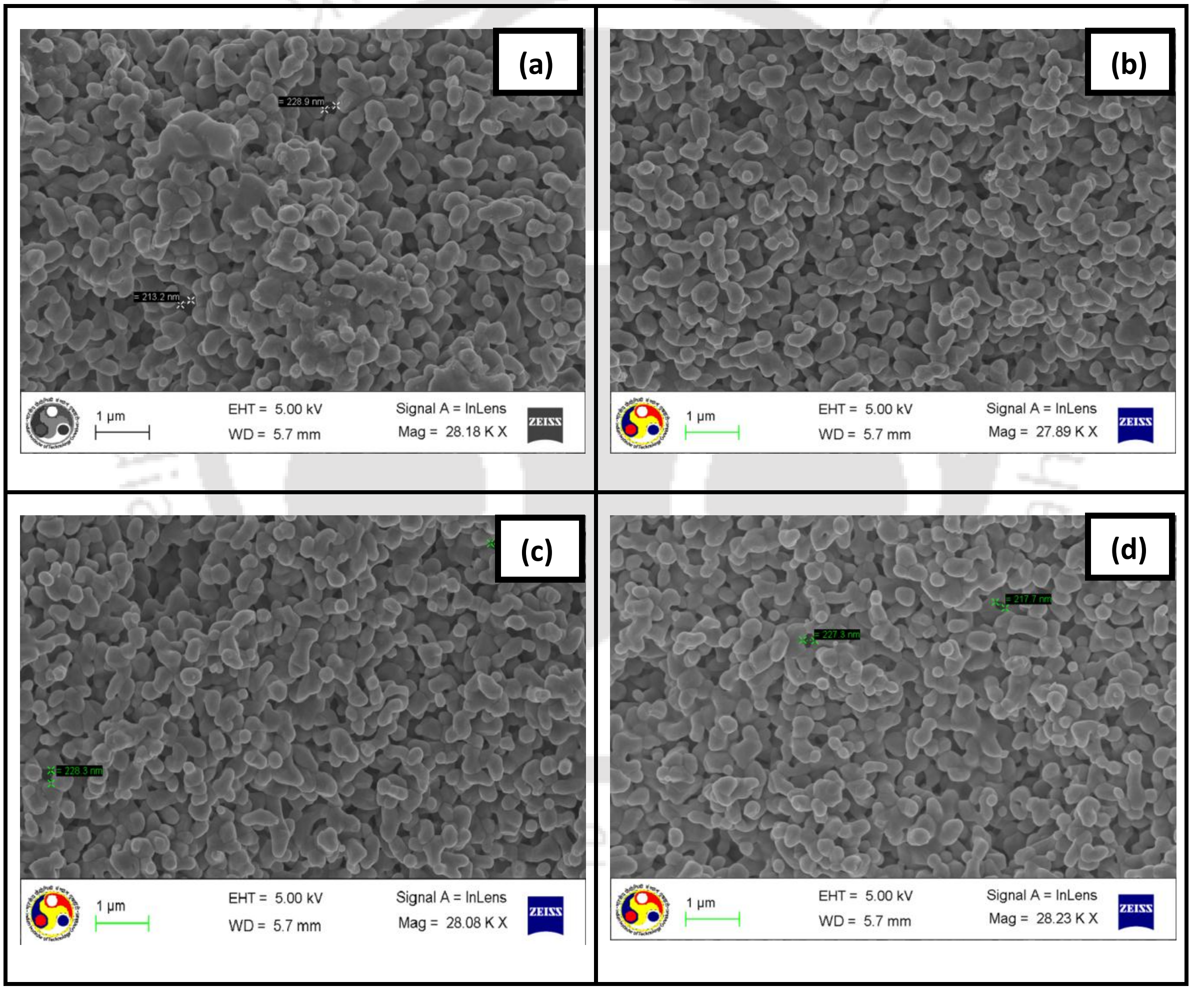

Figure 5.11 FESEM image of the α-Alumina disc membrane support synthesized at 1300^{o}C sintering temperature at **(a)** 50 kN, **(b)** 150 kN, **(c)** 250 kN and **(d)** 350 kN initial load.

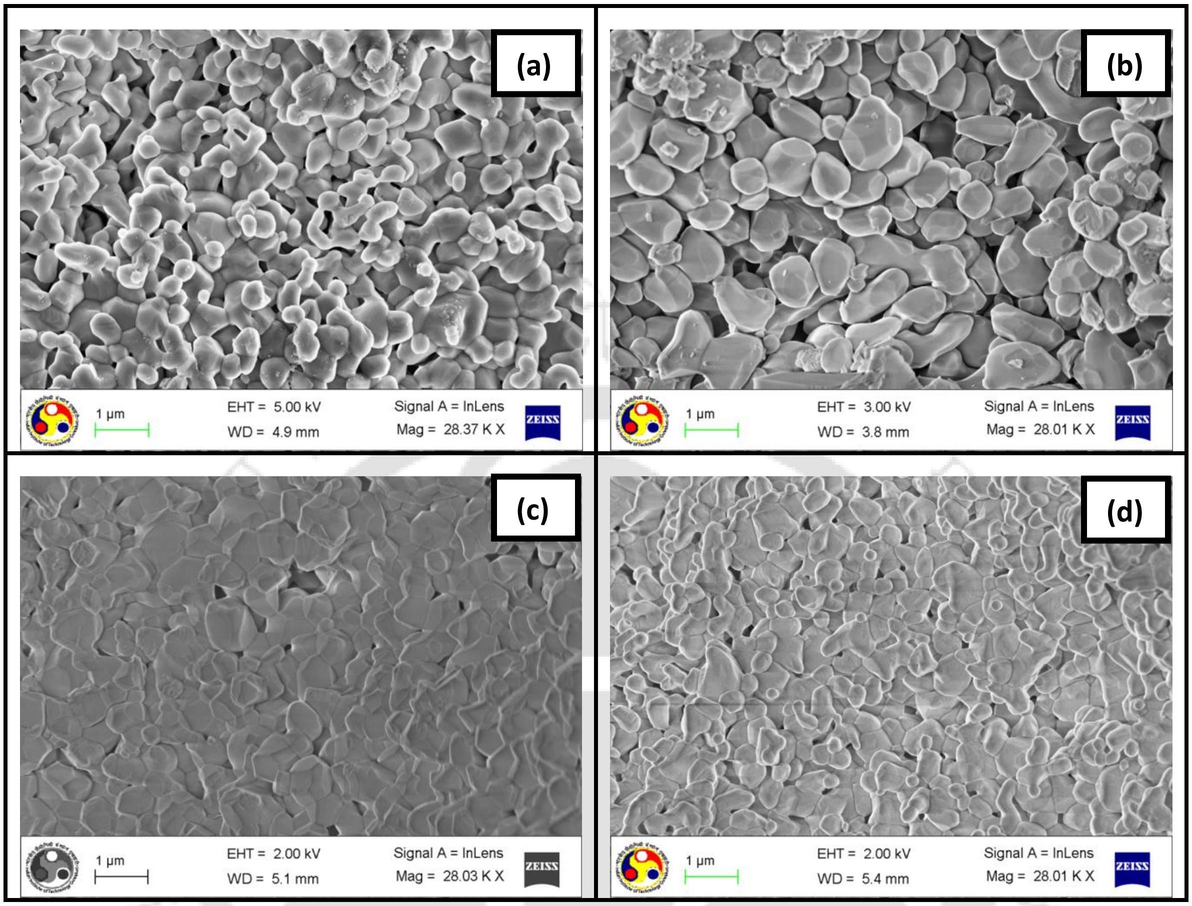

Figure 5.12 FESEM image of the α-Alumina disc membrane support synthesized at 1400°Csinteringtemperature at **(a)** 50 kN, **(b)** 150 kN, **(c)** 250 kN and **(d)** 350 kN initial load.

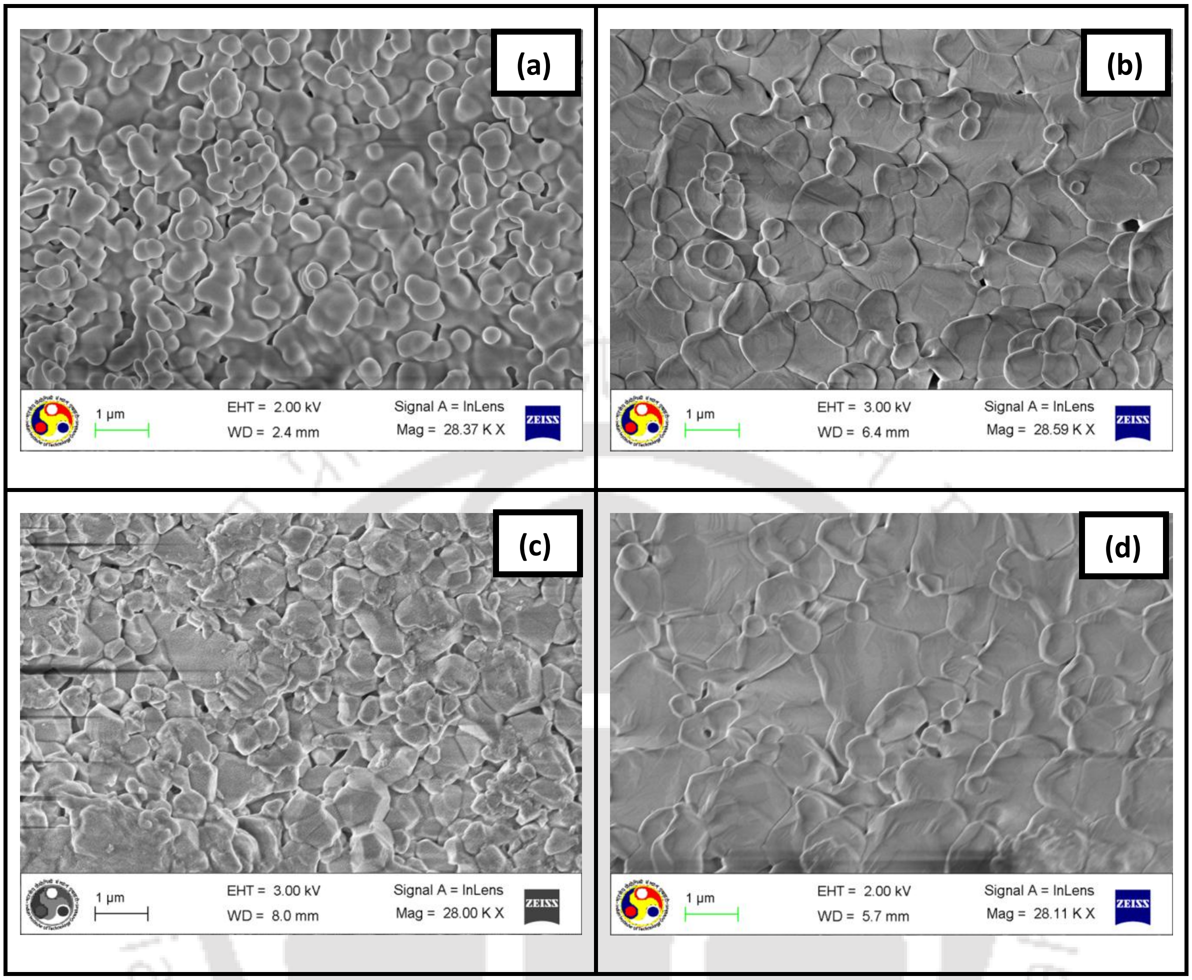

Figure 5.13 FESEM image of the α-Alumina disc membrane support synthesized at 1500^{o}C sintering temperature and **(a)** 50 kN, **(b)** 150 kN, **(c)** 250 kN and **(d)** 350 kN initial load.

5.4.2.4. *Nitrogen gas permeation analysis*

Pore size of the membrane support was also estimated by N_2 gas permeation analysis. Figure 4.14 presents the effective permeability factor vs. average pressure graphs for different membrane supports synthesized at different conditions (temperature and initial compaction load). The minimum pore sizes were obtained at higher sintering temperature and higher initial compaction load. The lowest value of effective permeability factor was found at1500 ^{o}C sintering temperature and 350 kN load. At this condition, average pore sizes obtained from N_2 gas permeation and FESEM analysis were 67 nm and 122 nm, respectively. The difference might be due to the fact that the FESEM analysis deals only with the surface pores (which is assumed to be cylindrical in shape) of the membrane support whereas gas permeation results provide the picture of inner pore channels (minimum passage, which is the neck of a funnel like shape, to pass through the gas) of the membrane support. The decrease in pore sizes with increase in sintering temperature and compaction load was observed from both N_2 gas permeation and FESEM analysis.

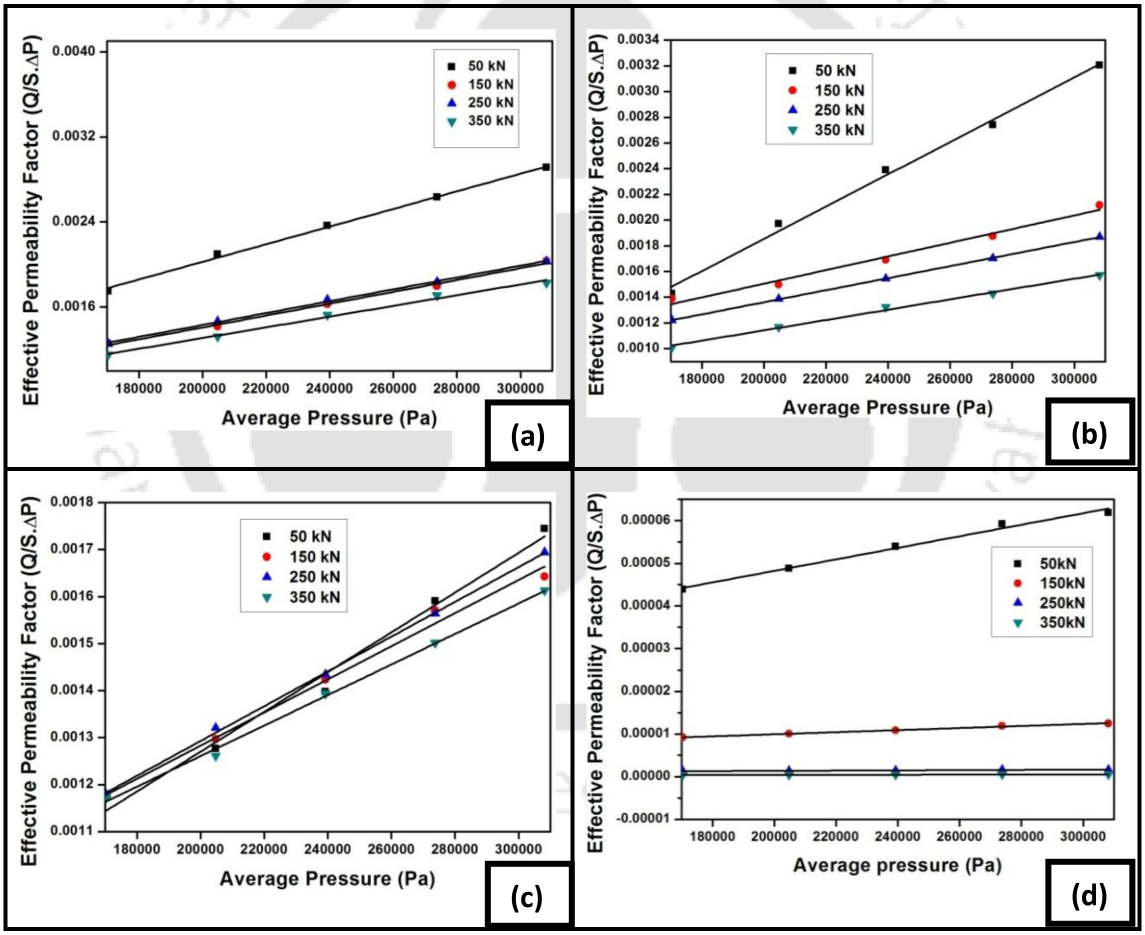

Figure 5.14 Effect of pressure on N_2 gas permeability for membrane supports synthesized at different sintering temperature **(a)** 1200^{o} C, **(b)** 1300^{o} C, **(c)** 1400^{o} C and **(d)** 1500^{o} C at different initial load.

Table 5.1
Average particle size and pore diameter of the sintered α-alumina membrane supports at different preparing conditions measured by ImageJ software from FESEM image and by N_2 gas permeation technique

Temperature (^oC)	Load (kN)	Average Particle Size by FESEM image (µm)	Average Pore size by FESEM image (µm)	Average Pore size by N_2 gas Permeation (µm)
1200	50	0.652	0.543	0.505
	150	0.661	0.485	0.505
	250	0.802	0.506	0.505
	350	0.772	0.497	0.420
1300	50	0.768	0.420	0.361
	150	0.826	0.421	0.316
	250	0.880	0.427	0.316
	350	1.135	0.418	0.337
1400	50	1.006	0.246	0.202
	150	1.064	0.238	0.168
	250	1.205	0.188	0.168
	350	1.212	0.142	0.168
1500	50	1.036	0.144	0.126
	150	1.306	0.134	0.101
	250	1.299	0.122	0.095
	350	1.599	0.122	0.067

5.4.2.5. *Porosity, density and shrinkage analysis*

Figure 5.15 shows the final density vs. load graph, which depicts that the density of the porous α-alumina support increases with higher compaction load. The increase in the density of the porous support was also observed with increase in temperature, which might be due to the sintering of the adjacent particle. So it is obvious that the higher the density, the lower the porosity or vice versa. Experimentally porosity of the membrane supports was determined. The results are shown in Figure 5.16, which satisfies the trend reported in Figure 5.15. Porosity of the membrane supports is decreased with higher sintering temperature (Figure 5.17) and also with higher initial load (Figure 5.16). Shrinkage in diameter greatly depends upon the sintering temperature. With increasing

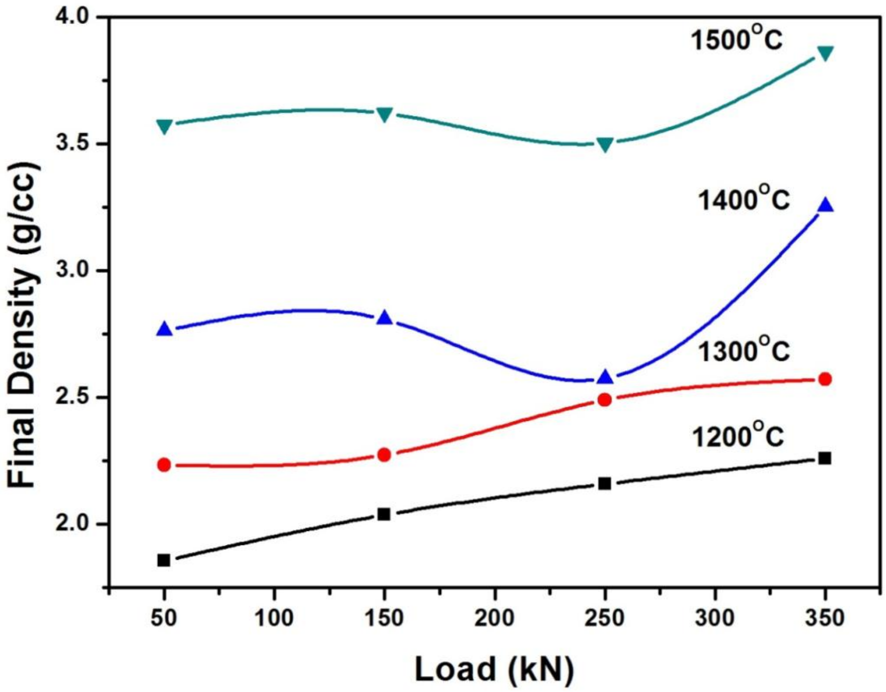

Figure 5.15 Final density of the sintered membrane support as a function of applied load at different temperatures: 1200°C, 1300°C, 1400°C and 1500°C.

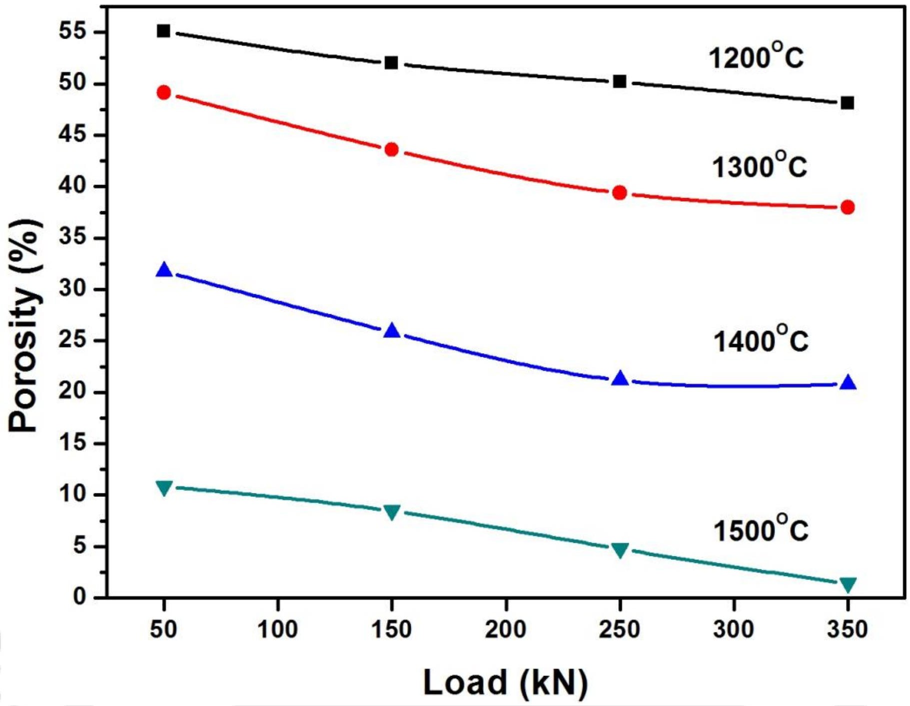

Figure 5.16 Porosity of the sintered membrane support as a function of applied load at different temperatures: 1200°C, 1300°C, 1400°C and 1500°C.

sintering temperature the shrinkage is more (Figure 5.18). Figure 5.18 shows the (%) shrinkage vs. compaction load at different temperature graphs. Significant change in the shrinkage of the diameter was not observed with the change in initial compaction load. However, at 1500 °C sintering temperature considerable change was observed between 50 kN load and 150 kN load. As discussed before, more compacted porous support can be obtained at higher compaction load. So the sintering starts earlier than the lower com-

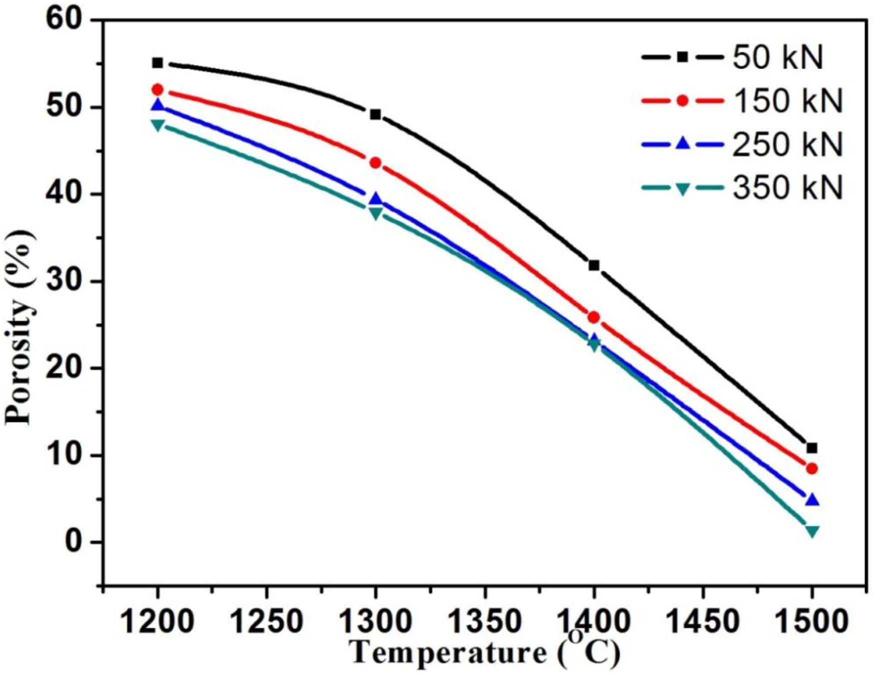

Figure 5.17 Porosity of the sintered membrane support as a function of temperature at different applied load: 50 kN, 150 kN, 250 kN and 350 kN.

-paction load condition at a particular sintering temperature. At 50 kN load condition the initial density for the porous membrane support was the least among other load conditions. So, the volume of the support was also maximum. When the final sintering occurred at1500 °C the change of the initial volume to the final volume was maximum due to the highest rate of volumetric diffusion compared to other load conditions which ultimately favoured maximum shrinkage.

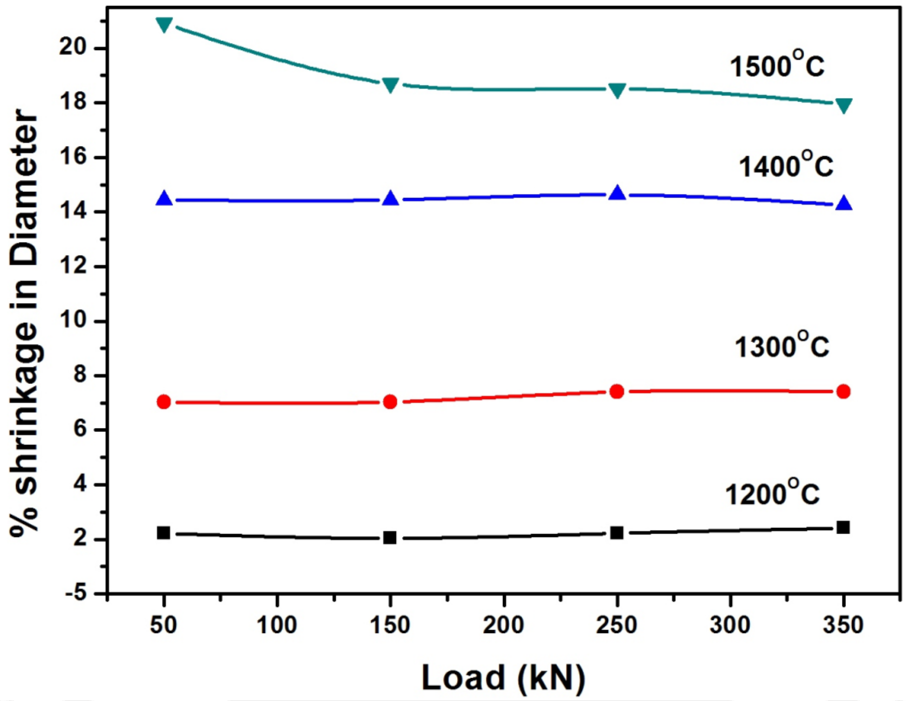

Figure 5.18 Percentage Shrinkage in diameter of the sintered membrane support as a function of applied load at different temperatures: 1200°C, 1300°C, 1400°C and 1500°C.

5.5. Conclusions

Membrane quality could be improved by varying the sintering temperature and initial compaction load. Both sintering temperature and initial compaction load played a significant role in α-alumina membrane support properties. Experimental studies showed that the prime variable of importance, which affected the key properties like pore size, porosity, flexural strength and shrinkage in diameter of the α-alumina membrane support, was the sintering temperature. However, it was observed that the key properties were marginally influenced by the compaction load. Results obtained from FESEM image analysis as well as N_2 permeation analysis for pore sizes showed quite similar trends.

References

[1] Shqau, K.; Mottern, M. L.; Yu, D.; Verweij, H. Preparation and properties of porous α-Al_2O_3 membrane supports, *J. Am. Ceram. Soc.* **2006,** *89(6)*, 790-1794.

[2] Sakamoto, Y.; Nagata, K.; Yogo, K.; Yamada, K. Preparation and CO_2 separation properties of amine-modified mesoporous silica membranes, *Micropor. Mesopor. Mater.* **2007,** *101*, 303-311.

[3] Guliants, V. V.; Carreon, M. A.; Lin, Y. S. Ordered mesoporous and macroporous inorganic films and membranes, *J. Membr.Sci.* **2004,** *235*, 53-72.

[4] Kumar, P.; Ida, J.; Kim, S.; Guliants, V. V.; Lin, J. Y. S. Ordered mesoporous membranes: Effects of support and surfactant removal conditions on membrane quality, *J. Membr. Sci.* **2006,** *279*, 539-547.

[5] Ostwal, M.; Pal Singh, R.; Dec, S. F.; Lusk, M. T.; Way, J. D. 3-aminopropyltriethoxysilane functionalized inorganic membranes for high temperature CO_2/N_2 separation, *J. Membr. Sci.* **2011,** *369*, 139-147.

[6] Li, S.; Carreon, M. A.; Zhang, Y.; Funke, H. H.; Noble, R. D.; Falconer, J. L. Scale-up of SAPO-34 membranes for CO_2/CH_4 separation, *J. Membr. Sci.* **2010,** *352*, 7-13.

[7] Chinelatto, A. S. A.; Tomasi, R. Influence of processing atmosphere on the microstructural evolution of submicron alumina powder during sintering, *Ceram. Int.* **2009,** *35*, 2915-2920.

[8] Hillman, S. H.; German, R. M. Constant heating rate analysis of simultaneous sintering mechanics in alumina, *J. Mater. Sci.* **1992,** *27*, 2641-2648.

[9] Page, R. A.; Pan, Y. M. Microstructure evolution during sintering, *Mater. Res. Soc. Symp. Proc.***1992,** *249,* 449.

[10] Fang, T. T.; Palmour III, H. Useful extensions of the statistical theory of sintering, *Ceram. Inter.* **1989,** *15,* 329-335.

[11] Lin, Y. S.; de Vries, K. J.; Burggraaf, A. J. Thermal stability and its improvement of the alumina membrane top layers prepared by sol-gel methods, *J. Mater. Sci.* **1991,** *26,* 715-720.

[12] Levanen, E.; Kolari, M.; Mantyla, T. Preparation of sprayed alumina microfiltration membranes, *The symposium of the ICIM'3, Worcestor,* **1994,** pp. 549-552.

[13] Lim, L. C.; Wong, P. M.; Jan, M. Microstructural evolution during sintering of near Monosized agglomerate-free submicron alumina powder compacts, *Acta. Mater.* **2000,** *48,* 2263-2275.

[14] Johnson, W. C.; Coble, R. L. A Test of the Second-Phase and Impurity-Segregation Models for MgO-Enhanced Densification of Sintered Alumina, *J. Am. Ceram. Soc.* **1978,** *61,* 110-114.

[15] Eskandari, A.; Aminzare, M.; Hesabi, Z. R.; Aboutalebi, S. H.; Sadrnezhaad, S. K. Effect of high energy ball milling on compressibility and sintering behaviour of alumina nanoparticles, *Ceram. Int.* **2012,** *38,* 2627-2632.

[16] Silva, L. L.O.; Vasconcelos, D. C. L.; Nunes, E. H.M.; Caldeira, L.; Costa, V. C.; Musse, A. P.; Hatimondi, S. A.; Nascimento, J. F.; Grava, W.; Vasconcelos, W. L. Processing, structural characterization and performance of alumina supports used in ceramic membranes, *Ceram. Int.* **2012,** *38,* 1943-1949.

[17] Pugazhenthi, G.; Kumar, A. Enzyme membrane reactor for hydrolysis of olive oil using lipase immobilized on modified PMMA composite membrane, *J. Membr. Sci.* **2004,** *228,* 187-197.

[18] Marchese, J.; Pagliero, C. L. Characterization of asymmetric poly sulphone membranes for gas separation, *Sep. Purif. Technol.* **1991,** *5*, 215-221.

[19] Coelho, A. C. V.; Santos, H. S.; Kiyohara, P. K.; Marcos, K. N. P.; Santos, P. S. Surface area, Crystal morphology and Characterization of Transition Alumina Powders from a new Gibbsite Precursor, *Mater. Res.* **2007,** *10(2),* 183-189.

[20] Mottern, M. L.; Chiu, W. V.; Warchol, Z. T.; Shqau, K.; Verweij, H. High-performance membrane supports: A colloidal approach to the consolidation of coarse particles, *Int. J. Hydrogen. Energy*. **2008,** *33,* 3903-3914.

[21] German, R.M. Sintering, Theory and Practice, *John Wiley & Sons, New York,* **1996.**

[22] Falamaki, C.; Afarani, M. S.; Aghaie, A. Initial sintering stage pore growth mechanism applied to the manufacture of ceramic membrane supports, *J. Eur. Ceram. Soc.* **2004,** *24,* 2285-2292.

Chapter 6

ORDERED MESOPOROUS SILICA MEMBRANE SYNTHESIS AND CHARACTERIZATION ON DIFFERENT SUPPORT

In this chapter, ordered mesoporous silica membrane are synthesized by sol-gel technology using spin coating method on different types of α-alumina supports of different pore sizes. The dependencies on the support quality for synthesizing ordered mesoporous silica membrane by spin coating method are studied. Detailed characterization study is performed to evaluate the formation of ordered mesoporous silica membrane onto the different supports. Also, single gas permeation through the synthesized membranes using N_2*, Ar, He and* CO_2 *gases are performed to know their efficiency and the mechanism of gas transport. In addition, mixed gas permeation (20%* CO_2 *and 80%* N_2*) studies are carried out using amino functionalized mesoporous silica membrane. This part of work has been published in* ***Microporous and Mesoporous Materials*** *210 (2015) 10-19.*

6.1. Introduction

Synthesising good quality ordered mesoporous silica membranes with controlled physical and chemical properties and also controlling the interface between various layers in multi-layered structures are very important. Simpler ways to synthesize mesoporous silica films by spin-coating [**1-2**] and dip coating [**3-4**] methods have been reported. Solvent-evaporation techniques have been utilized for the coating on glass supports [**1-2**] and on silicon wafers [**3-4**]. Various research groups have reported about the synthesis of mesoporous silica (MCM-48) membranes by sol–gel deposition on alumina supports [**5-6**]. However, the MCM-48 structure experiences ~20% contraction of the silica framework at (300–400) ^{o}C, during the surfactant decomposition [**7-10**]. Such large lattice contraction is expected to result in significant mechanical stresses in the MCM-48 membranes and the formation of macroscopic defects in the MCM-48 membrane layer, such as large cracks. Depending on the pore size of the support, the crack in the membrane might vary. The large pore sized supports can also result into penetration of the membrane material inside the pores of the support [**11-12**]. Hence, the quality of the support is one of the important factors in synthesizing good quality silica membrane. Kumar et al. [**13**] synthesized MCM-48 membrane on different types of support for CO_2 separation by hydrothermal method. They reported that the membrane quality depends upon the pore size of the support. A good quality support of having smooth surface as well as narrow surface pore size are necessary for the formation of thin ordered mesoporous silica membrane by spin coating method. Ordered mesoporous materials, as discussed in Chapter 3, are synthesized by the surfactant-templated self-assembly method [**14**]. Here, the ordered mesoporous silica membrane which is prepared by Evaporation induced self-assembly (EISA) method for more economical than the hydrothermal method. This chapter deals with synthesis, characterization and permeation studies for different gases. Finally, the separation studies for CO_2/N_2 gas mixtures are investigated by amine-functionalized ordered mesoprorous silica membrane.

6.2. Materials

Poly (vinyl alcohol) (98-99 mol% hydrolyzed powder) was obtained from Loba Chemie Pvt. Ltd, Mumbai, India. α-Alumina powder (Alfa Aesar, 99.9% (metals basis), size<1 micron APS powder, SA 6-8 m^2/g) was procured from Alfa Aesar, USA. Tetraethyl orthosilicate (TEOS), anhydrous toluene (EMPARTA^R ACS) and HCl (35%) were purchased from MERCK, India. N-hexadecyltrimethyl ammonium bromide (CTAB) and 3- aminopropyltriethoxysilane (3-APS) were supplied by Sigma Aldrich. Ethyl alcohol (EMSURE R ACS, ISO, Reag. PhEur) was obtained from Merck Germany.

6.3. Experimental

6.3.1 Support synthesis

The synthesis procedure for α-alumina supports have been described in Chapter 4 (see section 4.3.1).

6.3.2 Membrane synthesis

The details of sol synthesis procedure are described in Chapter 4 (see section 4.3.1.2) [**15**]. A mixture of EtOH, TEOS and diluted HCl (0.056 M, pH = 1.67) was taken into a beaker and was stirred for 1 h at room temperature. Then a required amount of CTAB was added to the mixture at room temperature with continuous stirring to dissolve it completely. The final sol was stirred continuously for 24 h for aging. The final molar ratio of the silica sol was CTAB: TEOS: H_2O (HCl): EtOH = 0.1:1:0.28:22. Sufficient amount of silica sol was then taken from the beaker with the help of a micropipette and was added drop-wise onto the different α-Al_2O_3 supports for spin-coating (Figure 6.2).

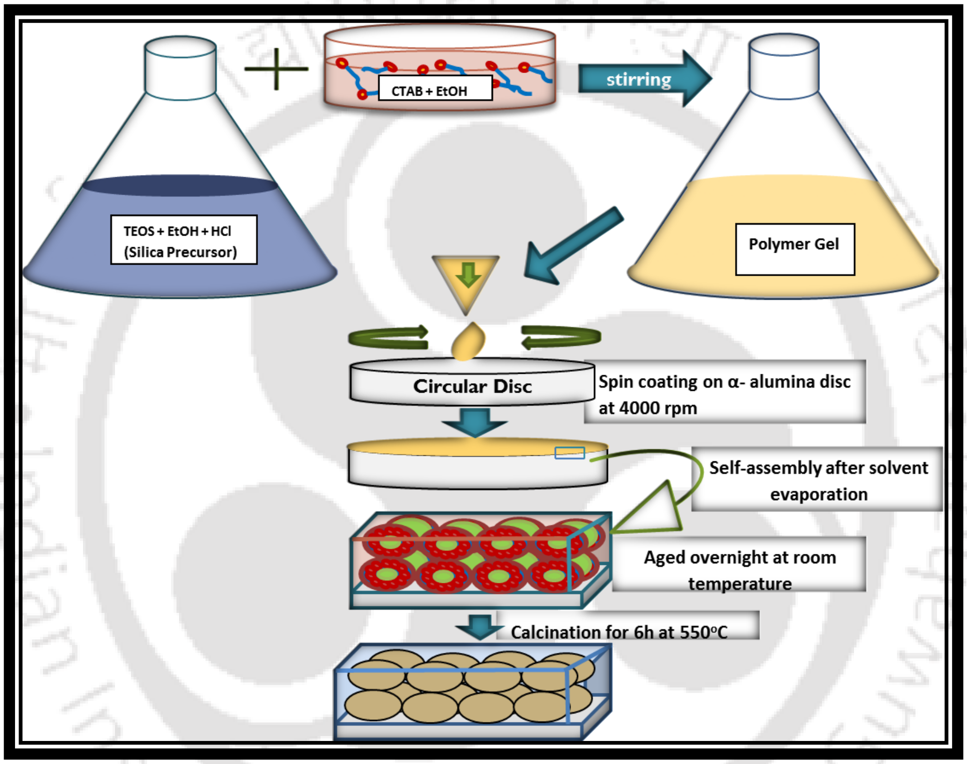

Figure 6.1 Synthesis procedure for OMS membrane by spin coating method

The coating was done at 4000 rpm for 180 sec. The coated membranes were kept overnight in a laminar flow chamber (Dlab Tech, Clean Bench). Finally, the spin coated membranes were calcined in the chamber furnace (Nabertherm, Germany) (Figure 5.2 shown in Chapter 5) at 550^{o}C for 6 h with the heating and cooling rate of 0.5 ^{o}C/min.

Figure 6.2 Spin coater Instrument for membrane coating

6.3.3. Functionalization of silica membrane by chemical grafting

The pores of the synthesized silica membrane were modified by 3-aminopropyltrimethoxysilirane (APS) to improve the CO_2 affinity of the pore walls.

Figure 6.3 Experimental set-up for amine functionalization for OMS membrane

MR2 membrane was taken for the modification. The method was followed as described as by Sakamoto et al. [**14**]. Calculated amount of 3-APS was dropped onto the ordered silica membrane MR2 which was previously taken into a beaker. The experiment was performed in Argon atmosphere. Before putting the silica membrane into the beaker, the membrane was dried at 120^{o}C in a vacuum oven for 24 h to remove the adsorbed water.

The modification was performed for 24 h at around 150^{o}C with a condenser. Finally the modified membrane was washed with anhydrous toluene (Merck, India), several times and was also dried at 60^{o}C for 24 h in a hot air oven.

6.3.4. Membrane Characterization

Structural analyies of the synthesized mesoporous silica membranes were conducted by (Bruke D8) advanced X-ray diffraction (XRD) measurement with Cu Kα radiation of wave length λ=1.54056 Å for 2θ angles between 2^o and 10^o at a scanning rate of 0.02° s^{-1} and a step size of 0.5 s. Surface morphology, cross-sectional view and micro-structural analysis of the membrane supports were done by using field emission scanning electron microscope (FESEM) (Sigma- Zeiss). The FESEM analysis was carried out to find the defect on the membrane support surface and also to know about the surface morphology of the membranes. The EDX (OXFORD Instruments, X-Max^N) analysis was carried out at different location of the support and the membrane layer to confirm the presence of different elements. FTIR spectrum analyses (SHIMADZU, IR Affinity 1, Japan) in powder mode were carried out to resolve the organic chemical groups of the synthesized active layers. FTIR spectra were recorded in the 4000−500 cm^{-1} wave number region using spectroscopic-quality KBr powder with 40 scans per sample and 4cm^{-1} resolution. The powder of the active membrane layer was scratched out by using a knife.

The steady-state single gas permeation experiments were carried out using pure N_2, Ar, He and CO_2 at room temperature (298 ±2K). The permeate side of the membrane was maintained at atmospheric pressure (14.7 psi), while four different pressures (138–345 kPa) were used on the feed side. A schematic representation of the steady-state permeation system is shown in Chapter 5 (Figure. 5.4).

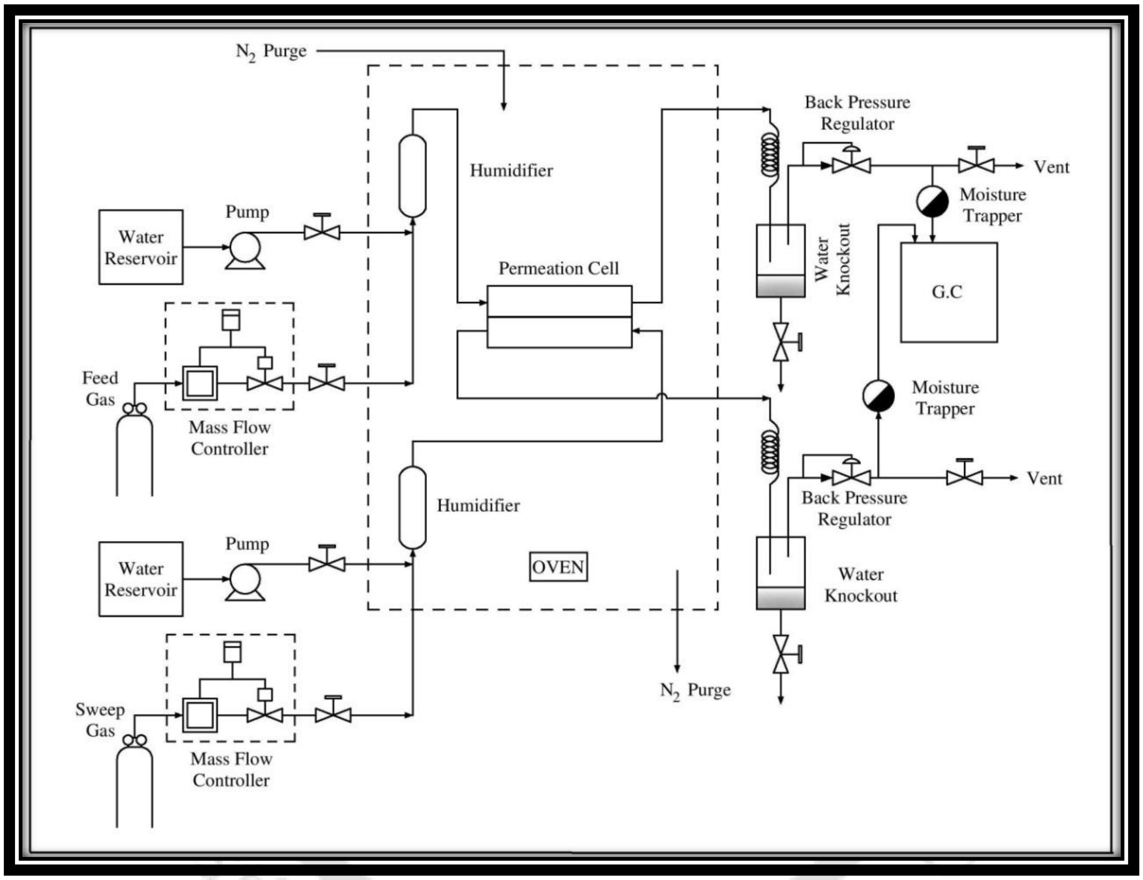

Figure 6.4 Schematic representation of gas-permeation set-up [**16**].

Transport properties of synthesized composite membrane with an active membrane area of 10.17 cm^2 were measured against different feed absolute pressure as mentioned above. For the pure gas experiments, the feed gas was pressurized and the permeate flow rate was measured using a bubble flow meter which in turn was used to calculate the permeance using Eq. (6.1).

$$Permeance\ (P_i) = \frac{Ni}{\Delta P_i} \tag{6.1}$$

where, P_i is the permeance of component i (in mol/(m^2 s Pa)) and N_i is molar flux of component i (in mol/(m^2 s)). ΔP_i is the pressure difference between feed and permeate side of component i.

The schematic of the mixed gas permeation measurement set-up is shown in Figure 6.4. The membrane was mounted in a stainless steel counter-current permeation module with an active membrane area of 10.17 cm^2. Transport properties of synthesized 3-APS modified ordered mesoporous silica membrane was measured against feed absolute pressure. The feed gas mixture contained 20% CO_2 and 80% N_2 on dry basis. Pure argon was used to control the feed side and permeate side gas flow rates. Both the feed and permeate side gas flow rates were kept at 40 cm^3/min. The pressure at feed side and permeate side of the membrane module was maintained by two different back-pressure regulators. The absolute feed pressure was varied from 148 kPa to 1013kPa and the absolute permeate pressure was maintained close to atmospheric pressure. Both the retentate and permeate streams leaving from the permeation cell were entered to the gas chromatograph (GC) for composition analysis. The compositions of both the retentate and permeate gas were then analyzed sequentially using Varian 450 gas chromatograph (Varian Inc., Palo Alto, CA) with one thermal conductivity detector (TCD). Helium was used as the GC carrier gas for TCD detector. The GC columns were used as CP7430 capillary columns (Agilent Technologies, Palo Alto, CA), which were the combination of two different capillary columns, one being the CP-Molsieve 5A and the other being CP-PoraBOND Q.

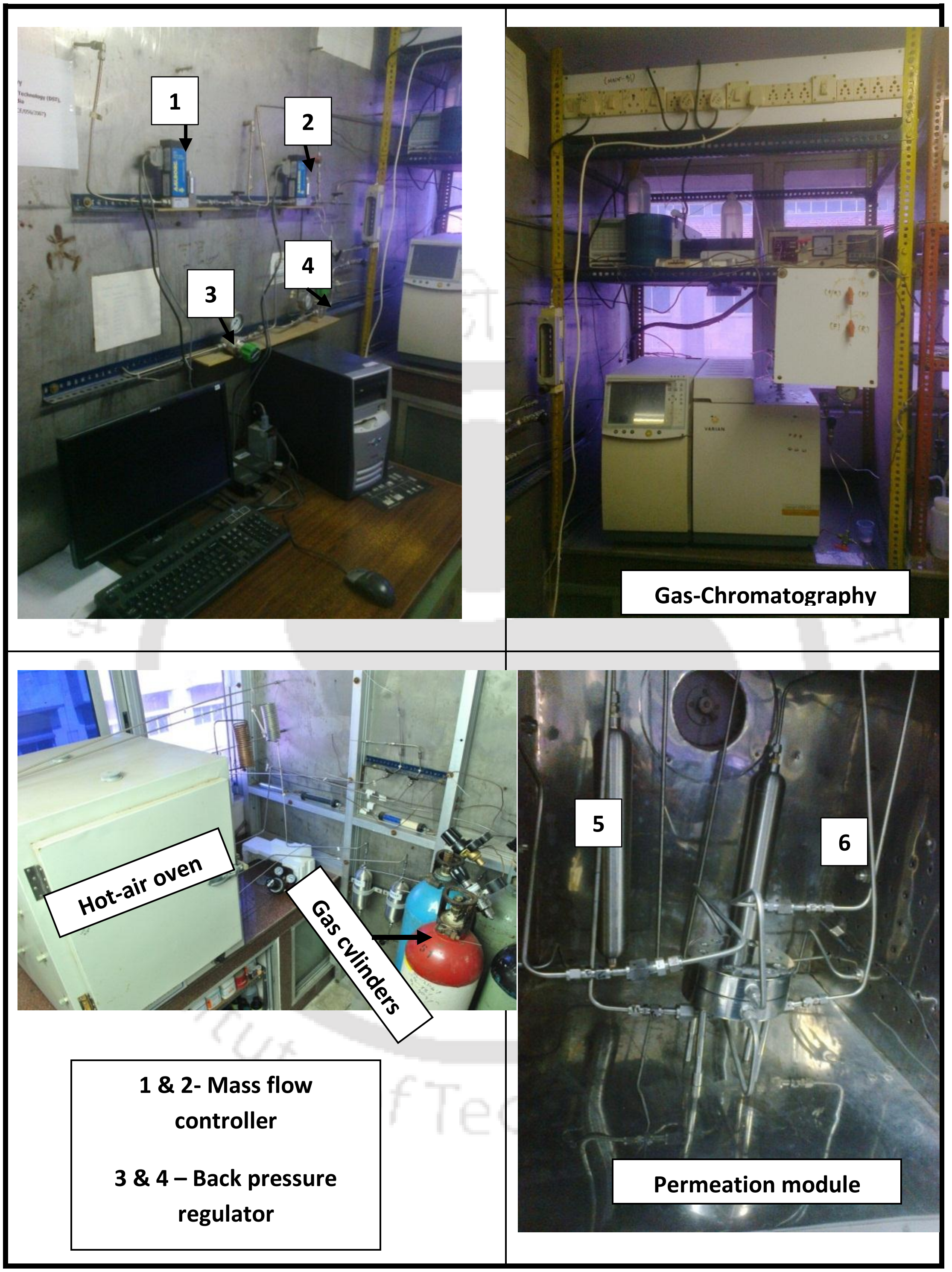

Figure 6.5 Gas permeation Experimental set-up

Each of the membrane permeation measurements were carried out for at least 24 h at a particular pressure and at a room temperature which allowed for the steady state permeation. All the presented gas permeation data are the average of three replicate measurements [**Appendix 2**]. The CO_2/N_2 selectivity was obtained from GC analysis. The CO_2/N_2 selectivity was defined as follows:

$$\alpha_{ij} = \frac{y_i/y_j}{x_i/x_j} \tag{6.2}$$

where, α_{ij} = selectivity of component *i* over component *j*, y_i and y_j are mole fractions of component *i* and *j* in the permeate stream and x_i and x_j are mole fractions of component *i* and *j* in retentate stream [**16**].

6.4. Results & discussions

6.4.1. X-ray diffraction (XRD) analysis

The XRD patterns of the silica membranes synthesized by spin coating on different α-alumina supports, having 3 different pore sizes denoted as MR1, MR2 and MR3 are shown in Figure 6.6. The pore sizes of the supports are ~0.3µm, 0.15µm and 0.09µm for MR1, MR2 and MR3, respectively. The layer deposited on MR1 α- alumina support did not reveal any strong diffraction peaks in the 2θ range of 2–10^o, however, the layer deposited on the other α-alumina supports which are denoted by MR2 and MR3, showed clear peaks around 3.5^o, as shown in Figure 6.6. The peak for (100) reflection appeared in MR2 and MR3 after coating, indicating the formation of the periodic ordered structure of the silica surfactant composite. However, the peak intensity has increased with decrease in pore size of the supports. The uncalcined membranes are denoted by MR1(U), MR2(U) and MR3(U) for the corresponding membranes. The XRD pattern for the membrane MR2 shows one strong (100) diffraction peak, at $2\theta = 3.5°$.The corresponding crystal plane spacing $d(100)$ for the different membranes were calculated by using the Bragg's formula $\lambda = 2d\sin\theta$. The XRD patterns were taken for the fully dried spin-coated membrane and after the calcination of the membranes.

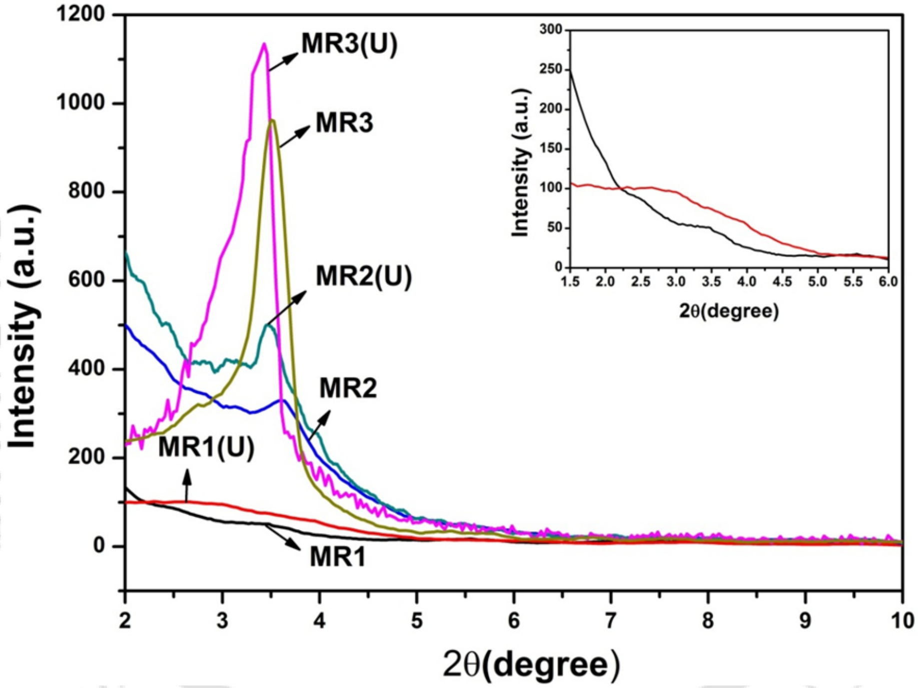

Figure 6.6 XRD diffraction patterns of the silica membranes synthesized on different supports before calcination and after calcination.

The $d(100)$ spacing values for the corresponding membranes before and after calcination are shown in Table 6.1. It can be observed from the Figure 6.6. that after calcination, the peaks shifted to higher angles. So the $d(100)$ spacing decreased after calcination. The $d(100)$ spacing reduced from 3.02 to 2.52 nm after calcination, for the membrane MR1 which corresponds to 16.64% contraction. This structural contract is attributed to the evaporation of residual solvent and the template removal. Due to the sufficient drying for the spin-coated membrane, this effect is less. But the shrinkage of structure mainly can be explained by the change in the connectivity of the SiO_4 network during calcination. Subsequent calcination causes the condensation of internal Si-OH group giving to a contraction of the structure. The contractions for the other two membranes were very less compared to membrane MR1. The possible reason behind higher contraction may be the larger thermal expansion ratio between the support and the membrane layer [**9**]. It was observed that the ordered mesoporous structure was retained for the membranes MR2 and MR3. It can also be observed from Figure 6.6 that the peak shape of each calcined product becomes less sharp with the increase in support pore size, indicating that the ordering degree decreases. It is evident however that for the membrane MR2, the (100) diffraction peak has been broadened to some extent, and for the membrane MR1 the peak corresponding to the (100) plane is hard to distinguish, indicating that the product contains large amount of non-hexagonal phase, and thus the (100) diffraction peak is heavily widened. The decrease in peak intensity and increase in peak width of the silica films indicates poor thermal stability of the structure which is due to the insufficient formation of silicate network in the as synthesized film [17]. At the time of spin coating, the silica sol comes into contact with the macroporous α-alumina support.

Table 6.1
'd'spacing value for the different membranes before and after the calcination

Membrane	d spacing (nm)		Size reduction (%)
	Uncalcined	Calcined	
MR1	**3.023**	**2.52**	**16.64**
MR2	**2.52**	**2.45**	**2.77**
MR3	**2.57**	**2.52**	**2.09**

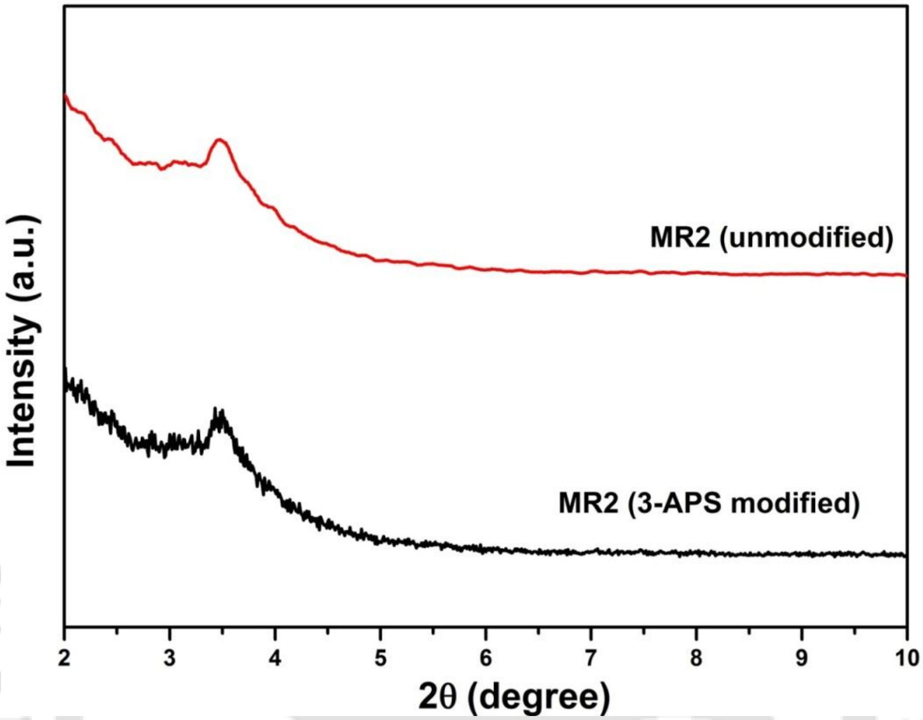

Figure 6.7 XRD diffraction patterns of the amine functionalized silica membrane (MR2) and unmodified membrane (MR2).

The α-alumina pores of ~0.3 μm diameter may exert a very large capillary suction on the sol liquid [**18**]. This suction is so high that it causes turbulence locally and any ordered miceller domains cannot be formed. Ultimately it results in non-ordered mesostructure silica film for MR1. The suction pressure, P_s, is evaluated as $2\gamma/r$, where γ and r are the surface tension of the sol and pore size of the α-alumina support, respectively. The suction force is calculated to be P_s × Area of the pore opening. The suction by the support may also enhance the drying rate of the silica film near the interface so drastically that the silica framework freezes before any self-organization has occurred. Due to the smaller size of the pores for the α-alumina supports for MR2 membranes, the suction force is lower than MR1 membranes. Initially the α-alumina capillaries may exert suction in the interface of the membrane surface and may form disordered structure but as soon as the capillary are filled by the silica sol, there will not be any suction pressure and the further growth of the silica structure can take place in the form of an ordered structure on top of the interface [**18**]. There may not be sufficient suction force for MR3 membrane that can prevent an ordered structure to form. The absence of the (110) reflection for the membranes MR2 and MR3 indicate that the (100) family of planes of the hexagonal unit cell is oriented parallel to the surface of the α-alumina substrate, which is consistent with the literature results [**1-2**]. The XRD peaks for the unmodified and 3-APS modified MR2 membrane is shown in Figure 6.7. However, no change in the peak position was found after amine modification, and the structure of mesoporous silica was retained.

6.4.2. Fourier transform infrared spectroscopy (FTIR) analysis

The sharp transmittance bands at 1100 cm^{-1} observed in all of the spectra are ascribed to the Si-O-Si framework. The peaks relative to Si-OH (960 cm^{-1}) and to Si-O-Si (1100–1000 cm^{-1}), means that the sol–gel matrix is not destroyed. The broad band observed at about 3000–3600 cm^{-1}, centred at 3375 cm^{-1}, and at 1634 cm^{-1}for the mesoporous silica membranes in Figure 6.8 is assigned to the surface silanol groups and adsorbed water molecule. This band is assigned to the hydrogen bonded silanol group combined with adsorbed molecular water at the external surface of the film as well as the internal defect sites due to poor connectivity of the (Si–O–Si) network in the interior of the film [**19-20**].

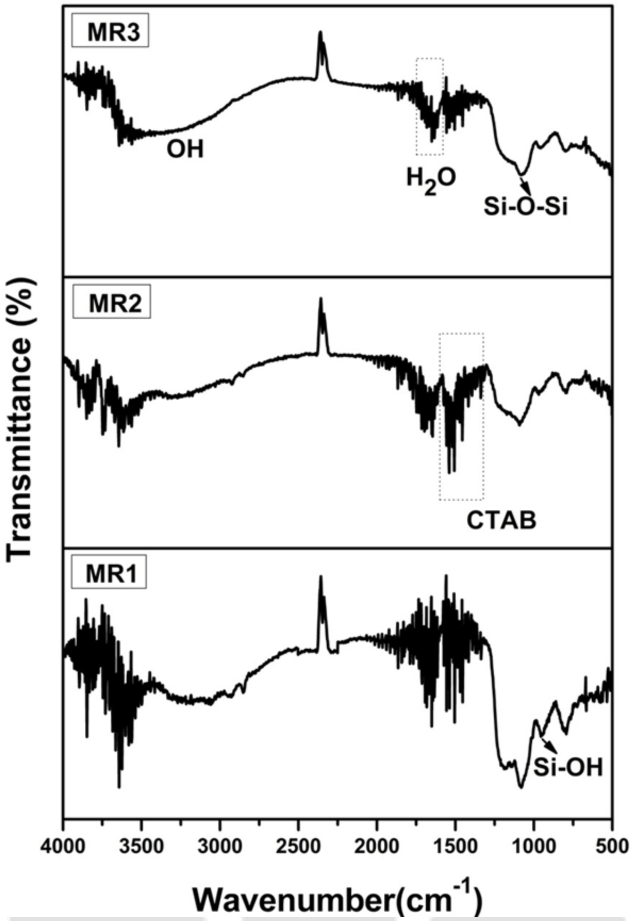

Figure 6.8 FTIR spectra of different silica membranes synthesized on different α-alumina supports.

A sharp peak at 3742 cm^{-1} for the membrane MR1 and MR2 are assigned as the hydrogen bonded silanol groups. So it was observed that H-bonded silanol groups are present more in case of MR1 and MR2 [**17, 19-20**]. The absence of the broad band in the spectra at 3500 cm^{-1} of the MR1 & MR2 samples shows that the concentration of the residual silanol group is extremely low. This is may be due to the high adsorption of water molecule in membranes MR1 and MR2 for which the free surface Si-OH groups are reduced. The presence of excess organics in the film as well as insufficient evacuation during measurements could be another possible reason. The transmittance peak band observed in the range of 3000–2800 cm^{-1} for mesostructured film for membranes MR1 is due to methyl groups still present in the film indicating the presence of the surfactant within the film [**19-20**].

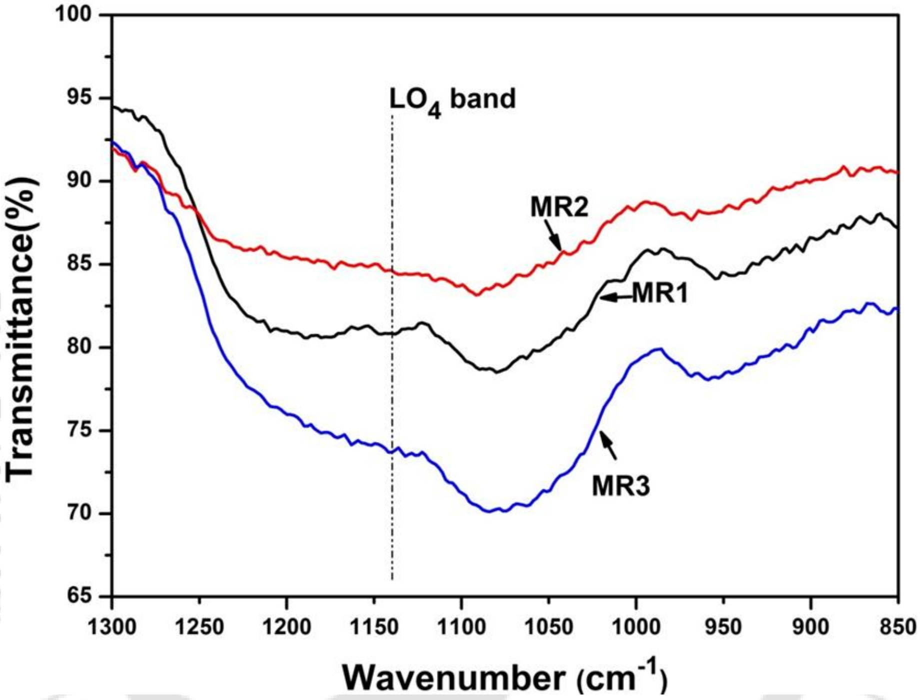

Figure 6.9 FTIR spectra in the range 1300-850 cm^{-1} of different silica membranes synthesized on different α- alumina supports.

The membranes MR1 & MR2, however, have peaks in the 1700–1000 cm^{-1} regions, due to water and residual CTAB fragments. The presence of CTAB fragments are also confirmed by the EDX analysis of the membrane layer which is shown in Figure 6.12. The presence of residual CTAB within the films may be due to the insufficient polymerization. The peak in the range of 650–1300 cm^{-1} for silicate (Si–O) stretches signifies the silicate network in the films. The intense broad shoulder around 1200 cm^{-1}, accompanying the (Si–O–Si) stretching mode is attributed to a broadened signature of the longitudinal optical (LO) component of the transverse optical (TO) antisymmetric stretching, or a mixed LO–TO mode with a dominant LO character [**20-22**]. In the mesoporous film the LO$_4$ (longitudinal optical) mode is detected around 1130 cm^{-1}[**23**] which is shown in Figure 5.9. The evolution with support pore size of the LO$_4$ mode shows a decrease in intensity when the support pore size decreases, suggesting a change to a more ordered structure [**23**] which is consistent with the XRD analysis. The increase in the intensity of the (Si- O-Si) mode is an indication of the silica structure strengthening with the proceedings of the polycondensation reactions; this is always accompanied by a decrease in the intensity of the Si-OH band (950 cm^{-1}).

6.4.3 FESEM & EDX analysis

The surface morphology for the different supports and the corresponding membranes MR1, MR2 and MR3 are shown in the Figure 6.10. The surface for the membrane MR3 was continuous with a very small amount of superficial defects observed from this figure. For the membrane MR2, the surface shows continuous layer with thin cracks and the membrane MR1 shows rough surface with large cracks compared to MR2 and MR3. However, the α-Al_2O_3 supports for all the membranes were completely covered by the deposited silica layer which is shown in the Figure 6.10. The possible reason for the formation of large cracks in case of MR1 may be due to the large difference of the support pore size and the active silica layer pore size for the membrane.

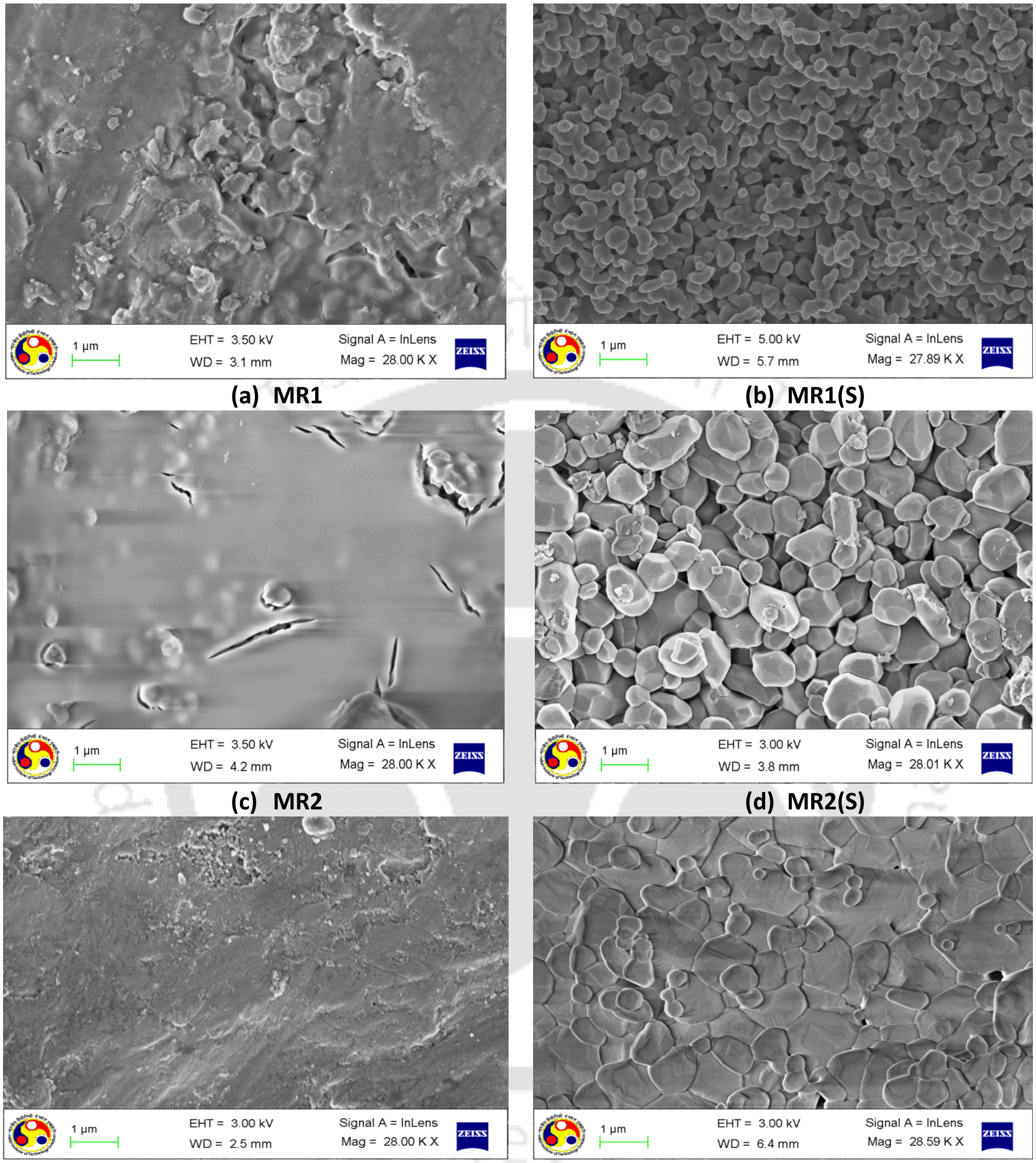

(a) MR1 **(b) MR1(S)**

(c) MR2 **(d) MR2(S)**

(e) MR3 **(f) MR3(S)**

Figure 6.10 FESEM images of the surfaces of the different silica membranes (MR1, MR2, and MR3) synthesized on different α-alumina supports and the corresponding α-alumina supports (MR1(S), MR2(S) and MR3(S)).

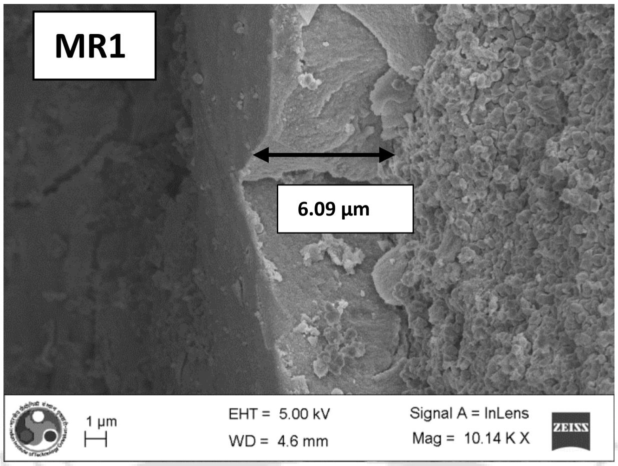

(a) MR1

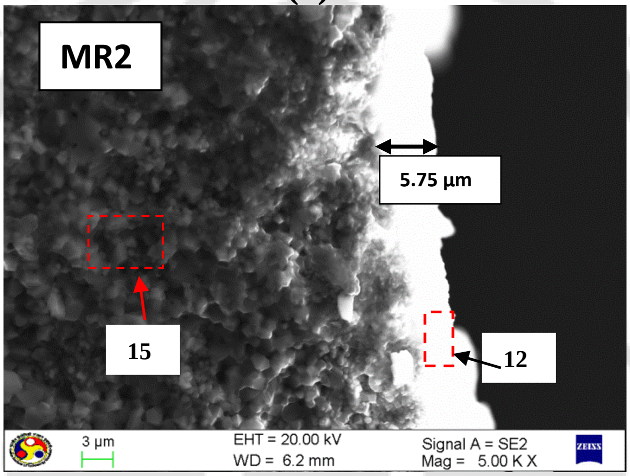

(b) MR2

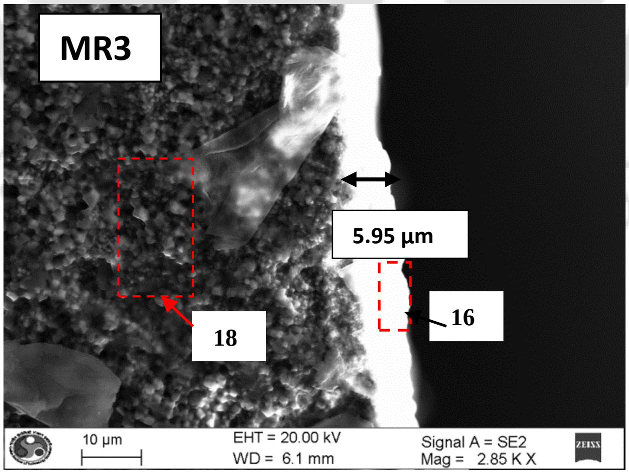

(c) MR3

Figure 6.11 FESEM images for the cross-sectional view of the different silica membranes (MR1, MR2, and MR3) synthesized on different α-alumina supports.

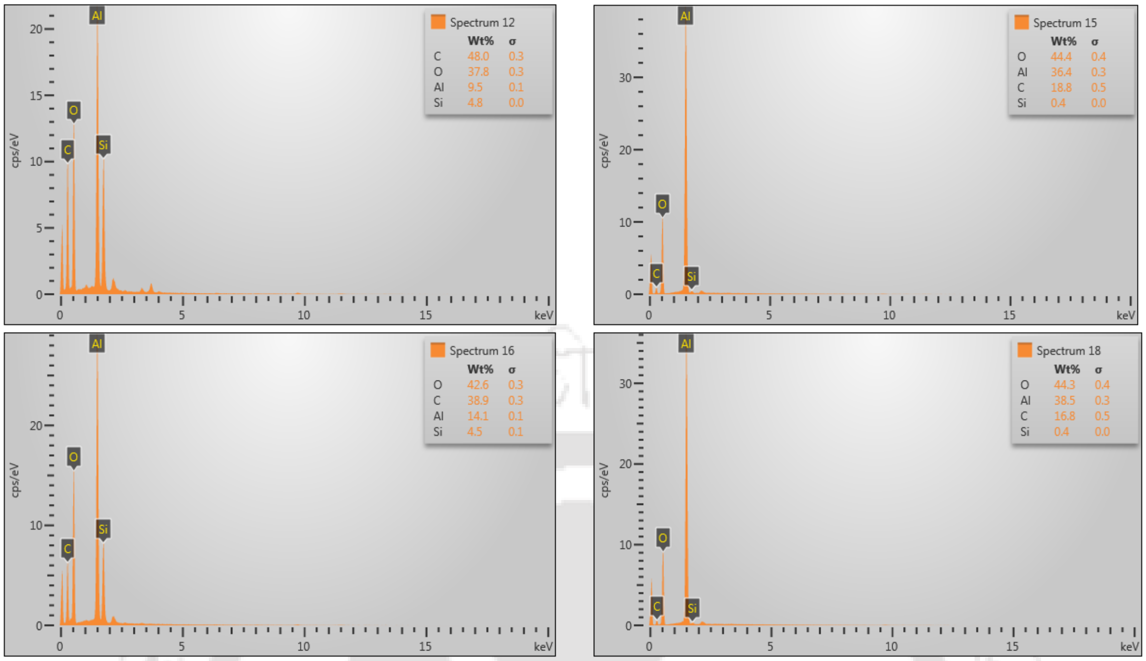

Figure 6.12 EDX analysis of the different silica membranes (MR2 and MR3) synthesized on different α-alumina supports at different locations shown in the Figure 6.11.

As the calcination proceeds, the shrinkage for the silica materials as well as for the films was observed which might not be comparable with the support material (α-alumina). Due to these effects a large mechanical stress occurred between the two layers, which ultimately led to major cracks. Figure 6.11 shows the cross-sectional image of the membranes. The thickness of the membranes varies from ~ 5.7 -6.1 µm range. EDX analysis for the different area located at membrane layer and the support layer for the membranes MR2 and MR3 are shown in Figure 6.12. The presence of Si and C in the membrane layer confirms that the silica layer is formed successfully on the porous α-alumina support. The C element in the membrane layer for EDX analysis confirms the presence of surfactant fragments which is consistent with the FTIR analysis.

6.4.4. Single gas permeation analysis

The steady-state single gas permeation studies were performed using the mesoporous silica membranes to examine the existence of macro porous defects. A permeation test through the mesoporous silica membrane was carried out using N_2 gas before calcination with a pressure drop of 690 kPa (~100 psi) at room temperature.

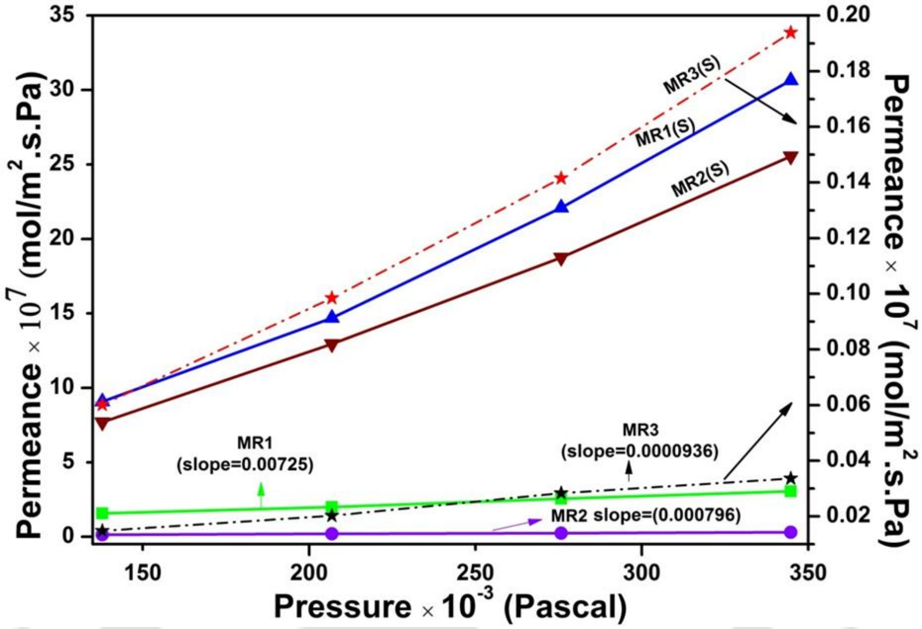

Figure 6.13 N_2 permeance for the different silica membranes (MR1, MR2, and MR3) and corresponding supports (MR1(S), MR2(S), and MR3(S)) at different feed pressures.

No permeation flux through the mesoporous silica membrane was detectable before calcination, which means that the membrane was intact and compact and therefore indicating high quality of membranes. For the membrane MR1, the coating was done more than once, until it became impermeable to N_2 gas at the applied pressure of 690 kPa. Figure 6.13 shows permeance of N_2 gas for the spin coated silica membranes and the supports which are denoted as MR1(S), MR2(S) and MR3(S) for the corresponding membranes. It was observed that the N_2 permeance was reduced ~ (4-6) times after coating, again indicating high quality of membranes.

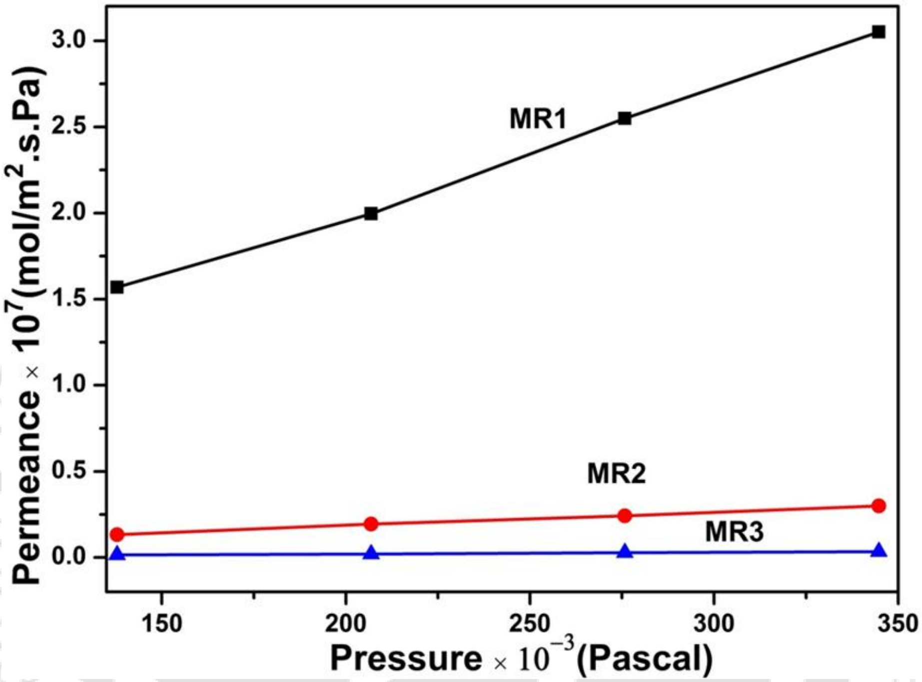

Figure 6.14 N_2 permeance for the different silica membranes (MR1, MR2, and MR3) at different feed pressures.

Figure 6.14 shows the permeances of N_2 gas through the calcined silica membranes. The membrane MR1 exhibits a linear dependence on the differential pressure, indicating the contribution of viscous flow to the total permeation. The silica membrane MR2 showed much weaker dependence of the N_2 permeance on pressure (Figure 6.14) as compared to the silica membrane MR1. The slopes of Figure 6.14 for membranes MR2 and MR3 are 0.000796 and 0.0000936, respectively, which are very less compared to slope for MR1 (0.00725). Very low dependence on pressure drop for the N_2 permeances of the membrane MR2 is due to the presence of thin defects on the membrane surface which are confirmed by the FESEM images (Figure 6.10.(c)).

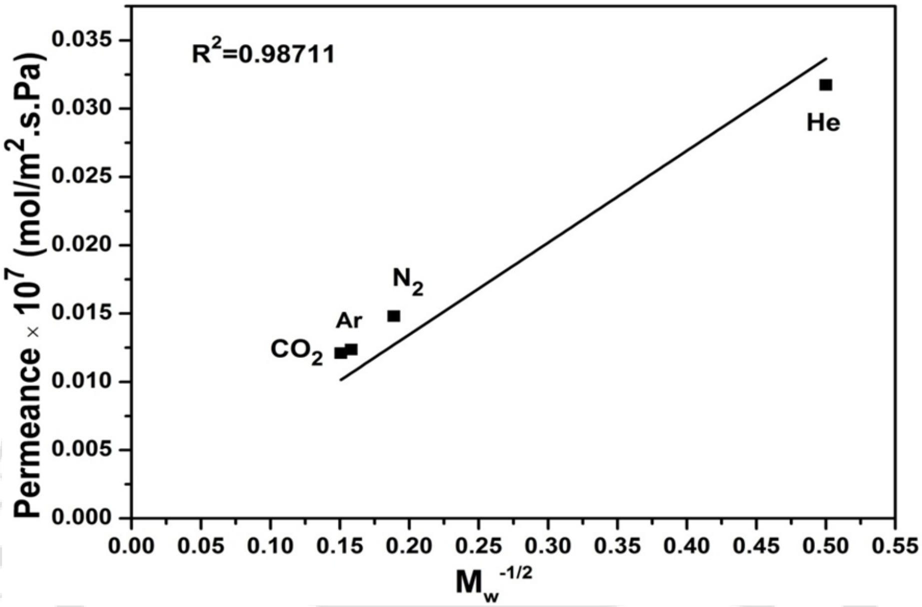

Figure 6.15 Plots of permeance versus $M_W^{-1/2}$ of various gases through mesoporous silica membrane (MR3), measured at 298 K and ~138 kPa.

The gas permeance in the Knudsen regime is inversely proportional to the square root of molecular weight, while for the viscous flow the gas permeance is directly proportional to the pressure. The presence of macro pores inside the α-alumina support in case of MR1 and defects in MR2 membranes could be responsible for the viscous flow contribution to total gas transport. Therefore, the total gas permeance through the MR1 and MR2 membranes involves both the Knudsen and viscous flow contributions. The single gas permeance for pure gases through the silica membrane, MR3, was plotted against the inverse square root of molecular weight at a particular pressure (20 psi). And the linear regression fit is presented in Figure 6.15. The result shows a good linear dependence (R^2

= 0.987) confirming that the gases transport occurred mainly by Knudsen diffusion. The overall gas transport properties through these membranes were governed mainly by the transport properties of the top silica layer.

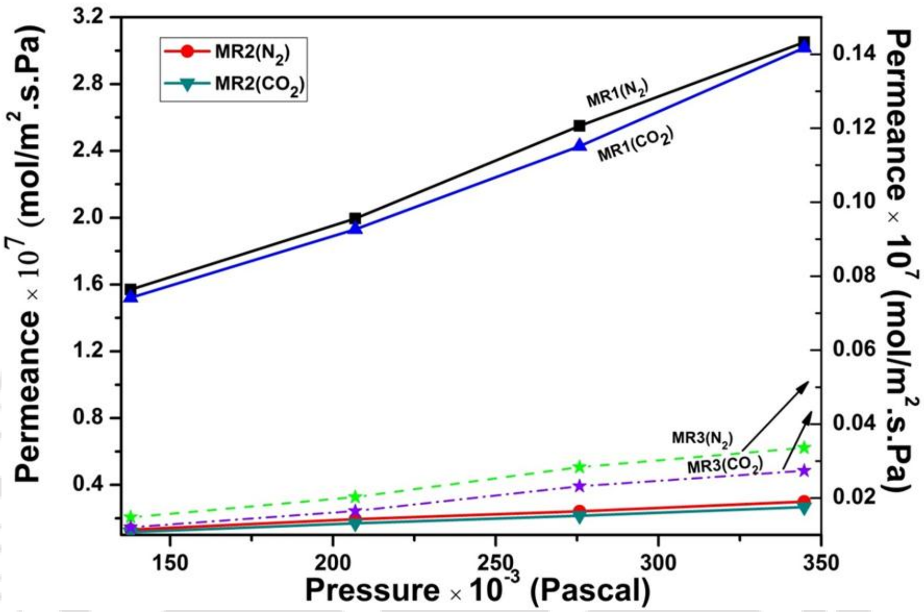

Figure 6.16 N_2 and CO_2 permeance for the different silica membranes (MR1, MR2, and MR3) at different feed pressures.

This was due to the larger gas diffusion resistance imposed by the small pores of the top layer, compared to those of the large pores of the support layers. The steady-state permeation results for the gases N_2 and CO_2 conducted on the different silica membranes prepared on the α-alumina supports for a particular pressure difference are shown in Figure 6.16. The permeance of the individual gases and separation efficiency for the different membranes are tabulated in Table 6.2. The permeance ratios at 298K for the MR1, MR2 and MR3 membranes showed that the ratio for the MR2 and MR3 membranes were closer to the theoretical Knudsen ratio as compared to the MR1 membrane. The permeance ratios for these gases again confirmed the superior quality of the MR2 and MR3 membranes as the permeance ratios for the membranes were close to the Knudsen value. The higher experimental value for the membrane MR1 was likely due to contribution of viscous diffusion for the gases as discussed before.

Table 6.2
CO_2 separation properties of different membrane samples at 298K and ~138 kPa pressure.

Sample	CO_2 Permeance (mol/m^2.s.Pa)×10^7	N_2 Permeance (mol/m^2.s.Pa)×10^7	CO_2/N_2 Permeance ratio	Theoretical Knudsen CO_2/N_2 Permeance ratio
MR3	0.01209	0.0148	0.82	0.8
MR2	0.11683	0.13193	0.88	0.8
MR1	1.52047	1.56927	0.97	0.8

6.4.5 Mixed gas permeation analysis

The effects of feed pressure on CO_2 permeance, N_2 permeance, and CO_2/N_2 selectivity were studied on the amine (3-APS) modified silica membrane, MR2. The pressure effect was studied at 298 K. The sweep side absolute pressure was maintained constant at 28 kPa. The effect of feed pressure on CO_2 and N_2 permeances and CO_2/N_2 selectivity is shown in Figure 6.17. It was observed that with the increase in the pressure, the CO_2 permeance initially decreased and then after about 690 kPa feed absolute pressure, the CO_2 permeance was increased whereas N_2 permeances were decreased continuously with increase in pressure. Initially due to the pore openings, both CO_2 and N_2 passed through the pores. As the pressure was increased, the attachment of CO_2 with the amine groups of the pore walls was increased and as a result the CO_2 permeance was decreased. Up to 690 kPa pressure, the pores might be saturated with the CO_2 molecules. At this stage, due to the additional effect of surface diffusion, the CO_2 permeance was increased. On the other hand due to the adsorption of CO_2 on the pore walls, the pore sizes were reduced and hence, the N_2 permeation might be hindered by the adsorbed CO_2 molecules.

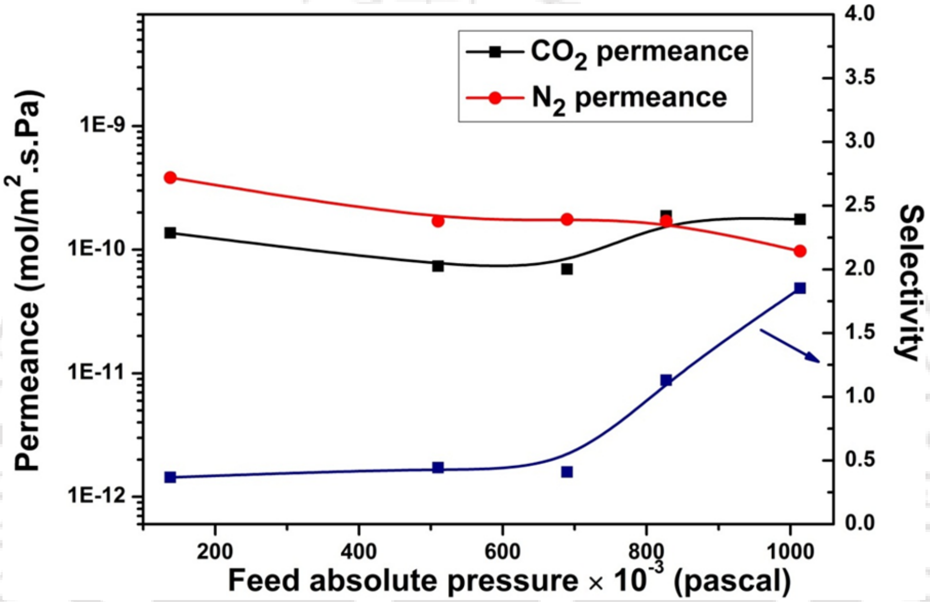

Figure 6.17 CO_2 and N_2 permeance versus feed absolute pressure for CO_2 separation membrane (MR2) at 363 K

And the CO_2/N_2 selectivity was increased after 690 kPa pressure. Thus, the membrane became CO_2 selective from N_2 selective after 690 kPa feed absolute pressure. The CO_2 permeance was observed between 7.35×10^{-11} to 1.76×10^{-10} (mol/m^2 s Pa) whereas, N_2 permeance was observed between 3.82×10^{-10} to 9.74×10^{-11} (mol/m^2 s Pa). Although, the gas permeance of the amine-modified mesoporous silica membrane was decreased as compared to the unmodified membrane, the highest (CO_2/N_2) selectivity value was obtained as 1.85 at ~1085 kPa pressure. The selectivity (CO_2/N_2) obtained in our experiment is less compared to the selectivity measured by Sakamoto et al. [**14**] and Ostwald et al. [**24**]. Possible reason for reduced performance of our membrane may be insufficient functionalization of the membrane and the presence of cracks in the membrane MR2.

6.5. Conclusions

Mesoporous silica membranes were successfully prepared on porous α-alumina supports by spin-coating method of silica sol. Silica membrane (MR1) synthesized on the support having ~0.3 µm pore size showed non-ordered structure, which was confirmed by XRD analysis. On the other hand, the membranes (MR2 & MR3) synthesized on the supports having ~0.13 µm and 0.09 µm pore sizes showed ordered mesoporous domains. The FESEM images showed that the cracks were formed more on large pore sized support compared to small pore sized support (MR3). The FESEM images also confirmed that the α-alumina supports were fully covered by the silica films. FTIR analysis also suggests that the MR3 membrane exhibits the maximum ordered structure as compared to MR1 and MR2. The sharp transmittance bands at 1100 cm^{-1} were observed in all of the spectra are ascribed to the Si-O-Si framework. The peaks are relative to Si-OH (960 cm^{-1}) and to Si-O-Si (1100–1000 cm^{-1}), meaning that the sol–gel matrix were not destroyed. Negligible dependence of N_2 permeance on pressure was observed for the unmodified MR3 & MR2 membranes indicating Knudsen diffusion regime for the N_2 transport as well as high quality membranes. The amine functionalized silica membrane showed promising candidates for CO_2 separation from process streams as they exhibit CO_2 selective at higher pressure.

References

[1] Ogawa, M. A. Simple sol–gel route for the preparation of silica–surfactant mesostructured materials, *Chem. Commun.* **1996,** *10,* 1149-1150.

[2] Ogawa, M.; Masukawa, N. Preparation of transparent thin films of lamellar, hexagonal and cubic silica-surfactant mesostructured materials by rapid solvent evaporation methods, *Micropor. Mesopor. Mater.* **2000,** *38,* 35-41.

[3] Lu, Y.; Ganguli, R.; Drewien, C. A.; Anderson, M. T.; Brinker, C. J.; Gong, W.; Guo, Y.; Soyez, H.; Dunn, B.; Huang, M. H.; Zink, J. I. Continuous formation of supported cubic and hexagonal mesoporous films by sol–gel dip-coating, *Nature.* **1997,** *389,* 364-368.

[4] Sellinger, A.; Weiss, P. R.; Nguyen, A.; Lu, Y.; Assink, R. A.; Gong, W.; Brinker, C. J. Continuous self-assembly of organic–inorganic nanocomposite coatings that mimic nacre, *Nature.* **1998,** *394,* 256-260.

[5] Xomeritakis, G.; Braunbarth, C. M.; Smarsly, B.; Liu, N.; Kohn, R.; Klipowicz, Z.; Brinker, C. J. Aerosol-assisted deposition of surfactant-templated mesoporous silica membranes on porous ceramic supports, *Micropor. Mesopor. Mater.* **2003,** *66,* 91-101.

[6] Zhang, J. L.; Li, W.; Meng, X. K.; Wang, L.; Zhu, L. Synthesis of mesoporous silica membranes oriented by self-assembles of surfactants, *J. Membr. Sci.* **2003,** *222,* 219-224.

[7] Dong, J.; Wegner, K.; Lin, Y. S. Synthesis of submicron polycrystalline MFI zeolite films on porous ceramic supports, *J. Membr. Sci.* **1998,** *148,* 233-241.

[8] Beck, J. S.; Vartuli, J. C.; Roth, W. J.; Leonowicz, M. E.; Kresge, C. T.; Schmitt, K. D.; Chu, C. T. W.; Olson, D. H.; Sheppard, E. W.; McCullen, S. B.; Higgins, J. B.; Schlenker, J. L. A new family of mesoporous molecular sieves prepared with liquid crystal templates, *J. Am. Chem. Soc.* **1992,** *114,* 10834-10843.

[9] Dong, J.; Lin, Y. S.; Hu, M. Z. C.; Peascoe, R. A.; Payzant, E. A. Template-removal-associated microstructural development of porous-ceramic-supported MFI zeolite membranes, *Micropor. Mesopor. Mater.* **2000,** *34,* 241-253.

[10] Kim, S.; Ida, J.; Guliants, V. V.; Lin, J. Y. S. Tailoring Pore Properties of MCM-48 Silica for Selective Adsorption of CO_2, *J. Phys. Chem. B.* **2005,** *109,* 6287-6293.

[11] Liu, C.; Wang, J.; Rong, Z. Mesoporous MCM-48 silica membrane synthesized on a large-pore α-Al_2O_3 ceramic tube, *J. Membr. Sci.* **2007,** *287,* 6-8.

[12] Liu, C.; Wang, L.; Ren, W.; Rong, Z.; Wang, X.; Wang, J. Synthesis and characterization of a mesoporous silica (MCM-48) membrane on a large-pore α-Al_2O_3 ceramic tube, *Micropor. Mesopor. Mater.* **2007,** *106,* 35-39.

[13] Kumar, P.; Ida, J.; Kim, S.; Guliants, V. V.; Lin., J. Y. S. Ordered mesoporous membranes: Effects of support and surfactant removal conditions on membrane quality, *J.Membr. Sci.* **2006,** *279,* 539-547.

[14] Sakamoto, Y.; Nagata, K.; Yogo, K.; Yamada, K. Preparation and CO_2 separation properties of amine-modified mesoporous silica membranes, *Micropor. and Mesopor. Mater.* **2007,** *101,* 303-311.

[15] Besson, S.; Ricolleau, C.; Gacoin, T.; Jacquoid, C.; Boilot, J-.P. A New 3D Organization of Mesopores in Oriented CTAB Silica Films, *J. Phys. Chem. B.* **2000,** *104*, 12095-12097.

[16] Mondal, A. CO_2-Selective Thin-Film Polymer Composite Membranes: Improvement of Thermal Stability and Role of Amine Carriers. PhD Dissertation, *Indian Institute of Technology, Guwahati*, **2014.**

[17] Nishiyama, N.; Tanaka, S.; Egashira, Y.; Oku, Y.; Ueyama, K. Enhancement of structural stability of mesoporous silica thin films prepared by spin coating, *Chem. Mater*. **2002,** *14*, 4229-4234.

[18] Chowdhury, S. R.; Peters, A. M.; Blank, D. H. A.; ten Elshof, J. E. Influence of porous substrate on mesopore structure and water permeability of surfactant templated mesoporous silica membranes, *J. Membr. Sci.* **2006,** *279,* 276-281.

[19] Snyder, R. G.; Strauss, H. L.; Elliger, C. A. Carbon-hydrogen stretching modes and the structure of n-alkyl chains. 1. Long, disordered chains, *J. Phys. Chem.* **1982,** *26*, 5145-5150.

[20] Falcaro, P.; Grosso, D.; Amenitsch, H.; Innocenzi, P. Silica Orthorhombic Mesostructured Films with Low Refractive Index and High Thermal Stability, *J. Phys. Chem.* **2004,** *108*, 10942-10948.

[21] Innocenzi, P. Infrared spectroscopy of sol–gel derived silica-based films: a spectra-microstructure overview, *J. Non-Cryst. Solids.* **2003,** *316*, 309-319.

[22] Almeida, R. M.; Pantano, C. G. Structural investigation of silica gel films by infrared spectroscopy, *J. Appl. Phys.* **1990,** *68*, 4225-4232.

[23] Innocenji, P.; Falcaro, P. Order−Disorder Transitions and Evolution of Silica Structure in Self-Assembled Mesostructured Silica Films Studied through FTIR Spectroscopy, *J. Phys. Chem. B.* **2003,** *107*, 4711-4717.

[24] Ostwal, M.; Pal Singh, R.; Dec, S. F.; Lusk, M. T.; Way, J. D. 3-Aminopropyltriethoxysilane functionalized inorganic membranes for high temperature CO_2/N_2 separation, *J. Membr. Sci.* **2011,** *369*, 139-147.

Chapter 7

CONCLUSIONS AND RECOMMENDATION FOR FUTURE WORK

In this chapter the salient accomplishments and major conclusions of this work are summarized and recommendations on future directions in the subject are made.

7.1 Conclusions

- The surface characteristics of amine-modified ordered mesoporous silica (OMS) materials for CO_2 adsorption and separation were performed and elaborated. The CO_2 isotherms at 30°C are measured up to 10 bar on different amine loaded OMS samples to systematically evaluate the effect of amine on CO_2 adsorption capacity. While at low pressures up to 4 bar, amine loaded sample exhibit more CO_2 uptake, at higher pressures pure OMS material (MCM-48) showed better CO_2 loading.
- Effect of temperature is also examined to understand whether physisorption or chemisorption dominates for amine loaded samples. Modeling of CO_2 isotherms is also carried out to get molecular level insight and to calculate Henry's constants.
- Original OMS (MCM-48) material exhibits a typical type IV shape (characteristic of mesoporous material) for N_2 adsorption isotherm, while that of the amine grafted OMS (MCM-48) material is type I microporous.
- CO_2 adsorption at 0.2 bar and 30 °C is increased significantly from ~0.1 mmol g^{-1} to ~0.84 mmol g^{-1} after grafting of 9 mmol of different on 1 g of OMS (MCM-48) material. CO_2 uptake 0.2 bar obtained for amine grafted OMS (MCM-48) samples is comparable with literature [**1-3**].
- The CO_2 adsorption uptake for amine-modified OMS materials decreases with the increase of temperature. This indicates that the interactions between CO_2 molecules and adsorbent samples are exothermic in nature.

- CO_2 isotherm of pure OMS (MCM-48) material follows Langmuir model indicating homogeneous adsorption nature of OMS (MCM-48) structure. In contrast, CO_2 isotherm on amine grafted samples follow Dual Site Langmuir (DSL) model.
- Henry's constant of OMS (MCM-48) material (0.47 mmol g^{-1} bar^{-1}) is significantly lower than that of samples containing 9 mmol of different amines (29 - 84 mmol g^{-1} bar^{-1}).
- CO_2 adsorption studies show better results for OMS materials obtained by acidic route compared to OMS materials obtained by basic route up to 8 bar pressure.
- α-alumina membrane support quality could be improved by varying the sintering temperature and initial compaction load. Both sintering temperature and initial compaction load played a significant role in α-alumina membrane support properties.
- Experimental studies showed that the prime variable of importance, which affected the key properties like pore size, porosity, flexural strength and shrinkage in diameter of the α-alumina membrane support, was the sintering temperature. However, it was observed that the key properties were marginally influenced by the compaction load. Results obtained from FESEM image analysis as well as N_2 permeation analysis for pore sizes showed quite similar trends.
- Mesoporous silica membranes are successfully prepared on porous α-alumina supports by spin-coating method of silica sol. Silica membrane (MR1) synthesized on the support having ~0.3 µm pore size showed non-ordered structure, which was confirmed by XRD analysis. On the other hand, the

membranes (MR2 & MR3) synthesized on the supports having ~0.13 µm and 0.09 µm pore sizes showed ordered mesoporous domains.

- The FESEM images showed that the cracks were formed more on large pore sized support compared to small pore sized support (MR3). The FESEM images also confirmed that the α-alumina supports were fully covered by the silica films.
- FTIR analysis also suggests that the MR3 membrane exhibits the maximum ordered structure as compared to MR1 and MR2. The sharp transmittance bands at 1100 cm^{-1} are observed in all of the spectra are ascribed to the Si-O-Si framework. The peaks are relative to Si-OH (960 cm^{-1}) and to Si-O-Si (1100–1000 cm^{-1}), meaning that the sol–gel matrix are not destroyed.
- Negligible dependence of N_2 permeance on pressure is observed for the unmodified MR3 & MR2 membranes indicating Knudsen diffusion regime for the N_2 transport as well as high quality membranes.
- The amine functionalized silica membrane shows promising candidates for CO_2 separation from process streams as they exhibit CO_2 selective at higher pressure.

7.2 Recommendations on future directions

Future recommendations on the present work are as follows:

- The CO_2 adsorption study for other amines may be investigated thoroughly for different doses.

- The CO_2 adsorption characteristics for the amine modified OMS materials can be investigated by using gas mixtures containing N_2, SO_x, NO_x, H_2O etc. as these gases are present in the flue gas.
- The acidic route for synthesizing OMS materials can be investigated by using different conditions such as pH, surfactant/silica ratio, etc.
- High quality uniform and porous α-alumina support for membrane can be synthesized by colloidal route [**4**]
- Amine functionalization for OMS membrane can be investigated by using other method such as direct co-condensation route.
- Detailed study for amine functionalized OMS membrane, synthesized by hydrothermal route can be investigated for CO_2separation.
- The total cost analysis for the CO_2 capture of life cycle can be analyzed compare to other CO_2 capture method.

References

[1] Huang, H. Y.; Yang, R. T.; Chinn, D.; Munson, C. L. Amine-grafted MCM-48 and silica xerogel as superior sorbents for acidic gas removal from natural gas. *Ind. Eng. Chem. Res.* **2003,** *42*, 2427-2433.

[2] Kim, S.; Ida, J.; Guliants, V. V.; Lin, J. Y. S. Tailoring pore properties of MCM-48 silica for selective adsorption of CO_2. *J. Phys. Chem. B.* **2005,** *109*, 6287-6293.

[3] Gil, M.; Tiscornia, I.; de la Iglesia, O.; Mallada, R.; Santamaría, J. Monoamine-grafted MCM-48: An efficient material for CO_2 removal at low partial pressures. *Chem. Eng. J.* **2011,** *175*, 291-297.

[4] Mottern, M. L.; Chiu, W. V.; Warchol, Z. T.; Shqau, K.; Verweij, H. High-performance membrane supports: A colloidal approach to the consolidation of coarse particles, *Int. J. Hydrogen. Energy*. **2008,** *33*, 3903-3914.

APPENDIX 1

DETAIL OF THE EXPERIMENTAL PROTOCOL FOLLOWED FOR ADSORPTION MEASUREMENT

A1.1 Experimental Protocol

The necessary steps in the volumetric adsorption measurement unit followed during gas adsorption measurements are presented below.

The complete experimental protocol is divided into sub-sections as following

(i) ***<u>Sample loading</u>***

1) Remove the sample holder from the unit
2) Clean the sample holder with acetone
3) Dry the clean sample holder at ~ 120 ^{o}C for 1 h
4) Cool down it to room temperature
5) Measure the weight of dry sample holder
6) Load with sample (~ 200 g sample)

(ii) ***<u>Activation of sample</u>***

1) Fit the sample holder properly in the adsorption unit.
2) Open the Helium gas cylinder regulator (pressure ~5 bar)
3) Open the valve in the unit for Helium gas
4) Make a degassing profile
    a) Put degassing temperature (120 ^{o}C)
    b) Rate of heating (5 ^{o}C/min)

  - c) Time for degassing (120 min)
5) Start degassing
6) Wait for Cooling (40 ^oC) after degassing and check the leak test.
7) If leak test passed, then, Measure the actual weight of the sample after degassing

(iii) ***Adsorption analysis***

1) Make a file defining the following points
  - a) Adsorption pressure points (say 0.05 to 10 bar, 25 points)
  - b) Adsorption temperature (say 30 ^oC)
  - c) Gas for the adsorption (CO_2)
  - d) Actual sample weight
2) Open the CO_2 regulator and maintain the pressure (~15 bar)
3) Open the valve in the unit for CO_2 gas
4) Start analysis
  - a) Void volume will be measured by machine
  - b) And, then analysis will be started automatically

APPENDIX 2

GAS TRANSPORT PARAMETERS CALCULATION AND GAS CHROMATOGRAPHY DATA

The gas transport parameter calculation and gas chromatography data of calibration gases and G.C operating protocol for this work has also been used by an earlier doctorate student (Dr. Arijit Mondal) of our group [**1**]

A2.1 Gas Transport Parameters (CO_2 and N_2 fluxes, CO_2 and N_2 permeability, CO_2/N_2 selectivity) Calculation

η_R (Mole/min) = retentate molar flux per unit area $= \dfrac{PV}{RT}$ (1)

where

P (atmospheric pressure at which the retentate gas is emitting) = 1 atm.

V (volumetric flow rate of mixed gas at retentate side) = 30 cc/min = 30 × 10^{-06} m^3/min.

T (room temperature at ^oK) = 298.15 ^oK.

R (universal gas constant) = 8.205746 × 10^{-5} m^3 atm / ^oK mol.

$$\eta_R \textbf{ (Mole/min)} = \frac{1\times 30\times 10^{-06}}{8.205746\times 10^{-05}\times 298.15} = \mathbf{1.22 \times 10^{-03}} \textbf{ mole/min.}$$

η_{Ar} (Mole/min) = argon (carrier gas) molar flux per unit area $= \dfrac{PV}{RT}$ (2)

where

P (atmospheric pressure at which the carrier gas is emitting) = 1 atm.

V (volumetric flow rate of carrier gas at permeate side) = 27 cc/min = 27 × 10^{-06} m^3/min.

T (room temperature at ^{o}K) = 298.15 ^{o}K.

R (universal gas constant) = 8.205746 × 10^{-5} m^3 atm / ^{o}K mol.

$$\eta_{Ar}\ \textbf{(Mole/min)} = \frac{1\times 27\times 10^{-06}}{8.205746\times 10^{-05}\times 298.15} = \mathbf{1.08 \times 10^{-03}\ mole/min.}$$

η_P (Mole/min) = permeate molar flux per unit area =

$$[(CO_2\ mole\ fraction\times\frac{CO_2(P)_{G.C}}{CO_2(F)_{G.C}})+(N_2\ mole\ fraction\times\frac{N_2(P)_{G.C}}{N_2(F)_{G.C}})]$$
$$\times\frac{Ar\ molar\ flux(mol/\min)}{[1-(CO_2\ mole\ fraction\times\frac{CO_2(P)_{G.C}}{CO_2(F)_{G.C}})-(N_2\ mole\ fraction\times\frac{N_2(P)_{G.C}}{N_2(F)_{G.C}})]} \qquad (3)$$

where

$CO_2(P)_{G.C}$ = CO_2 concentration at permeate side from G.C analysis

$CO_2(F)_{G.C}$ = CO_2 concentration at feed side from G.C analysis

$N_2(P)_{G.C}$ = N_2 concentration at permeate side from G.C analysis

$N_2(F)_{G.C}$ = N_2 concentration at feed side from G.C analysis

CO_2 mole fraction = 0.2 (say)

N_2 mole fraction = 0.8 (say)

Ar molar flux = 1.08 × 10^{-03} mole/min

$p_{CO_2}(R, psi)$ = CO_2 partial pressure at retentate side =

$$[BP_F + P_{ambient}\times\frac{14.7}{101.325}]\times$$
$$\frac{[\eta_R - 0.5\times\eta_P]\times CO_2\,mole\ fraction\times[0.5+0.5\times\frac{CO_2(R)_{G.C}}{CO_2(F)_{G.C}}]}{[\eta_R - 0.5\times\eta_P]+\frac{[0.5\times H_2O_F]+[0.5\times H_2O_{distribution}\times(H_2O_F+H_2O_S)]}{18}} \qquad (4)$$

where

BP_F = Back pressure (psig) at feed side of the membrane module = 25 psig (say)

$P_{ambient}$ = Ambient pressure (kPa) = 101.6 kPa

$CO_2(R)_{G.C}$ = CO_2 concentration at retentate side from G.C analysis

$CO_2(F)_{G.C}$ = CO_2 concentration at feed side from G.C analysis

H_2O_F = Feed side water flow rate (ml/min)

H_2O_S = Sweep side water flow rate (ml/min)

$H_2O_{distribution}$ = Total water distribution (ml/min)
$\eta_R = Retentate\ molarflux\ per\ unit\ area\ (mol/min)$

$\eta_P = Permeate\ molarflux\ per\ unit\ area\ (mol/min)$

CO_2 mole fraction = 0.2

$p_{CO_2}(R, psi)$ **= CO_2 partial pressure at retentate side (psi)**

$p_{CO_2}(P, psi)$ = CO_2 partial pressure at permeate side =

$$[BP_S + P_{ambient} \times \frac{14.7}{101.325}] \times \frac{[(\eta_{Ar} + 0.5 \times \eta_P) \times CO_2\, mole\ fraction \times 0.5 \times \frac{CO_2(P)_{G.C}}{CO_2(F)_{G.C}}]}{[\eta_{Ar} + 0.5 \times \eta_P] + \frac{[0.5 \times H_2O_S] + [0.5 \times (1 - H_2O\, distribution) \times (H_2O_F + H_2O_S)]}{18}} \quad (5)$$

where

BP_S = Back pressure (psig) at sweep side of the membrane module = 3.5 psig (say)

$P_{ambient}$ = Ambient pressure (kPa) = 101.6 kPa

$CO_2(P)_{G.C}$ = CO_2 concentration at permeate side from G.C analysis

$CO_2(F)_{G.C}$ = CO_2 concentration at feed side from G.C analysis

H_2O_F = Feed side water flow rate (ml/min)

H_2O_S = Sweep side water flow rate (ml/min)

$H_2O_{distribution}$ = Total water distribution (ml/min) = 0.22 ml/min

$\eta_{Ar} = Argon\ molarflux\ per\ unit\ area\ (mol/min)$

$\eta_P = Permeate\ molarflux\ per\ unit\ area\ (mol/min)$

CO_2 mole fraction = 0.2

$p_{CO_2}(P, psi)$ = **CO_2 partial pressure at permeate side (psi)**

$p_{N_2}(R, psi)$ = N_2 partial pressure at retentate side =

$$[BP_F + P_{ambient} \times \frac{14.7}{101.325}] \times \frac{[\eta_R - 0.5 \times \eta_P] \times N_2\ mole\ fraction \times [0.5 + 0.5 \times \frac{N_2(R)_{G.C}}{N_2(F)_{G.C}}]}{[\eta_R - 0.5 \times \eta_P] + \frac{[0.5 \times H_2O_F] + [0.5 \times H_2O\ distribution \times (H_2O_F + H_2O_S)]}{18}} \qquad (6)$$

where

BP_F = Back pressure (psig) at feed side of the membrane module = 25 psig (say)

$P_{ambient}$ = Ambient pressure (kPa) = 101.6 kPa

$N_2(R)_{G.C}$ = N_2 concentration at retentate side from G.C analysis

$N_2(F)_{G.C}$ = N_2 concentration at feed side from G.C analysis

H_2O_F = Feed side water flow rate (ml/min)

H_2O_S = Sweep side water flow rate (ml/min)

$H_2O_{distribution}$ = Total water distribution (ml/min)

$\eta_R = Retentate\ molarflux\ per\ unit\ area\ (mol/min)$

$\eta_P = Permeate\ molarflux\ per\ unit\ area\ (mol/min)$

N_2 mole fraction = 0.8

$p_{N_2}(R, psi)$ = **N_2 partial pressure at retentate side (psi)**

$p_{N_2}(P, psi)$ = N_2 partial pressure at permeate side =

$$[BP_S + P_{ambient} \times \frac{14.7}{101.325}] \times \frac{[(\eta_{Ar} + 0.5 \times \eta_P) \times N_2\ mole\ fraction \times 0.5 \times \frac{N_2(P)_{G.C}}{N_2(F)_{G.C}}]}{[\eta_{Ar} + 0.5 \times \eta_P] + \frac{[0.5 \times H_2O_S] + [0.5 \times (1 - H_2O\, distribution) \times (H_2O_F + H_2O_S)]}{18}} \qquad (7)$$

where

BP_S = Back pressure (psig) at sweep side of the membrane module = 3.5 psig (say)

$P_{ambient}$ = Ambient pressure (kPa) = 101.6 kPa

$N_2(P)_{G.C}$ = N_2 concentration at permeate side from G.C analysis

$N_2(F)_{G.C}$ = N_2 concentration at feed side from G.C analysis

H_2O_F = Feed side water flow rate (ml/min)

H_2O_S = Sweep side water flow rate (ml/min)

$H_2O_{distribution}$ = Total water distribution (ml/min)

$\eta_{Ar} = Argon\ molarflux\ per\ unit\ area\ (mol/min)$

$\eta_P = Permeate\ molarflux\ per\ unit\ area\ (mol/min)$

N_2 mole fraction = 0.8

$p_{N_2}(P, psi)$ **= N_2 partial pressure at permeate side (psi)**

V_{CO2} (cm^3/sec) = permeate volumetric gas flow rate of CO_2 =

$$\frac{\eta_{Ar} \times CO_2(P)_{G.C} \times CO_2\ mole\ fraction \times 8.314 \times 273.15 \times 1000000}{CO_2(F)_{G.C} \times 101325 \times 60 \times [1 - (CO_2\ mol\ fraction \times \frac{CO_2(P)_{G.C}}{CO_2(F)_{G.C}}) - (N_2\ mol\ fraction \times \frac{N_2(P)_{G.C}}{N_2(F)_{G.C}})]} \qquad (8)$$

V_{CO2} (cm^3/sec) = permeate volumetric gas flow rate of (cm^3/sec)

V_{N2} (cm^3/sec) = permeate volumetric gas flow rate of N_2 =

$$\frac{\eta_{Ar} \times N_2(P)_{G.C} \times N_2 \ mole\ fraction \times 8.314 \times 273.15 \times 1000000}{N_2(F)_{G.C} \times 101325 \times 60 \times [1-(CO_2\ mol\ fraction \times \frac{CO_2(P)_{G.C}}{CO_2(F)_{G.C}}) - (N_2\ mol\ fraction \times \frac{N_2(P)_{G.C}}{N_2(F)_{G.C}})]} \quad (9)$$

V_{N2} (cm^3/sec) = permeate volumetric gas flow rate of N_2 (cm^3/sec)

CO_2 Flux (10^{-6}cm^3(STP)/cm^{2}sec), CO_2 Permeability (Barrer), CO_2 Permeance (GPU) and CO_2/N_2 Selectivity

$$(\Delta p)_{CO_2} \ at \ psi = \text{partial pressure difference at psi} = p_{CO_2}(R, psi) - p_{CO_2}(P, psi)$$

$$(\Delta p)_{CO_2} \ at \ psi = 3.19 \ psi$$

$$(\Delta p)_{CO_2} \ at \ cmHg = \text{partial pressure difference at cmHg} = \frac{(\Delta p)_{CO_2} \ at \ psi}{14.7} \times 76$$

$$(\Delta p)_{CO_2} \ at \ cmHg = 16.49 \ cmHg$$

$$CO_2\text{flux} = \frac{V_{CO_2}(cm^3/\sec)}{area\, of\ membrane\left(cm^2\right)}$$

where,

V_{CO2} (cm^3/sec) = permeate volumetric gas flow rate of (cm^3/sec)

Area of membrane = 10.17 cm^2

CO_2 flux = in cm^3 (STP) / cm^{2}s

$$CO_2 \ \text{permeability} = \frac{V_{CO_2}(cm^3/\sec) \times thickness\left(cm\right)}{area\, of\ membrane\left(cm^2\right) \times (\Delta p)_{CO_2}\ at\, cmHg}$$

where,

V_{CO2} (cm^3/sec) = permeate volumetric gas flow rate of (cm^3/sec)

Area of membrane = 10.17 cm^2

Thickness = 0.0045 cm = 45 micron (say)

$(\Delta p)_{CO_2}\ at\ cmHg = 16.49\ cmHg$

CO_2 permeability = 'Y' × 10^{-10} cm^3 (STP) cm / cm^2 s cmHg = 'Y' Barrer

$$CO_2 permeance = \frac{CO_2 permeability}{thickness} = \frac{'Y'\ Barrer}{45} =' Z' GPU$$

1 GPU = 10^{-6} cm^3 (STP) / cm^2 s cmHg

$$\frac{CO_2}{N_2} Selectivity = \frac{\frac{CO_2(P)_{G.C.}}{N_2(P)_{G.C.}}}{\frac{CO_2(R)_{G.C.}}{N_2(R)_{G.C.}}}$$

N_2 Flux (10^{-6}cm^3(STP)/cm^{2}sec), N_2 Permeability (Barrer), N_2 Permeance (GPU) and CO_2/N_2 Selectivity

$(\Delta p)_{N_2}\ at\ psi$ = partial pressure difference at psi = $p_{N_2}(R, psi) - p_{N_2}(P, psi)$

$(\Delta p)_{N_2}\ at\ psi = 15.84\ psi$

$(\Delta p)_{N_2}\ at\ cmHg$ = partial pressure difference at cmHg = $\dfrac{(\Delta p)_{N_2}\ at\ psi}{14.7} \times 76$

$(\Delta p)_{N_2}\ at\ cmHg = 81.89\ cmHg$

$$N_2\text{flux} = \frac{V_{N_2}(cm^3/\sec)}{area\, of\ membrane\left(cm^2\right)}$$

where,

V_{N2} (cm^3/sec) = permeate volumetric gas flow rate of N_2 (cm^3/sec)

Area of membrane = 10.17 cm^2

N_2 flux = 'H' × 10^{-6} cm^3 (STP) / cm^2s

$$N_2 \text{ permeability} = \frac{V_{N_2}(cm^3/\sec) \times thickness\left(cm\right)}{area\,of\ membrane\left(cm^2\right) \times (\Delta p)_{N_2}\ at\,cmHg}$$

where,

V_{N2} (cm^3/sec) = permeate volumetric gas flow rate of N_2 (cm^3/sec)

Area of membrane = 10.17 cm^2

Thickness = 0.0045 cm = 45 micron (say)

$(\Delta p)_{N_2}\ at\ cmHg = 81.89\ cmHg$

N_2 permeability = in cm^3 (STP) cm / cm^2 s cmHg = Barrer

$$\mathbf{N_2\ permeance} = \frac{N_2 permeability}{thickness}\ \text{(GPU)}$$

1 GPU = 10^{-6} cm^3 (STP) / cm^2 s cmHg

Reference

[1] Mondal, A. CO_2-Selective Thin-Film Polymer Composite Membranes: Improvement of Thermal Stability and Role of Amine Carriers. PhD Dissertation, *Indian Institute of Technology, Guwahati,* **2014.**

A2.2 Gas Chromatography Data of Calibration Gases and G.C Operating Protocol

A2.2.1 Calibration Gases for G.C

Five known concentration of CO_2 and N_2 gas mixture were used as calibration gas. This was (4% CO_2 + 4% N_2, balance Argon), (8% CO_2 + 8% N_2, balance Argon), (12% CO_2 + 12% N_2, balance Argon), (20% CO_2, balance N_2) and (40% CO_2, balance N_2).

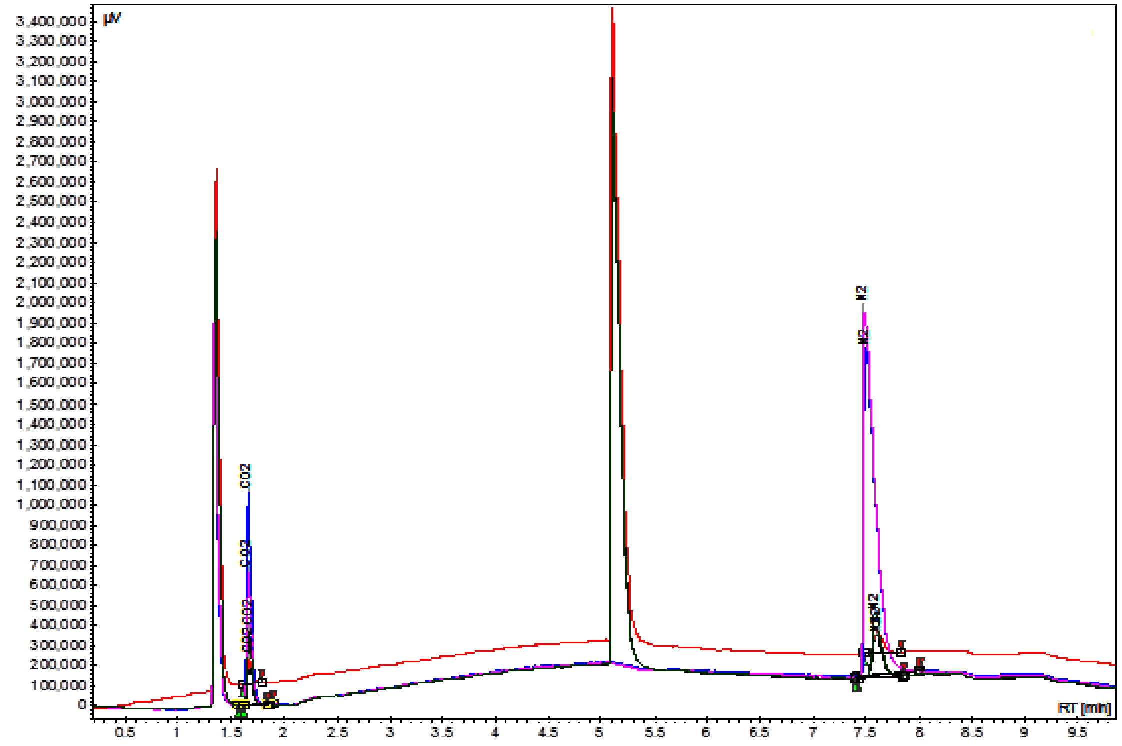

Figure A2.1 Peak intensity and position of all five CO_2 and N_2 calibration gases

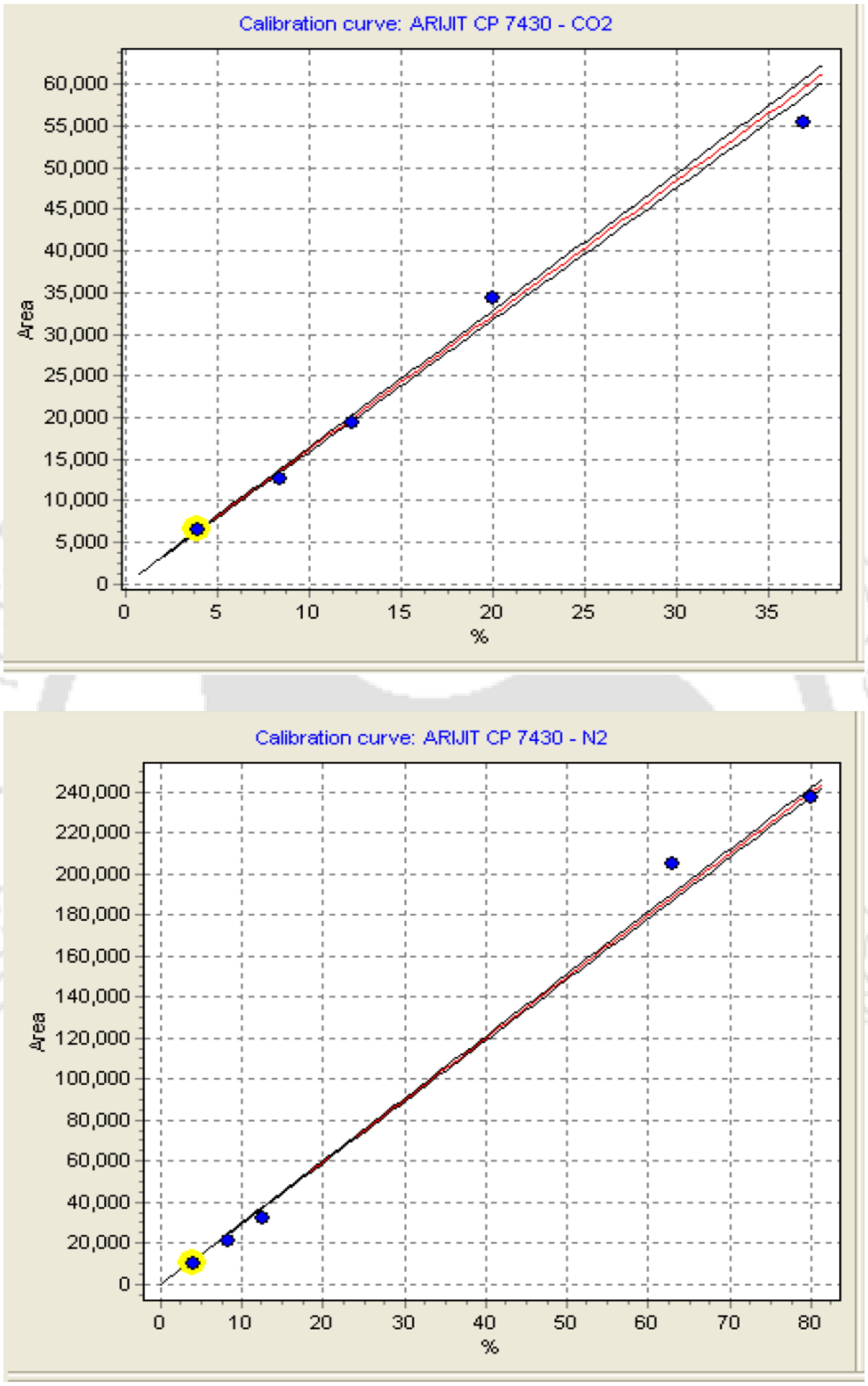

Figure A2.2 Plot of all five CO_2 and N_2 calibration gases

A2.2.2 G.C operating protocol

Here, we have used Varian-450 G.C for all the permeation experiments. The detail G.C operating protocols are mentioned below:

Injector programing: Heater (ON) at 120^{o}C

Tine (min)	**Split state**	**Split ratio**
Initial	ON	1
0.00	ON	1
1.00	ON	1

Oven programing:

Column oven (ON) and Rear oven (ON) at 100^{o}C

Rate (^{o}C/min)	**Temperature (^{o}C)**	**Time (min)**	**Total time (min)**
initial	40	2.00	2.00
10	70	5.00	10.00

Total time 10.00

Column pneumatics: (pressure program)

Rate (psi/min)	**Pressure (psi)**	**Time (min)**	**Total time (min)**
Initial	15	10.00	10.00

Total time 10.00

Detector (TCD) programing:

Heater (ON) at 95°C

Electronics (ON)

Filament temperature at 235°C

Filament temperature limit at 390°C

TCD event table

Time (min)	**Range**	**Auto zero**	**Polarity**
Initial	0.05	YES	Negative

Gas sampling valve (GSV) programing:

Time (min)	**Gas sampling valve**
Initial	Fill
0.02	Inject

A2.2.3 Detail Purity of all Calibration gases

Table A2.1 Detail purity percentage of all calibration gases

Name	Purity compositions
4% CO_2 + 4% N_2, balance Argon	CO_2 (99.999%), N_2 (99.999%), Ar (99.999%), H_2O (< 2 ppm) and CO (< 0.5 ppm)
8% CO_2 + 8% N_2, balance Argon	CO_2 (99.999%), N_2 (99.999%), Ar (99.999%), H_2O (< 2 ppm) and CO (< 0.5 ppm)
12% CO_2 + 12% N_2, balance Argon	CO_2 (99.999%), N_2 (99.999%), Ar (99.999%), H_2O (< 2 ppm) and CO (< 0.5 ppm)
20% CO_2, balance N_2	CO_2 (99.999%), N_2 (99.999%), H_2O (< 2 ppm) and CO (< 0.5 ppm)
40% CO_2, balance N_2	CO_2 (99.999%), N_2 (99.999%), H_2O (< 2 ppm) and CO (< 0.5 ppm)